REACTIVE FORCE FIELD BASED ATOMISTIC SIMULATIONS OF SILICON ANODE UPON LITHIATION AND DELITHIATION IN LITHIUM-ION BATTERIES

By

Kwang Jin Kim

A DISSERTATION

Submitted to
Michigan State University
in partial fulfillment of the requirements
for the degree of

Materials Science and Engineering – Doctor of Philosophy

2018

ABSTRACT

REACTIVE FORCE FIELD BASED ATOMISTIC SIMULATIONS OF SILICON ANODE UPON LITHIATION AND DELITHIATION IN LITHIUM-ION BATTERIES

By

Kwang Jin Kim

Silicon (Si) has been considered as a promising anode material for lithium-ion batteries due to its high theoretical capacity (3750 mAh/g), low discharge voltage, abundancy, and low cost. However, electrochemical lithiation and delithiation of Si proceeds via solid-state amorphization and massive volume expansion/contraction, resulting in destructive consequences such as slow rate performance, irreversible capacity loss, and mechanical degradation. These problems significantly affect the capacity retention and cycle life and limits the wide application of Si anode. In this thesis, molecular dynamic (MD) simulations with reactive force field (ReaxFF) were performed to better understand and design optimized Si anodes with enhanced rate performance and minimized irreversible capacity loss. Furthermore, the transferability of ReaxFF to simulate SiO system was evaluate and the ground work was laid to design extensive training set of Li-Si system for machine-learning potentials development. There are two major discoveries based on the simulation work.

First, to elucidate the rate-limiting factor upon lithiation of Si for improved rate performance, reactive MD simulations were performed in crystalline-Si and amorphous-Si at the atomic-scale. It was discovered that Si movement is the rate-limiting factor. It was also revealed that Li diffusivity increases with Li concentrations, opposite to many currently used intercalation compounds. Furthermore, the new finding highlighted that vacancies in Si can accelerate the lithiation process dramatically.

Then, the irreversible atomic-scale structural changes upon delithiation was studied using a newly-developed reactive MD-based delithiation algorithm with well-controlled chemical potential gradient driving force and delithiation rate. During fast delithiation, a cage-like structure with high Si content was formed near the surface, thus trapping significant amount of Li atoms inside the Si-thin-film. Furthermore, delithiated amorphous Li_xSi (with no porosity and trapped Li) still has higher volume (lower density) than the equilibrium structures at the same Li concentration throughout the whole delithiation process regardless of the delithiation rates. The origin of the excess volume is the loss of directly bonded Si-Si pairs, which makes the subsequent re-lithiation proceed faster. These new insights lead to several recommendations, such as the delithiation rate and depth of charge, to avoid trapped Li and coating delamination in order to enhance the life of Si electrodes.

ACKNOWLEDGEMENTS

First of all, I would like to thank my advisor Prof. Yue Qi for her great inspirations and motivations. She has provided constructive guidance, which trained me to become an independent researcher. Without her constant encouragements, I would not be able to complete my research journey. Het integrity, enthusiasm, and companionship set an excellent example for me to follow, which will enlighten and guide my life. I also want to appreciate my committee member, Prof. Wei Lai, Prof. Lawrence Dzral, and Prof. Rebecca Anthony for their helpful directions and suggestions on my researches. Additionally, special thanks to our collaborator, Prof. H.Metin Aktulga and Prof. Matthew Hirn, for their helpful discussion and contributions.

I also want to acknowledge all my colleagues and friends in Michigan State University: Christine James, Tridip Das, Yuxiao Lin, Jialin Liu, Hong-Kang Tian, Thanaphong Phongpreecha, Yunsong Li, Kurt A. O'Hearn, Paul Sinz, and Xavier Brumwell. They shared their expertise with me and support my research. It has been a pleasure to know you and share my life in graduate school.

Most importantly, I want to appreciate my family for their unconditional love and encouragements. Their trust and love made me a strong and confident person, which allowed me to complete this work.

TABLE OF CONTENTS

LIST OF TABLES	vii
LIST OF FIGURES	viii
Chapter 1 Background and Motivations	1
1.1 Li-ion Batteries and Silicon Negative Electrode	
1.1.1 Thermodynamics and Kinetics of Electrochemical Reaction of Li with Si	
1.1.2 Computational Studies of Li-Si System	
1.1.2. (a) Density Functional Theory Calculation of Li-Si	
1.1.2. (b) Molecular Dynamics Simulation of Li-Si	
1.2 Motivation and Thesis Outline	
Chapter 2 Overview of Computational Methods	20
2.1 Energy Calculation using DFT and Force Fields	
2.1.1 Density Functional Theory	
2.1.2 Force Fields	
2.1.2. (a) Introduction	
2.1.2. (b) Classical Force Field	23
2.1.2. (c) Reactive Force Field	25
2.2 Molecular Dynamics	26
2.2.1 Ab Initio MD and Force Field based MD	
2.2.2 Equation of Motions and Thermodynamic Ensembles	28
Chapter 3 Vacancies in Si Can Improve the Concentration-Dependent Lithiation Rate	30
3.1 Summary	30
3.2 Introduction	31
3.3 Simulation Methods	33
3.3.1 Reactive Force Field for Li-Si System	33
3.3.2 Molecular Dynamics Simulations	34
3.3.3 Local Concentration and Diffusion Properties Analysis	36
3.4 Results and Discussion	38
3.4.1 How Lithiation Proceeds in a-Si	39
3.4.2 How Lithiation Proceeds in c-Si	39
3.4.3 Si Vacancy Generation Accelerates Lithiation Dynamics	41
3.4.4 Random Diffusion of Li in Si is Concentration Dependent	46
3.4.4. (a) Local Concentration Evolution	46
3.4.4. (b) Random Diffusion of Li in Si is Concentration-Dependent	49
3.4.4. (c) Room-Temperature Li and Si Diffusivity Calculation	51
3.5 Conclusions	52
Chapter 4 Atomistic Simulation Derived Insight on the Irreversible Structural Changes of Si	
Electrode during Fast and Slow Delithiation	54
4.1 Summary	

4.2 Introduction	55
4.3 Simulation Methods	58
4.3.1 Reactive Force Field for Li-Si-Al-O-H System	58
4.3.2 Molecular Dynamics Simulations of the Delithiation Process	60
4.3.3 Analysis of Volume Contraction, Pore Evolution, and Li Trap	oping63
4.3.4 Comparison between a-Li _x Si at Equilibrium and Relithiated a	n-Li _x Si 65
4.4 Results and Discussion	66
4.4.1 Delithiation Proceeds with Different Rates	66
4.4.2 Porous Structures Evolution and Coating Delamination	68
4.4.3 Quantifying the Volume Contribution	
4.4.4 Dilated a-Li _x Si Exhibits Faster Lithiation Rate in the Second	Cycle73
4.4.5 Si Cage as the Origin of Li Trapping-Induced Irreversible Ca	pacity Loss75
4.5 Conclusions	77
Chapter 5 Reactive Force Field Evaluation for Lithiation/Delithiation in Si-	
5.1 Introduction	
5.2 Simulation Methods	
5.2.1 First-principles DFT Calculations	
5.2.2 ReaxFF-based Molecular Dynamics Calculations	
5.3 Results and Discussions	
5.3.1 Direct Energy Comparison of ReaxFF versus DFT	
5.3.2 Non-Physical SiO Structure Predicted by ReaxFF-MD	
5.3.3 Reason for the Errors in the MD Results	
5.3.4 Design of the Training Set for Li-Si-O System	
5.4 Conclusions	91
	0.2
Chapter 6 Generation of Li-Si Training Set for Machine-Learning Potential	
6.1 Introduction	
6.2 Automated Construction of the Training Set with Crystalline and	
6.2.1 c-Li _x Si structures	
6.2.2 a-Li _x Si Structures	
6.2.3 Formation Energy and OCV for the Training Set	
6.3 Elastic Property Calculation to Validate Machine Learning Resul	
6.4 Conclusions	104
Chapter 7 Conclusions	106
APPENDIX	109
REFERENCES	137
K P.P.P.K P.N.J. P.A	13/

LIST OF TABLES

Table 3-1 Summary of time required to reach fully lithiated stage, together with simulation information of amorphous Si and crystalline Si with (100), (110), and (111) surface orientations 35
Table 5-1 Summary of density, microstructure, and simulation size of a-Si, a-SiO, and a-SiO ₂ 84
Table 5-2 Summary of energy calculation of a-Si, a-SiO, and a-SiO ₂ from optimized structures generated by first-principle DFT calculations and ReaxFF-MD simulations
Table 6-1 Structural parameters for c-Li, c-Si, and c-Li _x Si alloys at equilibrium

LIST OF FIGURES

Figure 1-1 Energy density comparison of different batteries systems (Adapted from reference [¹]. Copyright © Nature 2001)
Figure 1-2 Schematic diagram of Li-ion batteries, which is composed of cathode (LiCoO ₂), anode (graphite), electrolyte, and separator (Adapted from reference [³]. Copyright © Journal of Power Sources 2013)
Figure 1-3 (a) Gravimetric capacity of different anode materials (Adapted from reference [⁶]. Copyright © Chemical Reviews 2014) (b) Degradation mechanism of Si anodes upon lithiation-driven volume expansion (Adapted from reference [⁷]. Copyright © Nature Reviews Materials 2016)
Figure 1-4 (a) - (c) Various morphologies of Si active materials and their composites (Adapted from reference [^{7,12}]. Copyright © Nature Reviews Materials 2016) (d) Schematic of SiO _x composite anode in atomic-level (Adapted from reference [¹³]. Copyright © The Journal of Physical Chemistry C 2016) (e) Schematic describing the formation of the artificial SEI on Li _x Si nanosphere (Adapted from reference [¹⁴]. Copyright © Journal of the American Chemical Society 2015) (f) Illustration of Si binder concepts (Adapted from reference [⁷]. Copyright © Nature Reviews Materials 2016)
Figure 1-5 (a) Li-Si phase diagram (Adapted from reference [40]. Copyright © Bulletin of Alloy Phase Diagram 1990) (b) Experimentally measured voltage vs. composition of Li-Si system 6
Figure 1-6 (a) Schematic diagram of phase evolution upon multiple cycle based on in situ XRD of charge/discharge cycles of Li-Si battery (Adapted from reference [33]. Copyright © Journal of the Electrochemical Society 2007) (b) High-resolution TEM image of the sharp phase boundary between c-Si and a-Li _x Si (Adapted from reference [37]. Copyright © Physical Review Letters 2011)
Figure 1-7 (a) Characteristic volume expansion of c-Si nanopillars along <100>, <110>, and <111> axial orientations upon lithiation (Adapted from reference [⁴⁵]. Copyright © Nano Letters 2011) (b) High-resolution TEM image and schematic diagram describing the lateral ledge flow along {111} plane (Adapted from reference [⁴³]. Copyright © Nature Nanotechnology 2012) 9
Figure 1-8 Multi-scale modeling and simulation
Figure 1-9 (a) Experimentally measured (red curve) and computationally calculated (blue, green, and black curve) voltage vs. composition of Li _x Si. (Adapted from reference [⁵²]. Copyright © Journal of the Electrochemical Society 2009) (b) Net charge of Li and Si in c-Li _x Si (LiSi, Li ₁₂ Si ₇ , Li ₇ Si ₃ , Li ₁₃ Si ₄ , Li ₁₅ Si ₄ , and Li ₂₁ Si ₅). (Adapted from reference [⁵⁴]. Copyright © Journal of Alloys and Compounds 2010)

Figure 1-10 (a) Representative structural snapshots at various lithiation stages of c-Si (top) and a-Si (a-Si) at 1200K. Cyan and purple color spheres in the figure represent Si and Li atoms, respectively (b) Representation of structures form during lithiation (c) Structural statistics with time upon for lithiation of c-Si. (Adapted from reference [⁵⁶]. Copyright © Nano Letters 2011) 15
Figure 1-11 (a) Structural snapshot representing the lithiation of a-Si and c-Si with (100), (110), and (111) surface orientations after 200 ps at 1200K using ReaxFF-MD simulations (Adapted from reference [⁶²]. Copyright © The Journal of Physical Chemistry C 2014) (b) Structural snapshot representing the delithiation of lithiated Si NW with MD equilibration time of 250 ps (red) and 500 ps (black) for each delithiation steps (Adapted from reference [⁶³]. Copyright © The Journal of Physical Chemistry C 2015)
Figure 2-1 Description of energy terms for classical force fields. Each number represents (1) Bond, (2) Angle, (3) Dihedral, (4) van der Waals, and (5) Electrostatic contribution
Figure 2-2 (a) Overview of the ReaxFF total energy components ⁶¹ (b) Interatomic distance dependency of the carbon-carbon bond order ⁷²
Figure 2-3 Illustration of molecular dynamics algorithm
Figure 3-1 Energy versus volume of (a) Various Li crystals and (b) crystalline LiSi and Li ₁₃ Si ₄ predicted by DFT and ReaxFF calculation (Adapted from reference [⁵⁹]. Copyright © Modelling and Simulation in Materials Science and Engineering 2013)
Figure 3-2 (a) \sim (e) Structural snapshots and local concentrations profile at successive stages of lithiation of a-Si and (f) \sim (j) c-Si with (100) surface orientation. All snapshots are taken at 1200 K. In the figure, spheres in blue and green color represent Si and Li atoms, respectively 38
Figure 3-3 Structural snapshots of c-Si with (100) surface orientations with (a) no vacancy, (b) 5 % Li vacancy, (c) and 5 % Si vacancy after a reaction time of 10 ps at 1200 K. In the figure, spheres in blue and green color represent Si and Li atoms, respectively (d) The concentration profiles of the three snapshots. (e) Movement of reaction fronts with and without Si vacancies with respect to time at 1200 K
Figure 3-4 (a) Movement of reaction fronts with 2 %, 4 %, 6 %, 8 %, and 10 % Si vacancies with respect to time (b) Reaction rates with corresponding Si vacancy concentrations. All information was obtained during lithiation of c-Si with (100) orientation at corresponding Si vacancy concentration at 1500K
Figure 3-5 Radial distribution functions $g_{Si-Si}(r)$ at 1500K for c-Si with (100) orientation with 2 % and 8 % Si vacancies at (a) 1 ps and (b) 1 ns
Figure 3-6 Local concentration distributions with respect to (a) position at different time and (b) time at different positions at 1500 K. Concentration distributions respect to (c) position at different

time and (d) time at different positions at 1200 K. All concentration profile was obtained durin lithiation of c-Si with (100) orientation at corresponding temperature
Figure 3-7 (a) Diffusion coefficients of Li at different concentrations in logarithmic scale at 120 K. Diffusion coefficients with corresponding concentration upon lithiation from bulk a-Li _x Si represented by blue dots. Red dots represent data obtained from local MSD calculations from initially c-Si with (100) surface orientation (b) Comparison Li diffusivity at with first-principle calculation and experiment
Figure 4-1 Model setup . (a) Initial structure of fully lithiated a-Li _{3.75} Si thin film sandwiched between fully lithiated aluminum oxide a-Li ₈ Al ₂ O ₃ coatings, where spheres in yellow, green, real and blue represent Si, Li, O, and Al atoms respectively (b) The computed open circuit voltage for a-Li _x Si and a-Li _x Al ₂ O ₃ . Continuously removing Li from the coating layer outside of the buffer zone (white region) will generate the chemical potential driving force for the Li inside Si thin film to "naturally" diffuse out
Figure 4-2 Schematic representation of Connolly volume calculation with (a) probe (b) structure with internal pore smaller than single atom size and (c) system with internal pore larger than single atom size (considered as isolated-inner pore, region in yellow)
Figure 4-3 Atomic Structure Evolution. Structural snapshots at the specified delithiation step during the continuous delithiation process with the (a) - (c) fast and (d) - (f) slow rates. In the figure, spheres in yellow, green, red, and blue represent Si, Li, O, and Al atoms, respectively 6
Figure 4-4 Pore Structure Evolution. Structural snapshots of the pore structure and distribution in the highlighted a-Li _x Si region during continuous delithiation process with the (a) fast and (b) slow rate
Figure 4-5 Volume and Concentration Evolution. (a) The total volume (V_{total}) and trul occupied a-Li _x Si volume (V_{true}) change normalized with respect to the unlithiated Si and (b) I concentration and the pore volume contribution (V_{pore} / V_{total}), upon delithiation with the fast an slow rate
Figure 4-6 Difference in Amorphous Structures. (a) a-Li _x Si structures formed during delithiation have lower density than the equilibrium structures. Density corresponding to the delithiated a-Li _x Si upon delithiation with fast and slow rate are represented by blue and red dot Green dots represent density obtained from the equilibrium a-Li _x Si structures (b) RDF of g _{Si-Si} (at 900 K of delithiated a-Li _x Si upon delithiation with fast and slow rate and equilibrium a-Li _x Si all at concentration 2.8. Local concentration distributions at different stages of lithiation of (delithiated a-Si with slow rate and (d) equilibrium a-Si at 1200 K
Figure 4-7 Si Cage and Trapped Li. (a) Local Li concentration distribution at the final stage of delithiation with the fast (55 step) and slow (65 step) rate (b) Li motion tracking with various initial positions during fast delithiation. In the figure, Si and Li atoms are excluded to improve the clarity Spheres in green, red, and blue represent Li. O. Al atoms, respectively

Figure 5-1 (a) EELS profiles (Si-K edge) taken from the three different regions in the HAADF-STEM image (b) Experimental (a) - (c) and simulated (d) - (f) ABED images corresponding to Si ,SiO ₂ , and interface regions (Adapted from reference [¹³³]. Copyright © Nature Communications 2016)
Figure 5-2 Schematic of (a) random bonding and (b) random mixture a-SiO
Figure 5-3 Energy calculation of a-SiO _{0.5} , a-SiO, and a-SiO ₂ with equation of states
Figure 5-4 Formation energy of a-SiO with (a) DFT optimized and (b) ReaxFF-MD optimized structure. The red and blue data points represent DFT and ReaxFF-MD energy calculation, respectively
Figure 5-5 (a) Energy Comparison of random bonding and random mixture a-SiO with its unique microstructure. (a) - # represents the microstructure of a-SiO corresponding to the energy. In the figure, spheres in red and yellow represent O and Si atoms, respectively (b) Formation energy (ΔE_f) of a-SiO structures
Figure 5-6 Energy calculation using DFT and ReaxFF methods for (a) three different Si phases and (b) various silicon dioxide phases at different densities for ReaxFF fitting (Adapted from reference [⁷³]. Copyright © The Journal of Physical Chemistry A 2003)
Figure 6-1 Flow chart describing the automated protocol to construct the Li-Si training set 96
Figure 6-2 (a) Radial distribution function of c-Li ₁₅ Si ₄ and a-Li ₁₅ Si ₄ (b) Densities of a-Si, a-LiSi, a-Li ₁₂ Si ₇ , a-Li ₇ Si ₃ , a-Li ₁₃ Si ₄ , and a-Li ₁₅ Si ₄ calculated from ReaxFF-NPT simulations via melting-and-quenching process
Figure 6-3 Formation energies of crystalline and amorphous Li _x Si included in the training set. The training set is consisted of total 88201 structures
Figure 6-4 Experimental ^{34,42} and calculated OCV vs. composition curves of Li/Si system at high temperature (lines in red) and room temperature (curves in blue) (Adapted from reference [³⁴]. Copyright © Journal of the Electrochemical Society 2004)
Figure 6-5 Bulk modulus for a-Li _x Si with comparison with literature (DFT) ^{49,55}

Chapter 1 Background and Motivations

1.1 Li-ion Batteries and Silicon Negative Electrode

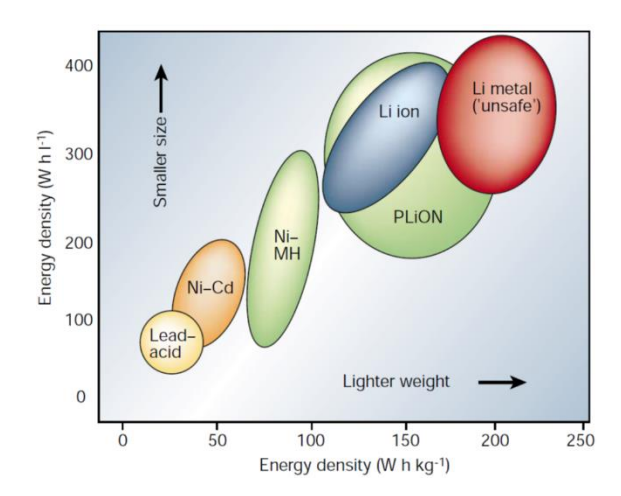


Figure 1-1 Energy density comparison of different batteries systems (Adapted from reference [¹]. Copyright © Nature 2001)

In the past few decades, Lithium-ion batteries have become the primary energy storage devices and power sources for portable electronics, power tools, and hybrid/full electric vehicles due to its high energy density, as shown in **Fig. 1-1**. To meet the increasing demand for large-scale energy storage, particularly for the applications to increasingly popular electric vehicles, it is necessary to significantly improve Li-ion batteries in terms of energy density, specific capacity, durability, safety, and cost. ^{1–3}

As represented in **Fig. 1-2**, in commercial Li-ion batteries, transition metal oxides or phosphates (LiCoO₂, LiMnO₂, LiFePO₄ etc.) are commonly used as the cathode (positive electrode) materials, while graphite is commonly used as the anode (negative electrode) material.

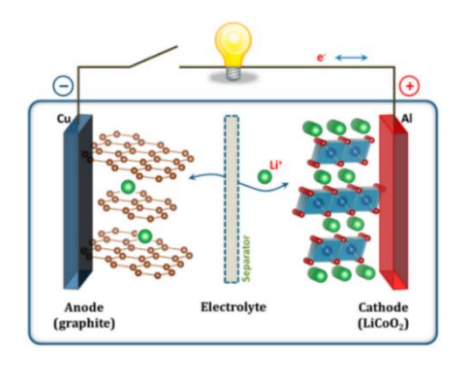


Figure 1-2 Schematic diagram of Li-ion batteries, which is composed of cathode (LiCoO₂), anode (graphite), electrolyte, and separator (Adapted from reference [³]. Copyright © Journal of Power Sources 2013)

Cathode and anode are separated by a porous separator filled with electrolytes, which prevents the electrical contact between the electrodes and allows Li-ion diffusion during charging and discharging process. In electrochemistry, anode refers to the electrode where oxidation is taking place. However, in the rechargeable battery system, oxidation takes place in both electrodes depending on whether the system is under charging and discharging. Therefore, in this thesis, anode is designated to be the electrode where oxidation is taking place during the discharge. During the charging process, two electrodes are externally connected to an electrical supply and electrons are released and externally moves from the cathode to the anode. Simultaneously, Li ions internally move in the same direction through the electrolyte and store the external energy in the form of chemical energy. The energy released during battery charging and discharging can be represented by the following equation

Energy =
$$\int V dq$$
 (1-1)

where V is the voltage and q is the amount of charge transferred.⁴ Since the amount of charge that can be reversibly stored in the electrodes (number of Li or electrons released from electrochemical

reaction at the electrodes) determines the battery capacity, developing novel electrode materials is crucial to enhance the battery energy density.

In terms of anode, graphite interacts with Li ions via an intercalation mechanism, where Li ions are inserted into and extracted from the interstitial sites provided by the layered graphite. The number of limited intercalation sites prevents significant structural changes, resulting in good capacity retention upon cycling. However, the limited number of intercalation sites within the graphite confines the theoretical specific capacity to 372 mAh/g.¹ The need for alternative anode materials with improved specific capacity motivated researchers to investigate novel electrode materials which interact with Li via an alloying mechanism. In contrast to intercalation mechanisms, alloying mechanisms proceeds via breakage of the bonds between the host atoms and formation of Li alloys. Since the reaction of the host material and Li are not limited by the atomic framework of the host material, significantly more Li atoms can be stored compared to intercalation electrode materials. ^{5,6}

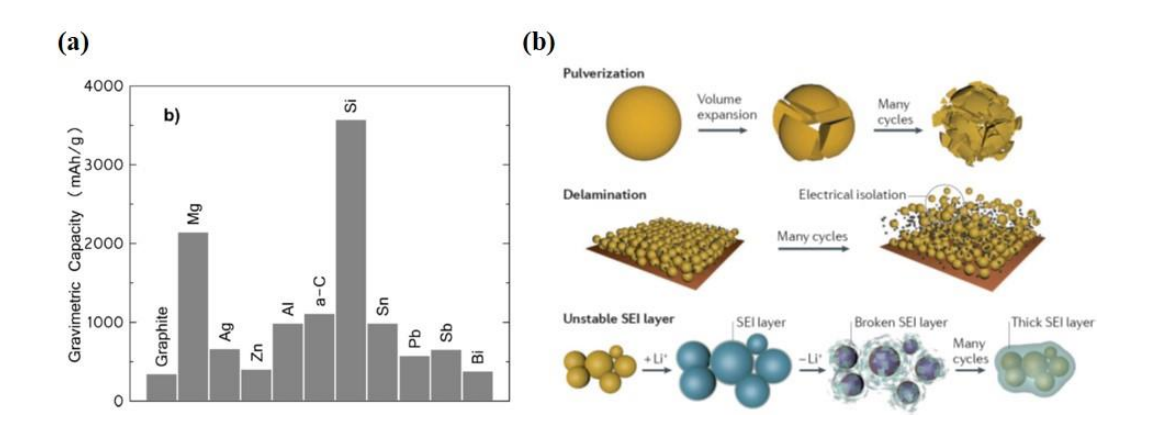


Figure 1-3 (a) Gravimetric capacity of different anode materials (Adapted from reference [⁶]. Copyright © Chemical Reviews 2014) (b) Degradation mechanism of Si anodes upon lithiation-driven volume expansion (Adapted from reference [⁷]. Copyright © Nature Reviews Materials 2016)

Among many alloying anode materials, Silicon (Si) is considered as a promising candidate because of its exceptionally high theoretical specific capacity (3750 mAh/g). Despite its high specific capacity, Si is limited in its application because of its 300 % volume expansion and massive structural change during lithiation/delithiation, caused by the large number of Li reacting with the Si. ⁸ This leads to mechanical fracture, formation of unstable solid electrolyte interphase (SEI), and disconnection between the particles, which all together contribute to the irreversible capacity loss and limited cycle life. ^{7,9–12}

To facilitate the practical implementation of Si anodes, various strategies have been employed to mitigate the mechanical degradation and improve the rate performance and capacity retention.^{7,12,23,15–22} As shown in **Fig. 1-4 (a)**, designing effective nano-structured Si (Si nanoparticles, ¹⁹ Si nanowires, ^{17,18} Si nanotubes, ^{21,22} Si nanospheres ²³) is a promising direction since they can efficiently alleviate the effect of dramatic volume expansion, which results in enhanced capacity retention and improved cycle life. However, reducing the size of Si to nanodomain induces another significant problem; increasing formation of Solid Electrolyte Interphase (SEI). ^{24–26} Due to high surface-to-volume ratio of nanostructures, much more surfaces are exposed to the electrolyte and form SEI layer. Furthermore, huge volume change of nanostructured Si continuously breaks the SEI layer and generate new surface exposed to the electrolyte, thereby constantly consuming active Li which causes rapid capacity loss and low current efficiency. To solve challenges rising from reducing the size of Si to nano-domain, researchers further engineered the nano-structures (Fig. 1-4 (c)) with intentionally designed voids 19 and developed composite materials in some form of carbon²⁷ or TiO₂ ²⁸ (**Fig. 1-4 (b)**). These unique designs accommodate the volume expansion without any outward expansion, thereby avoiding direct contact with the electrolyte and alleviating the SEI problem.

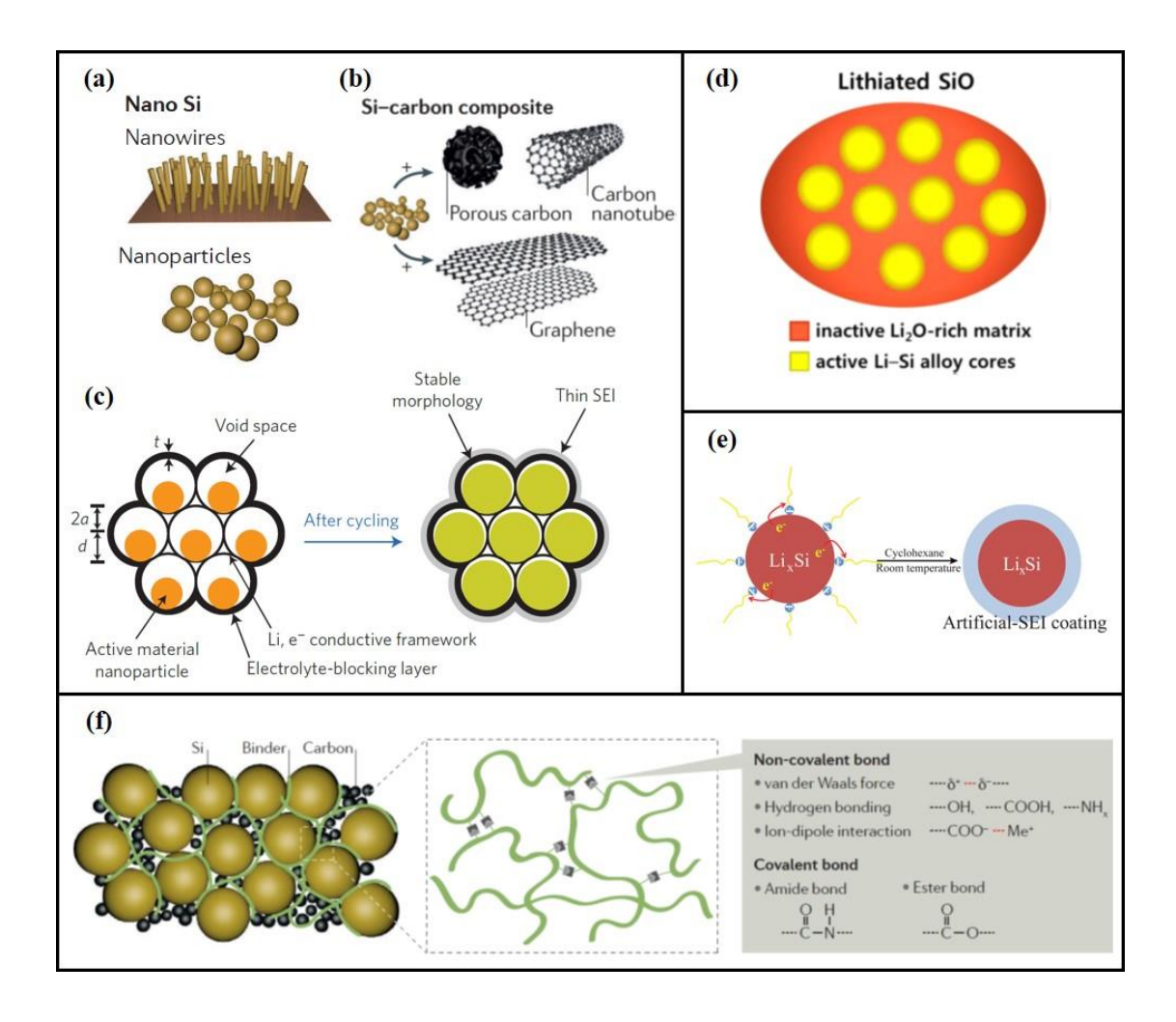


Figure 1-4 (a) - (c) Various morphologies of Si active materials and their composites (Adapted from reference [7,12]. Copyright © Nature Reviews Materials 2016) (d) Schematic of SiO_x composite anode in atomic-level (Adapted from reference [13]. Copyright © The Journal of Physical Chemistry C 2016) (e) Schematic describing the formation of the artificial SEI on Li_xSi nanosphere (Adapted from reference [14]. Copyright © Journal of the American Chemical Society 2015) (f) Illustration of Si binder concepts (Adapted from reference [7]. Copyright © Nature Reviews Materials 2016)

Utilizing composite form at atomic-level, such as Silicon Monoxide (SiO)²⁹, is another strategy to mitigate the effect of volume expansion (**Fig. 1-4** (**d**)). SiO is composed of inhomogeneous mixture of a-Si and a-SiO₂ in atomic-level where Li reacts with SiO to form several irreversible phases (Li₂Si₂O₅, Li₆Si₂O₇, Li₄SiO₄, and Li₂O), which act as buffering phases against the volume expansion during cycling. Even though the formation of irreversible phase

results in lower discharge capacity (~ 2200 – 2500 mAh/g) compared to Si, significantly reduced volume expansion (~ 160 %) enhances the capacity retention and cycle life of SiO. Usage of electrolyte additives and generation of effective surface passivation layers (artificial SEI layer)¹⁴ could be a valuable strategy to prevent the chemical degradation (**Fig. 1-4 (e)**). Finally, utilizing conductive binders, which is stiff, inert to electrolyte, and conductive to Li ions and helpful to stabilize SEI, also dramatically improve the cycle life (**Fig. 1-4 (f)**).^{7,30} For detailed information, see the review article by Choi *et al.* and Li *et al.* and the references therein. ^{7,12}

Along with the massive volume expansion, concurrently occurring upon electrochemical lithiation and delithiation of Si is the crystalline-to-amorphous phase transition.^{31–39} Solid-state amorphization results in characteristic reversible and irreversible structural evolution, chemical reactions, and diffusion of active materials which significantly affects the irreversible capacity loss, stress generation, and rate performance. Therefore, it is also important to investigate the thermodynamics and kinetics during electrochemical lithiation/delithiation of Si, which can be utilized to design battery with improved performance.

1.1.1 Thermodynamics and Kinetics of Electrochemical Reaction of Li with Si

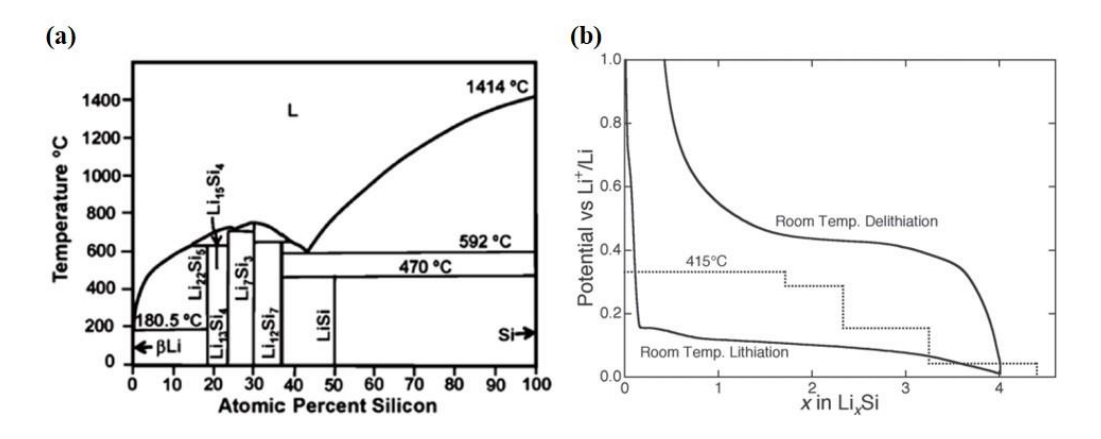


Figure 1-5 (a) Li-Si phase diagram (Adapted from reference [⁴⁰]. Copyright © Bulletin of Alloy Phase Diagram 1990) (b) Experimentally measured voltage vs. composition of Li-Si system.

Figure 1-5 (Cont'd)

Dotted curve represents the coulometric titration curve of Li_xSi at 415°C and solid curve represents the galvanostatic charge/discharge profile of Si powder electrode at room temperature (Adapted from reference [41,42]. Copyright © Journal of Solid State Chemistry 1981)

The reaction of Li and Si follows the equilibrium phase diagram (**Fig. 1-5 (a**)) at high temperature, forming intermetallic compounds with nominal composition of Li₁₂Si₇, Li₇Si₃, Li₁₃Si₄, and Li₂₂Si₅. ⁴⁰ The formation of equilibrium intermetallic compounds were confirmed by Wen and Huggins, ⁴² who used galvanic cell consisted of "LiAl"(s)|LiCl-KCl(eut.)|Li₉Si(s) to study the alloying process of Li-Si at high temperature (415 °C) using equilibrium coulometric titration technique. They observed four distinct voltage plateaus (**Fig. 1-5 (b)**, **dotted curve**), which clearly indicated the sequential formation of equilibrium intermetallic compounds corresponding to the composition of Li₁₂Si₇, Li₇Si₃, Li₁₃Si₄, and Li₂₂Si₅.

In contrast to the alloying process of Li-Si at high temperature, which follows the phase diagram, the electrochemical reaction of Si with Li at room temperature proceeds via non-equilibrium solid-state amorphization. Limthongkul *et al.* ^{31,32} observed a single voltage plateau during the lithiation of Si at room temperature (**Fig. 1-5 (b)**, **solid curve**) using X-ray diffraction and HREM. X-ray diffraction studies revealed the continuous formation of metastable amorphous Li_xSi phases instead of equilibrium intermetallic compounds, which serve as an evidence the electrochemical lithiation at room temperature is a non-equilibrium process. In other words, the electrochemical reaction of Si with Li at room temperature is kinetically controlled and since the formation of thermodynamically stable crystalline intermediate phases is circumvented, amorphous phases with lower Gibbs free energy than the reactant but higher than those of the equilibrium crystalline phases are formed.

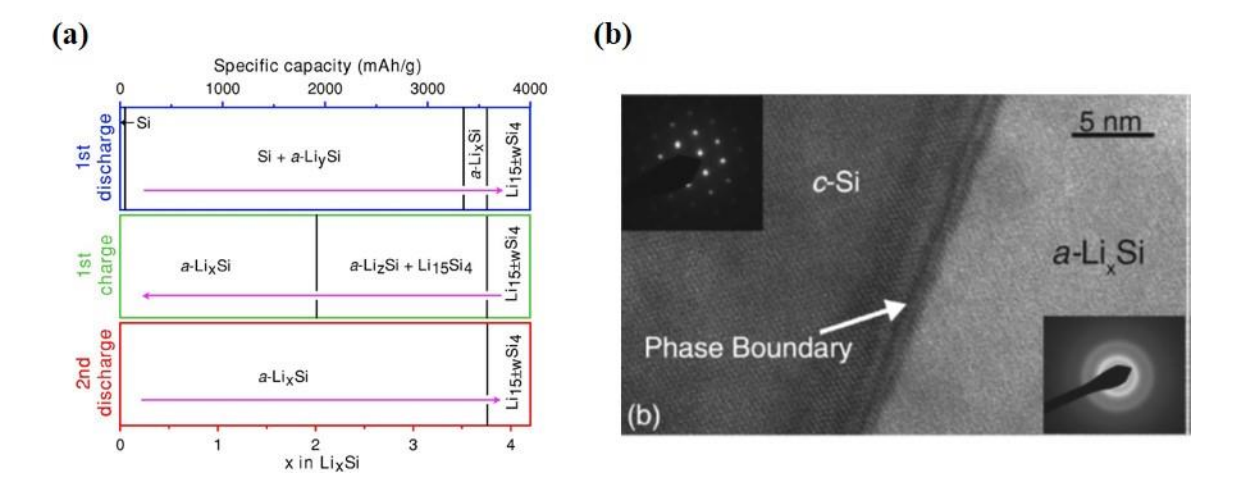


Figure 1-6 (a) Schematic diagram of phase evolution upon multiple cycle based on in situ XRD of charge/discharge cycles of Li-Si battery (Adapted from reference [³³]. Copyright © Journal of the Electrochemical Society 2007) (b) High-resolution TEM image of the sharp phase boundary between c-Si and a-Li_xSi (Adapted from reference [³⁷]. Copyright © Physical Review Letters 2011)

Further XRD³³, NMR^{35,36}, and TEM analysis³⁷ captured the reaction process with two-phase lithiation and recrystallization of highly lithiated a-Li_xSi phase into c-Li₁₅Si₄, as described in the schematic reaction diagram of c-Si (**Fig. 1-6 (a)**). Chon *et al.* ³⁷ observed a sharp phase boundary (~ 1nm) separating the crystalline silicon and amorphous lithium silicon using scanning electron microscopy and high-resolution transmission electron microscopy, which further confirmed the two-phase reaction, as shown in **Fig. 1-6 (b)**. To further investigate the local structural evolution in the two-phase region where crystalline Si and amorphous Li_xSi coexist, Key *et al.* ³⁵ used in situ and ex situ NMR techniques, followed by local structure probes and PDF analysis. ³⁶ Upon initial lithiation stage, Si bonds begins to dissociate and forms small clusters of Si surrounded by Li atoms. As time proceeded, these small Si clusters broke into isolated Si atoms, a reaction indicating complete crystalline-to-amorphous phase transition, which corresponded to the Li concentration of ~3.4. Further lithiation results in rapid crystallization of a-Li_xSi to c-Li₁₅Si₄, which is a characteristic phase transition observed only during electrochemical lithiation of Si at

room temperature.^{33,36} During delithiation, previously formed metastable c-Li₁₅Si₄ phase or a-Li₁₅Si₄ gradually disappears and are replaced by amorphous lithium silicon. NMR studies ^{35,36} indicate that the two-phase coexists until the terminal phase of the previous lithiation completely disappears and a single amorphous phase emerges towards the end of the delithiation process. Regardless of the initial phase of the Si (c-Si or a-Si), the resulting amorphous Si is different from the initial Si.

Recent development of in situ transmission electron microscopy (TEM) techniques enabled researchers to elucidate the local and detailed structural information which previously buried in the averaged properties. ^{16,43–47} By tracking the structural evolution of single Si nanoparticles or nanowire during lithiation, it was revealed that the short-range reaction and interfacial mobility controls the rate of phase transformation and determines the volume expansion pattern upon lithiation.

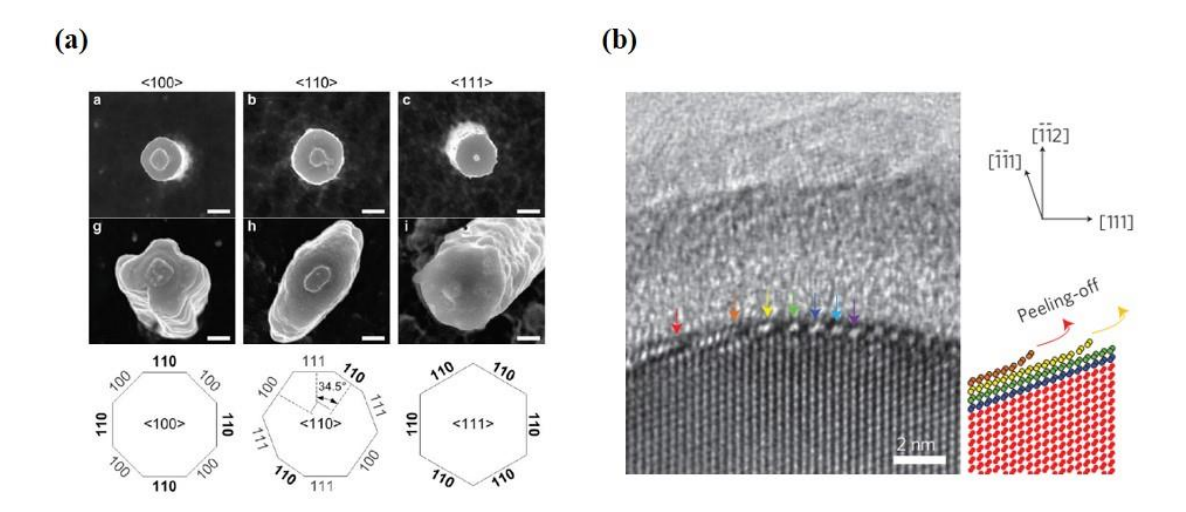


Figure 1-7 (a) Characteristic volume expansion of c-Si nanopillars along <100>, <110>, and <111> axial orientations upon lithiation (Adapted from reference [45]. Copyright © Nano Letters 2011) (b) High-resolution TEM image and schematic diagram describing the lateral ledge flow along {111} plane (Adapted from reference [43]. Copyright © Nature Nanotechnology 2012)

Lee et al. 45 examined the lithiation-induced shape and volume change of c-Si nanopillars with different crystallographic orientations and observed anisotropic expansion. This anisotropic expansion suggested that the rate of the phase transition strongly depends on the direction of Li insertion, <110> was shown to be the fastest and <111> the slowest. Liu et al. 44 reported anisotropic swelling of Si nano-wires during lithiation using in situ TEM, which further supported the idea that lithiation rate in c-Si is highly anisotropic. Furthermore, the movement of the sharp reaction front was linearly correlated with reaction time, suggesting lithiation is controlled by short-range reactions at the reaction front. Recently, Liu and coworkers⁴³ revealed the atomicscale mechanism of the lithiation process is characterized by a layer-by-layer peeling-off of {111} facets using in situ TEM. Taken together with finite element modeling, ¹⁶ it was determined that the rate of phase transformation and concurrently occurring anisotropic volume expansion upon lithiation is controlled by the short-range reaction and interfacial mobility. For a-Si, in situ TEM experiments 46,47 revealed unexpected two-phase lithiation behavior, which causes a different mechanism of stress evolution. During the first lithiation process, a sharp phase boundary of nanoscale thickness was observed which separated the a-Li_xSi region and unlithiated a-Si region. This indicated that lithiation in a-Si is limited by reaction front mobility, while less Li is required to break the Si-Si bonds in a-LiSi than to disrupt the rigid Si-Si covalent network in c-Si case. Upon lithiation, a-Si expands in an isotropic manner due to the lack of underlying crystallography. In subsequent lithiation/delithiation cycles, a single-phase mechanism was observed.

Experimental observations introduced above provide important information to understand the electrochemical lithiation/delithiation of Si. However, the inherent limitation of the experiment methods is that they only provide information related to the averaged properties over space and time. For instance, the important Li distribution information upon lithiation/delithiation cannot be

obtained. Also, detailed (local) structural evolutions at different lithiation/delithiation stages are difficult to study since even the most advanced in-situ TEM methods is not sensitive enough to capture the amorphous nature of a-Li_xSi. Computational investigation of Li-Si system in electronic and atomic level can provide fundamental knowledge regarding electronic and chemical properties, which information can be further utilized to better understand and predict reaction of Li with Si.

1.1.2 Computational Studies of Li-Si System

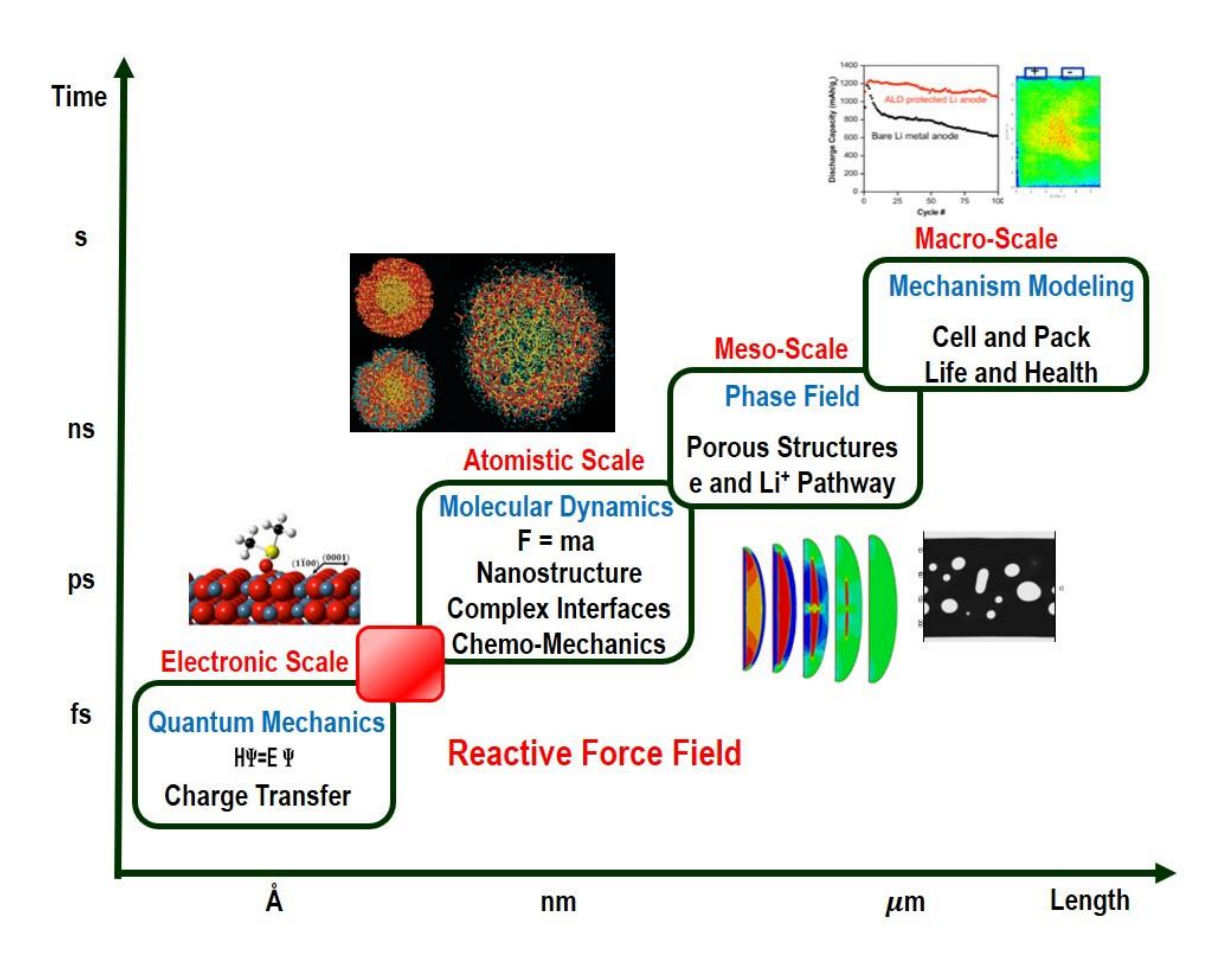


Figure 1-8 Multi-scale modeling and simulation

Computer simulations have become an important tool in essentially all fields of chemistry, condensed matter physics, and material science.⁴⁸ In principle, material properties and reaction

mechanisms can be describable by quantum mechanics (QM). However, simulations of large system size and dynamics time are impractical since solving the Schrödinger equation is computationally too expensive. Classical approximations lead to simplified equations of motion which describes the interaction between atoms and therefore, applicable to much larger system size and longer dynamic calculations without compromising the accuracy of the calculations. At the higher end of the length and time scales, continuum-level methods are widely used which provides insight into elucidating the behavior of matter at the microscale and macroscale. In this thesis, I only focus on the computational simulations on the electronic- and atomic-scale.

1.1.2. (a) Density Functional Theory Calculation of Li-Si

Characteristic material properties regarding the thermodynamic, electronic, kinetic, and mechanical properties of the bulk Li-Si system have been extensively studied with first-principle DFT calculations.^{49–58} Energetics, charges, diffusivities, and elastic constants of Li_xSi at certain compositions were calculated and the relationship between these properties at different Li concentrations was interpreted to obtain electronic and atomic level understanding of the Li-Si system.

To determine the structure and stability of Li-Si compounds, Chevrier *et al.* ⁵² computed the energies of Li_xSi structures at various Li concentrations and revealed the formation energy per Li_xSi constantly decrease upon Li insertion and reached its minimum around x = 3.75. Furthermore, Jung and Han⁵⁷ determined the crystalline-to-phase transition occurs during the initial stage of lithiation (x = 0.3) based on the formation energy comparison of a-Li_xSi and c-Li_xSi. Open-circuit voltage (OCV), which is another important parameter for lithiation experiments, were also computed from energies obtained from DFT calculations. As shown in **Fig. 1-9** (a), the computed

OCV curve of c-Li_xSi and a-Li_xSi compounds agreed well with the experiment which confirmed that essential physics and energetics of Si upon lithiation were successfully captured. 52,53

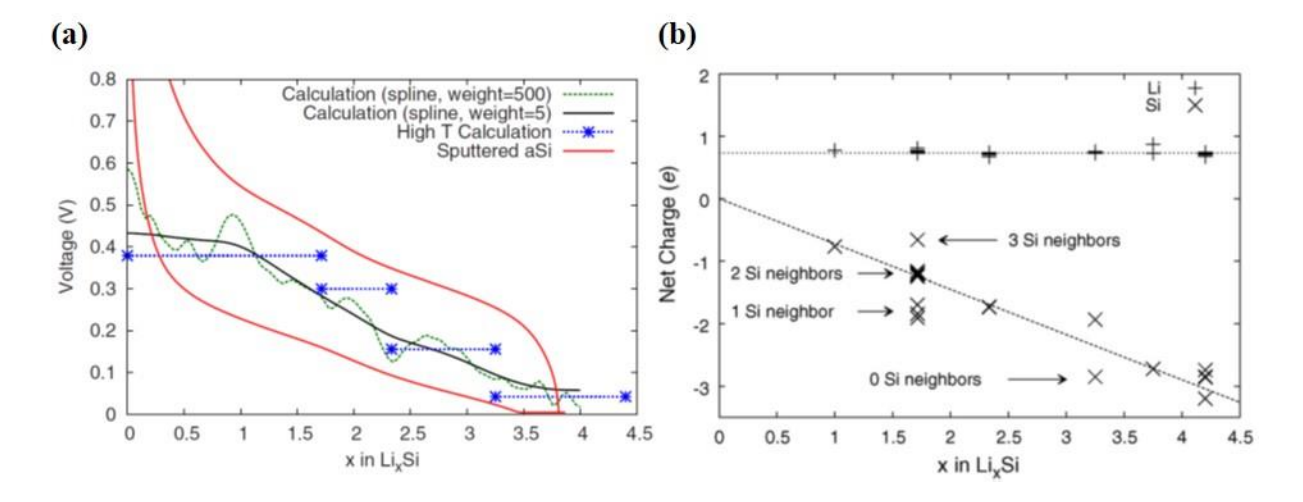


Figure 1-9 (a) Experimentally measured (red curve) and computationally calculated (blue, green, and black curve) voltage vs. composition of Li_xSi. (Adapted from reference [⁵²]. Copyright © Journal of the Electrochemical Society 2009) (b) Net charge of Li and Si in c-Li_xSi (LiSi, Li₁₂Si₇, Li₇Si₃, Li₁₃Si₄, Li₁₅Si₄, and Li₂₁Si₅). (Adapted from reference [⁵⁴]. Copyright © Journal of Alloys and Compounds 2010)

Another fundamental insight that can be obtained from first-principle calculations are the information regarding the charge transfer and electronic structure. Using Bader charge analysis, Chevrier *et al.* ⁵⁴ calculated the net charge of the Li and Si atoms at various c-Li_xSi, as shown in **Fig. 1-9** (b). They revealed regardless of the Li concentration, Li atoms have similar positive net charge of 0.73 e and 0.68 e. In contrast, the net charge of Si atoms decreases as the Li concentration increases, which clearly indicates Si net charge is strongly dependent on the local environment. In other words, decrease in Si net charge is due to the dissociation of Si-Si covalent bond and formation of Li-Si ionic bonds upon increased Li concentration.

To efficiently obtain the a-Li_xSi structures while avoiding the computationally expensive Ab Initio Molecular Dynamics (AIMD), Chevrier and Dahn^{52,53} successfully developed a protocol

based on Li insertion at energetically favorable sites followed by structural optimization. Using this self-developed lithiation algorithm, they were able to successfully generate a-Li_xSi structures which captured the volume expansion and OCV vs composition curve which agreed well with the experimental values. Chan *et al.*⁵¹ further improved the Li insertion protocol and performed Li insertion and removal simulation to study the complete lithiation/delithiation process of c-Si and discovered that Li insertion to c-Si with (110) surface orientations is thermodynamically more favorable than (100) and (111).

For mechanical properties, Shenoy *et al.*⁴⁹ calculated the elastic modulus of c-Li_xSi and a-Li_xSi. Bulk modulus, shear modulus, and Young's modulus for both c-Li_xSi and a-Li_xSi decrease linearly with increasing Li concentration, which indicated a softening effect as Li_xSi approached the Li-rich phases. Elastic softening phenomena upon increase in Li concentration is due to the breakage of strong covalent Si-Si bonds being replaced by weak ionic Li-Si bonds.

Finally, diffusion kinetics and local structural evolution upon lithiation was also computed using ab initio molecular dynamics (AIMD) simulations. Johari *et al.* ⁵⁶ investigated the Li-Si mixing mechanism upon lithiation from AIMD using a slab model with 1D diffusion and revealed that Li atoms convert the conventional 6-node-rings by interrupting the Si-Si covalent bonds. The structural evolution continued with time by forming temporary structures, which eventually evolved into isolated Si atoms and Si-Si dumbbells, as shown in **Fig. 1-10** (b) - (c). Furthermore, diffusivity calculations of Li and Si suggested that both Li and Si diffuse faster in a-Si than in c-Si and room temperature Li diffusivities, obtained by extrapolating high temperature results, is in good agreement with experimentally measured Li diffusivities. Recently, Wang *et al.* ⁵⁸ revealed Li diffusion increases with Li concentration with a linear trend based on calculated Li diffusivity at four different concentrations.

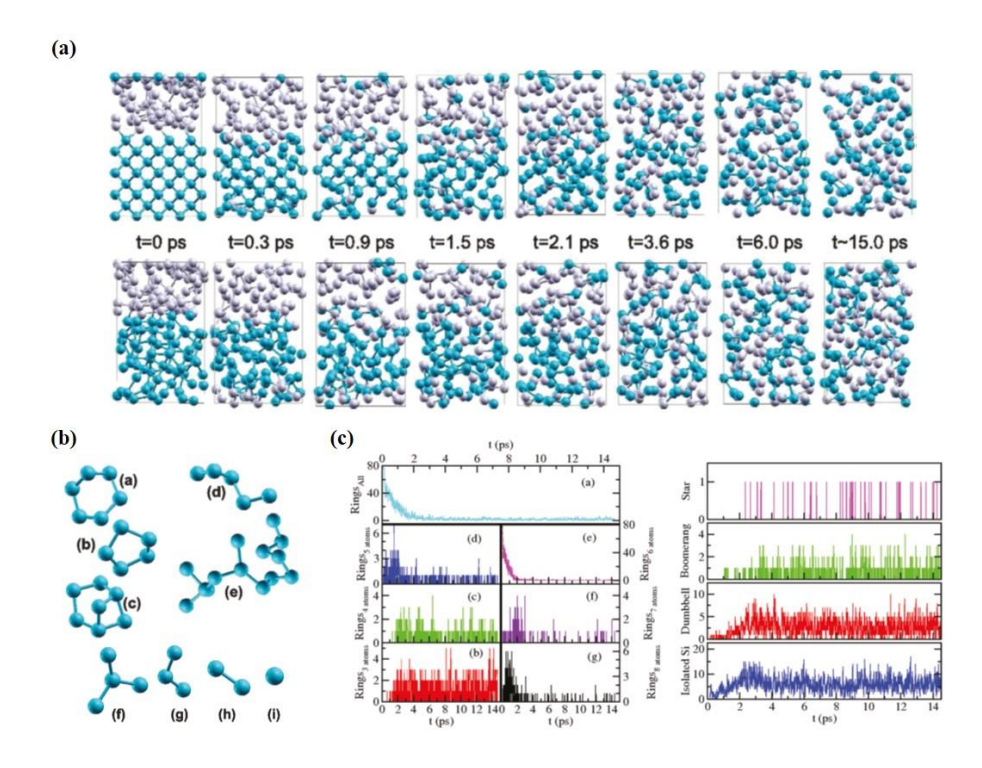


Figure 1-10 (a) Representative structural snapshots at various lithiation stages of c-Si (top) and a-Si (a-Si) at 1200K. Cyan and purple color spheres in the figure represent Si and Li atoms, respectively (b) Representation of structures form during lithiation (c) Structural statistics with time upon for lithiation of c-Si. (Adapted from reference [⁵⁶]. Copyright © Nano Letters 2011)

Although first-principle calculations of Li-Si system provides valuable fundamental insights of chemical, electronical, and mechanical properties, most of them are from static property calculation of Li_xSi compounds at equilibrium. Ab initio MD simulations describe the short-range local structural change characterized by breakage of Si clusters into isolated Si atoms. However, the simulation size is limited to ~ 100 atoms due to the computational cost, thus the information regarding the movement of reaction front and long-range structural evolutions are buried inside the immediate collapse (lithiation) upon mixing. ⁵⁶ In other words, within the scope of first-principle calculations, it is difficult to simultaneously track and correlate the chemical and structural evolution upon lithiation and delithiation. Atomistic simulation, which approximates

atoms as classical particles and replace the expensive quantum calculations with interactions between atoms, is a great alternative to study the dynamic evolution of large structures in time.

1.1.2. (b) Molecular Dynamics Simulation of Li-Si

Molecular Dynamics (MD) simulation, also known as atomistic simulations, can simulate over scales relevant to nanometers and nanoseconds. Therefore, it is considered as a promising alternative method to study the dynamic properties change but the usage was restricted in Li-Si system due to the lack of accurate interatomic potentials to describe the chemical reactions between Li and Si. Recently, van Duin and coworkers^{59–61} developed a reactive fore field (ReaxFF) for Li-Si system, which accurately describes the bond breaking and bond formation processes, thus providing a set of reliable properties for Li_xSi alloys including chemical reactions, volume expansion, and open-cell voltage.

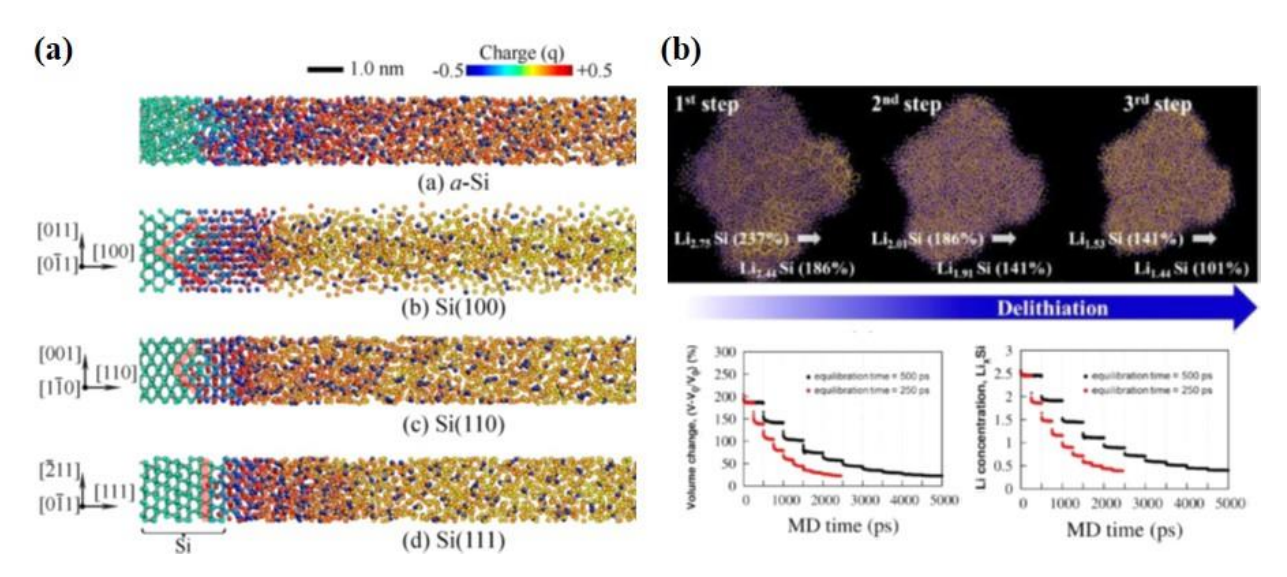


Figure 1-11 (a) Structural snapshot representing the lithiation of a-Si and c-Si with (100), (110), and (111) surface orientations after 200 ps at 1200K using ReaxFF-MD simulations (Adapted from reference [⁶²]. Copyright © The Journal of Physical Chemistry C 2014) (b) Structural snapshot representing the delithiation of lithiated Si NW with MD equilibration time of 250 ps (red) and 500 ps (black) for each delithiation steps (Adapted from reference [⁶³]. Copyright © The Journal of Physical Chemistry C 2015)

Motivated by in situ TEM experiments, which revealed the phase boundary, Kim et al. 62 investigated the formation and propagation of phase boundary for c-Si with different orientations. They revealed the phase boundary depends on the orientation of c-Si, where the location of the (111) plane governs the rate of crystal-to-amorphous phase transformation and the thickness of the phase boundary. Ostadhossein et al. 64 also studied the Li insertion process into c-Si nano-wires using ReaxFF and revealed the atomistic mechanism of the crystalline-to-amorphous phase transformation. They also demonstrated that Li diffusion-induced compressive stress can slow down the lithiation process. The consistency with experiments validated the ability of ReaxFF to capture the room-temperature electrochemical reactions of the Li-Si system. Jung et al. 63 simulated the delithiation process by removing the Li atoms from the surface of a-Li_xSi to generate a Li concentration gradient, which served as the driving force for delithiation. They revealed the formation of c-Si nuclei in the delithiated a-Li_xSi matrix and demonstrated that the volume of delithiated a-Li_xSi is larger than the original Si volume. However, removing all the Li from the surface abruptly disrupted the surface structure and may prevent a "natural" delithiation response in terms of volume contraction, structural evolution, Li diffusion in the Li-Si system.

These experiments and computational studies have investigated the reaction of Si upon lithiation/delithiation, but there are still important information missing regarding the lithiation rate and the origin of the irreversible capacity loss.

Lithiation rate is one of the most important factors that determines the performance of Liion battery since it significantly impacts the stress generation and determines the rate performance. In order to improve the rate performance by accelerating the lithiation rate, it is crucial to elucidate the rate-limiting factor upon lithiation. Also, the effect of Li concentration on Li diffusivity, which affects the lithiation rate on different stages of lithiation, remains unclear. The origin of the irreversible capacity loss that are inherent at atomic-scale is another key factor missing to understand the high irreversible capacity loss. Typically, initial irreversible capacity loss is responsible for the poor capacity retention in Si anode. In other words, besides the consumption of Li atoms in SEI layer formation and other side reactions, the irreversible capacity loss is mainly due to the chemical and structural evolution during the delithiation. So far, simulation of delithiation is in its infancy level since an effective delithiation procedure to successfully mimic a "natural" delithiation response is absent. Therefore, a systematic delithiation algorithm needs to be developed and utilized to simulate the delithiation process which can simultaneously track and correlate the irreversible chemical and structural evolution with rate effects.

1.2 Motivation and Thesis Outline

The goal of this thesis is to use electronic and atomic-scale simulations to obtain atomic insights on the lithiation mechanism to accelerate rate performance, elucidate the irreversible changes that are inherent at atomic-scale upon delithiation with rate effects for Li-Si system. Furthermore, we will evaluate the reactive force field for application to SiO system and lay down the ground work to design extensive training set of Li-Si system for machine-learning potential development.

In Chapter 2, computational tools and methods are introduced. Basics of density functional theory and molecular dynamics with force field are explained in detail.

Chapter 3 presents the ReaxFF-based molecular dynamics to elucidate the rate-limiting factor upon lithiation of Si for accelerated lithiation rate. Fundamental insights on lithiation dynamics of c-Si with different orientations and a-Si were extensively studied and the effect of Li

concentration on Li diffusivity were revealed. Also, based on the determination of the rate-limiting factor, methods to enhance the lithiation rates are introduced.

Chapter 4 focuses on understanding the irreversible changes that are inherent in atomic-scale upon delithiation. To quantify the 'natural' irreversible structural and chemical evolution upon delithiation, we first developed a continuous reactive molecular dynamics delithiation algorithm, with well-controlled chemical potential gradient driving force and delithiation rate. With this new systematic delithiation algorithm, the fundamental reasons behind initial irreversible capacity loss was investigated by analyzing the relationship between the depth of discharge and corresponding volume and structural changes at different rates. Furthermore, the effect of irreversible structural changes on subsequent lithiation processes was also studied.

In Chapter 5, the reactive force field developed for Li/Al/Si/O/H system are evaluated for application to simulate lithiation/delithiation of SiO system. The phase stabilities of SiO_x structures are computed against DFT calculations and design of the training set for modified Li/Si/O parameters are suggested.

Chapter 6 presents the development of accurate and extensive training set for the next-generation machine-learning potentials for Li-Si system. Based on Ab Initio Molecular Dynamics and DFT optimization procedure, systematic strategy to generate Li-Si training set with minimum human intervention are developed and the quality of the training set is also evaluated.

Finally, Chapter 7 presents a summary of the research work and discusses future research direction.

Chapter 2 Overview of Computational Methods

2.1 Energy Calculation using DFT and Force Fields

2.1.1 Density Functional Theory

First principle calculations describe the interaction of electrons by solving Schrödinger equation. Born-Oppenheimer approximation⁶⁵ states that the motion of nuclei and electrons can be separated since electrons move much faster than nuclei, thus nuclei can be treated as stationary. Based on Born-Oppenheimer approximation, atomic positions are treated to be fixed and wave functions are used to solve the Schrödinger equation which describe the motion of electrons. The time-independent Schrödinger can be expressed as

$$H\psi = E\psi \tag{2-1}$$

where H is the Hamiltonian operator, E is the energy operator, and ψ is the wave function. In case where the Hamiltonian has a simple form, such as hydrogen system, Schrödinger equation can be exactly solved. However, it is impossible to solve Schrödinger equation with multiple nuclei and electrons. For complicated systems with multiple nuclei and electrons, Schrödinger equation can be expressed as

$$\left[-\frac{\hbar^2}{2m} \sum_{i=1}^{N} \nabla_i^2 + \sum_{i=1}^{N} V(r_i) + \sum_{i=1}^{N} \sum_{j=i}^{N} U(r_i, r_j) \right] \psi = E \psi$$
 (2-2)

where m and N refers to the mass of electron and total number of electrons. The three terms in brackets refer to the energies corresponding to, in order, kinetic electrons, interaction between each electron and atomic nuclei, and electron-electron interactions. Among various methods to solve Schrödinger equation with multiple nuclei and electrons, density functional theory (DFT) is one

of the most widely used method due to its efficiency. DFT⁶⁶, first proposed by Kohn and Hohenberg in 1964, is based on two key theorems:

The ground-state energy from Schrödinger's equation is determined by a unique functional
of the electron density

$$\mathbf{n}(\mathbf{r}) = 2\sum_{i} \psi_{i}^{*} \psi_{i}(\mathbf{r}) \tag{2-3}$$

2. The correct electron density, which describes the ground-state, minimizes the energy of the overall system

Based on these theorems, Kohn and Sham developed DFT which reduces the intractable interactions of many electrons to a tractable functional of the electron density. Using DFT, time-independent Schrödinger equation (eqn. 2-1) can be describe by a wave function

$$\left[-\frac{\hbar^2}{2m}\nabla^2 + V(r) + V_H(r) + V_{XC}(r)\right]\psi_i(r) = \varepsilon_i\psi_i(r)$$
 (2-4)

where the first term is defined as the kinetic energy of electrons, V(r) is the sum of electron interaction, $V_H(r)^{66}$ is the electron-electron interaction and the self-coulombic interaction energy. Exchange-correlation contributions, $V_{XC}(r)^{66}$, describes the interaction between electrons which is difficult to capture in DFT since DFT treats electrons as a functional of electron density. $V_{XC}(r)^{66}$ is defined as a function derivative of XC energy

$$V_{XC}(r) = \frac{\delta E_{XC}(r)}{\delta n(r)}$$
 (2-5)

The exact form of exchange-correlation term is unknown. Therefore, various approximate functionals of electron density, such as local density approximation (LDA), generalized gradient approximation (GGA), are applied to describe this term. All DFT calculations performed in this

thesis uses Perdew-Burke-Ernzerhof (PBE) functional (a class of GGA), which utilizes both electron density and its gradient.

In DFT, plane wave basis sets are used to represent the electronic wave functions;

$$n_m(r) = \frac{1}{\sqrt{\Omega}} \sum_G c_m(G) \exp(iGr)$$
 (2-6)

where Ω is the normalization factor (volume of the box), G is the reciprocal lattice vector and r is the real space position. For practical application, we must basis sets must be truncated since DFT calculation with infinite plane-wave basis sets are difficult to perform. In this purpose, I utilized the cut-off energy in our DFT calculations and kept it constant throughout different calculations

$$\frac{1}{2}|G|^2 \le E_{cut} \tag{2-7}$$

Also, in our simulation (periodic system), integrals over the first Brillouin Zone in reciprocal space was used. Rather than integrating all the possible K-points, I carefully selected representative points (KPOINTS) with convergence test, to maintain high computational efficiency.

2.1.2 Force Fields

2.1.2. (a) Introduction

Force Field is a collection of functional forms and parameter sets, which is used to determine the energetics of large number of atoms (beyond the scope of DFT) at a reasonable computational cost. Based on Born-Oppenheimer approximation, computationally expensive electronic calculations are ignored and only the motions of the nuclei are utilized to describe the energy of the system. Additivity and transferability are two characteristics which defines a force

field. ^{69–71} Additivity means that the system energy can be expressed as sum of different energy contributions corresponding to bonded and non-bonded interactions. Transferability indicates the ability of the force field to use a force field developed for a specific atomic environment to describe a much larger atomic system with similar chemical environments. Although force field can efficiently capture the energetics based on atomic interactions, it is impossible to correctly translate all the quantum mechanical effects into one optimal set of functionals and parameters. Therefore, based on the system (covalent, ionic, metallic, etc.) of interest, different types of force fields with unique functional forms and parameters (empirical or from first-principle calculation) are designed. Classical force field^{69–71} and Reactive force field (ReaxFF)^{61,72–74} are two main type of force field which is widely used. Therefore, in the following section, Classical and Reactive force fields are introduced.

2.1.2. (b) Classical Force Field

Classical force fields, such as AMBER, CHARMM, and GROMOS, are mainly used in the field of chemistry and biochemistry, which focus on describing the covalently bonded system. Most classical force fields can be expressed as potential energy terms corresponding to deformation of bond and angles, rotation of dihedral angles, van der Waals interactions, and electrostatic interactions, ^{69–71} as shown in **Fig. 2-1**. The first three terms in the equation above represent covalently bonded terms, which corresponding energies are described with a simple harmonic potential of a force constant, equilibrium, and actual distance, angle, and torsion. First, second, and third term represents the energy contribution of deformation of bond, angle, and rotation of dihedral angle (torsion). The fourth and fifth term in the equation represent the non-bonded terms. The fourth term represent the contribution of van der Waals interaction, which

includes both attractive and repulsive term. The fifth term describes the Coulombic potential (electrostatic interaction) and are calculated by using charge equilibration (QEq) method. ⁷⁵

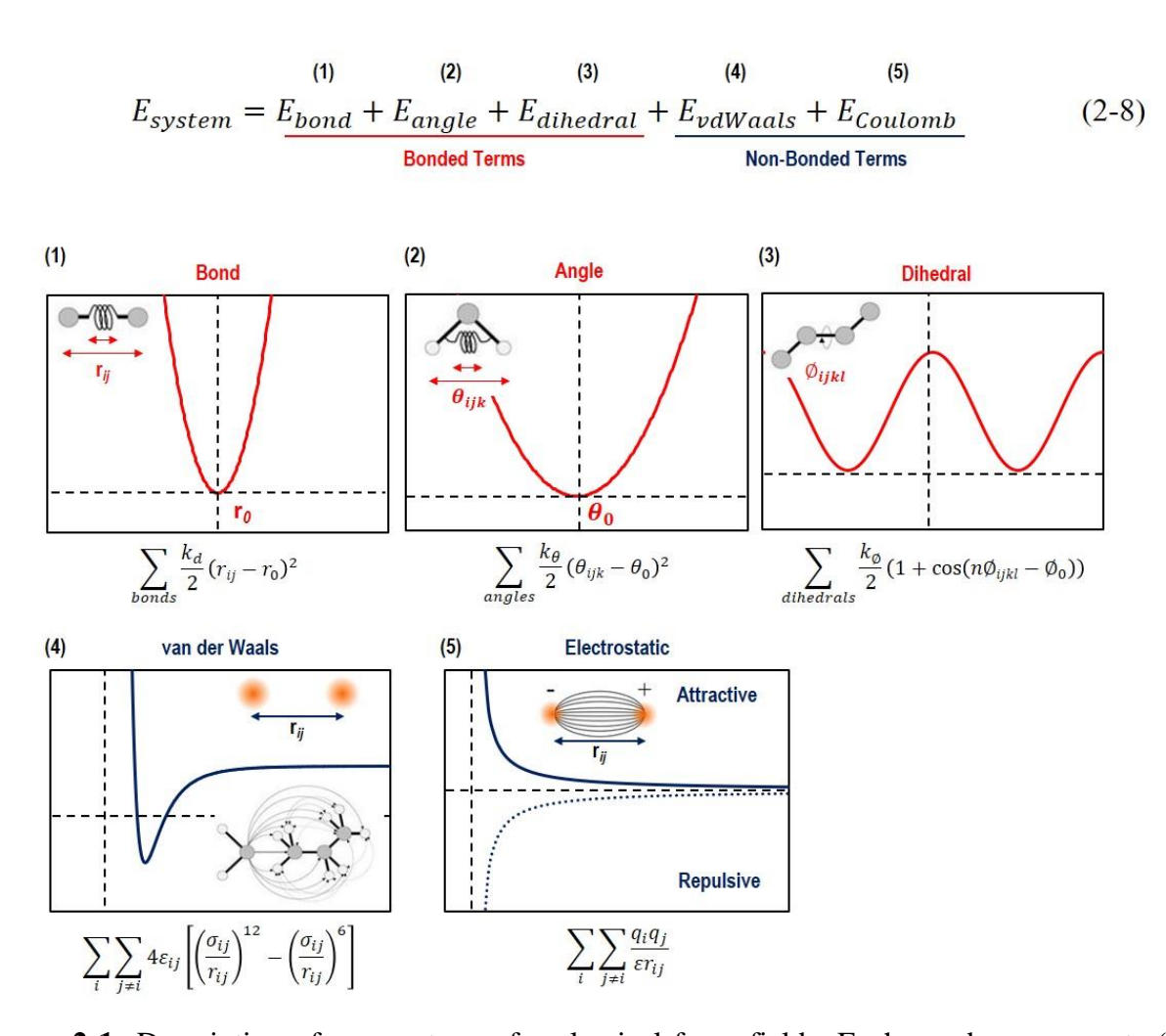


Figure 2-1 Description of energy terms for classical force fields. Each number represents (1) Bond, (2) Angle, (3) Dihedral, (4) van der Waals, and (5) Electrostatic contribution

Calculation involving classical force field successfully describe the non-reactive interactions near equilibrium. However, rigid functional form (harmonic) employed in the classical force field are inadequate for modelling chemical reactions with change in connectivity. For example, simple harmonic potential is applied to describe the angle and torsion interactions regardless of the strength of the bonds, thus important bond formation and dissociation can't be

captured or simulated using classical force field. Simulating chemical reactions can be achieved through the "Reactive Force Field".

2.1.2. (c) Reactive Force Field

$$E_{system} = E_{bond} + E_{over} + E_{under} + E_{lp} + E_{val} + E_{tor} + E_{vdWaals} + E_{coulomb}$$
 (2-9)

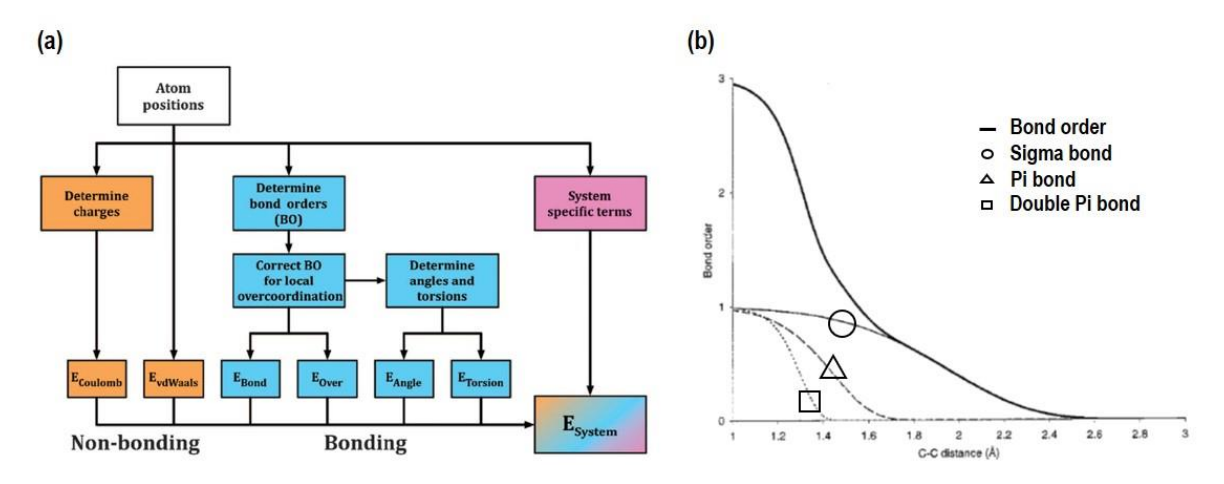


Figure 2-2 (a) Overview of the ReaxFF total energy components⁶¹ (b) Interatomic distance dependency of the carbon-carbon bond order⁷²

Energy contribution of ReaxFF can be expressed as shown in **Eqn. 2-9**, where each term represents bond deformation, over-coordination penalty, under-coordination stability, lone-pair, valence angle, torsion, and non-bonding van der Waals and Coulombic energies, respectively. ^{60,61} Different from classical force field, ReaxFF utilizes a bond-order dependent scheme to model the interactions between different atoms, as describe in the schematic in **Fig. 2-2 (a)**. By converting the bond distance to bond order, ReaxFF is able to dynamically describe the atomic interaction without predefined reactive sites. ⁶¹ The relationship between the bond distance and bond order are illustrated in **Eqn. 2-10**, where each exponential term represent the contribution from single, double, and triple bonds;

$$BO_{ij} = exp\left[p_{bo,1} \cdot \left(\frac{r_{ij}}{r_0\sigma}\right)^{p_{bo,2}}\right] + exp\left[p_{bo,3} \cdot \left(\frac{r_{ij}}{r_0\pi}\right)^{p_{bo,4}}\right] + exp\left[p_{bo,5} \cdot \left(\frac{r_{ij}}{r_0\pi\pi}\right)^{p_{bo,6}}\right]$$
(2-10)

where r_0^{σ} , r_0^{π} , and $r_0^{\pi\pi}$ represent equilibrium bond distance of single, double, and triple bonds. Each p term represents parameters obtained from first-principle calculations to successfully capture bond strength and corresponding energies for species that are r_{ij} apart. **Fig. 2-2 (b)** illustrates an example of unique ReaxFF bond order scheme for carbon-carbon interaction⁷², which highlights a smooth transition from nonbonded to single, double, and triple bonded system due to bond order dependent scheme.

In terms of non-bonded interactions, ReaxFF uses electronegativity and hardness parameter to calculate the charge transfer within the system. Based on EEM⁷⁶ and QEq⁷⁵ methods, charges are at each time step are calculated using geometry-dependent scheme, and further utilized to determine the Coulombic interactions. Also, different from classical force field which only calculates the non-bonded interactions between atoms that are not directly connected, ReaxFF calculates Coulombic and van der Waals interactions between all the atom pairs. To prevent excessive repulsion and attraction, ReaxFF employs a shielded term and corrects the interactions at short distance.

2.2 Molecular Dynamics

2.2.1 Ab Initio MD and Force Field based MD

Molecular Dynamics (MD) is a computer simulation method to study the thermodynamics and dynamic properties of a system by tracing the motion of atoms based on statistical mechanics. MD consider atoms as classical particles and determines the dynamic evolution by numerically solving Newton's equations of motion which can be expressed as

$$F_i = m_i a_i \tag{2-11}$$

where F_i is the force acting on an atom, m_i is the mass, and a_i is the acceleration of atom i. The potential energies and forces between atoms are calculated via DFT or force fields.

In this thesis, the first is referred as Ab Initio MD (AIMD) and later is referred as classical MD (with classical force field) or reactive MD (with reactive force field). In Ab initio MD, instead of using a prescribed potential, one solves the interatomic forces at a given time instant as follows. From a quantum-mechanical perspective, the system at a fixed time can be parametrized in terms of the coordinates of the nuclei and the relevant electrons. Based on Born-Oppenheimer approximation, the nuclei can be considered fixed and the time-independent Schrödinger equation can be written as the many-body wave function of the electrons. This Schrödinger equation is then solved using (time-independent) DFT to obtain the energy. The energy is then considered to be a function of the nuclear coordinates that were fixed earlier, and it can thus act as the interatomic potential that is needed to compute the forces in Newton's equation of motion for the nuclei. So, by computing the gradients of the DFT energy at this fixed point with respect to the nuclear coordinates, forces are obtained and the nuclei are moved according to get to the next time step. The DFT process is then repeated with these new nuclear coordinates. The difference between Ab Initio MD and force field based MD results from how the forces to describe the Newton's equation of motion are determined. In the standard MD approach, the instantaneous force on each atom is calculated as a gradient of a prescribed interatomic potential function (or, in other words, force field), which is function of the atomic coordinates that you can equally well regard as the coordinates of their nuclei. By avoiding computationally expensive electronic calculation with efficient force field, much larger system with longer dynamic simulation can be perform.

Ab initio MD and force field based MD approaches differ significantly in terms of the ability and computational cost due to the calculation method. Ab initio MD calculates the forces by on-the-fly from accurate electronic structure calculations, which intrinsically captures the bonding, charge transfer, polarization, and many-body effects. However, simulation with only small system sizes and short simulation time can be utilized due to significant computational cost. In force field based MD, one of the most challenging aspects is the accuracy of the calculation since empirical potential functions can't correctly translate all the quantum mechanical effects into one optimal set of functionals and parameters. Also, force fields can only describe the environment which it learned from and it is difficult to extrapolate to configurational space not included in the training set. Despite the limitation rising from force fields, MD with force field can simulate much larger system size with longer simulation time, thus providing valuable information regarding the phase, structures, and dynamics at a reasonable accuracy to compromise.

2.2.2 Equation of Motions and Thermodynamic Ensembles

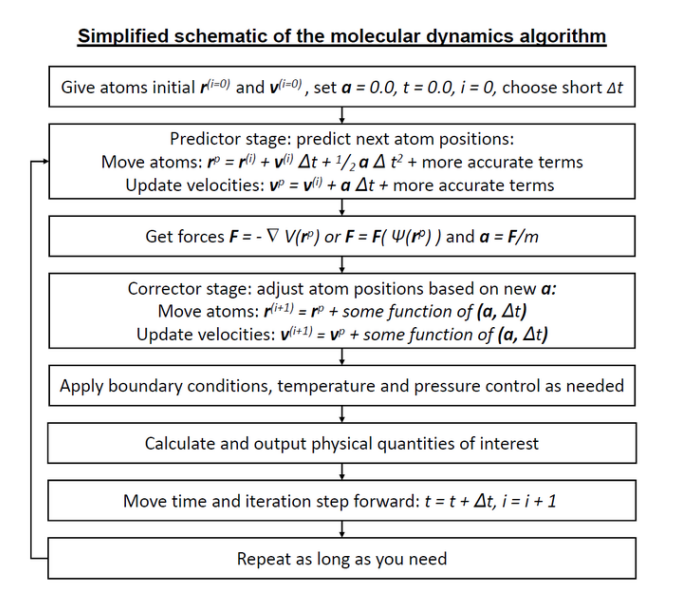


Figure 2-3 Illustration of molecular dynamics algorithm

Flow chart in **Fig. 2-3** describes the MD algorithm. Initially, the positions and velocities of atoms are specified, which propagates with a finite time interval using numerical integrators, such as Verlet algorithm.⁷⁷ By integrating Newton's law of motion, the position, velocities, and forces of each particles at different time in the system can be determined. As the particle moves, averaged properties including thermodynamic information, phase transition, structural evolution, and diffusion dynamics are obtained by analyzing the movement of the atoms (trajectories).

Various thermodynamic conditions can be simulated by controlling three thermodynamic state variables: Pressure (P), Volume (V), and Temperature (T). NPT ensemble, also known as isothermal-isobaric ensemble, represents a simulation condition where the pressure and temperature are controlled to be constant. It is mainly used to reproduce the experimental condition, where correct pressure and densities are important. NVT ensemble (canonical ensemble) is used to simulate a thermodynamic condition with constant volume. Similarly, for constant volume and total energy, NVE ensemble (microcanonical ensemble) is utilized.

Chapter 3 Vacancies in Si Can Improve the Concentration-Dependent Lithiation Rate

3.1 Summary

The study of lithiation dynamics is important since it affects both stress generation and rate performance of electrodes for Li-ion batteries. This topic becomes more crucial for Si anodes because its high capacity is accompanied by dramatic volume and structural changes, which lead to mechanical fracture, capacity loss, and limited cycle life. In order to provide fundamental insights into the lithiation dynamics, determine the rate-limiting process of lithiation, and investigate the effect of concentration on Li diffusivity, molecular dynamics (MD) along with reactive force field (ReaxFF) was used to simulate the lithiation process of both amorphous and crystalline Si electrodes. The local lithiation concentration evolution shows that lithiation dynamics can be characterized as two stages: an initial mixing stage followed by subsequent random walk diffusion stage. The Li diffusion is demonstrated to be concentration dependent as Li diffuses faster with higher Li concentration, opposite to many intercalation compounds. The degree of Li diffusivity increment with respect to Li concentration increases dramatically around Li_{0.8}Si. This relationship provides an underlying reason for the experimentally observed two-phase lithiation in both c-Si and a-Si. Furthermore, it is found that the lithiation rate during the initial mixing stage increases exponentially with vacancy concentrations in Si. This relationship reveals that the Si-Si bond breaking is the rate-limiting factor for Si lithiation.

This chapter is reproduced from the work published as: Kwang Jin Kim, Yue Qi, "Vacancies in Si Can Improve the Concentration-Dependent Lithiation Rate: Molecular Dynamics Studies of Lithiation Dynamics of Si Electrodes," The Journal of Physical Chemistry C 2015, 119, 24265-24275.

3.2 Introduction

Si is considered as a promising anode material due to its exceptionally high theoretical specific capacity (3750 mAh/g) and abundancy, which is promising in terms of its availability for future usage. Despite its high specific capacity, Si is limited in its application due to its 300 % volume expansion and massive structural change during lithiation and delithiation, caused by the large number of Li reacting with the host material. This leads to mechanical fracture and disconnection between the particles, which contributes to the irreversible capacity loss and limited cycle life. ^{7,9–12}

It is important to understand the fundamental aspect of lithiation/delithiaton dynamics since the stress generation and rate performance are significantly affected by the diffusion of Li and the host materials in alloy forming electrodes. During the lithiation process, Si undergoes enormous structural changes accompanied by significant changes in electronic and mechanical properties. Experiments, including X-ray diffraction (XRD), nuclear magnetic resonance (NMR), and acoustic emission have traced and revealed the evolution of averaged chemical bonding and structural change during Si cycling. ^{31–39} It has been shown that electrochemical lithiation of crystalline Si (c-Si) at room temperature involves solid-state amorphization. Due to this phase transformation, c-Si particles have shown more fractures during amorphization than during subsequent cycling. To avoid initial cracking due to amorphization, amorphous Si (a-Si) electrodes are preferable in practical battery applications. Thus, understanding the difference between the lithiation dynamics in a-Si and the lithiation dynamics in c-Si is not only scientifically interesting but also practically important.

Recent development of *in situ* transmission electron microscopy (TEM) techniques which tracked the structural evolution of single Si nano-particles or nano-wires during lithiation, revealed that the rate of phase transformation and concurrently occurring anisotropic volume expansion upon lithiation is controlled by the short-range reaction and interfacial mobility. Similarly, the initial lithiation of a-Si proceeds via two-phase lithiation which highlights the reaction front limited diffusion. ^{16,43–47}

In the field of theoretical research, initial simulations on the lithiation process of both c-Si and a-Si relied on first-principles calculations, which characterized and predicted diffusion energy barriers, formation energies, and elastic properties. ^{49–58} More specifically, *ab initio* molecular dynamics (AIMD) simulations were used to gain fundamental insights on the lithiation dynamics at the atomic level. ^{56,58} Johari *et al.* ⁵⁶ investigated the Li-Si mixing mechanism upon lithiation of c-Si and a-Si from AIMD using a slab model with 1D diffusion and revealed that structural evolution proceeds by Li atoms interrupting the Si-Si covalent bonds and eventually evolves into isolated Si atoms and Si-Si dumbbells. Further radial distribution functions and pair distribution function analysis indicate AIMD successfully capture the lithiation-induced amorphization. Diffusivity calculation of Li and Si suggested that both Li and Si diffuse faster in a-Si than in c-Si.

To further investigate the lithiation behavior with larger system size and longer dynamics, Kim *et al.* ⁶² investigated the formation and propagation of phase boundary for c-Si with different orientations using ReaxFF-based MD simulations. They revealed the phase boundary depends on the orientation of c-Si, where the location of the (111) plane governs the rate of crystal-to-amorphous phase transformation and the thickness of the phase boundary. ⁶² Ostadhossein *et al.* ⁷⁸ also studied the Li insertion process into c-Si nano-wires using ReaxFF and revealed the atomistic

mechanism of the crystalline-to-amorphous phase transformation and demonstrated Li diffusion-induced compressive stress can slow down the lithiation process.

Although many experiments and computational studies have investigated the lithiation process of Si, the rate-limiting factor of this process has not yet been determined. In this work, I performed MD simulations with ReaxFF to examine lithiation dynamics in c-Si with different surface orientations and a-Si at the atomic-scale. Furthermore, I studied how to accelerate the lithiation rate by determining the rate-limiting factor in Li-Si system. We also investigated the effect of Li concentrations on Li diffusivity, which demonstrates the decisive role of Li concentration on the experimentally observed two-phase mechanism upon lithiation.

3.3 Simulation Methods

3.3.1 Reactive Force Field for Li-Si System

To perform molecular dynamics with reactive force field, reactive force field developed for Li-Si system was employed. The pioneer work in development of reactive force field for Li-Si system was performed by van Duin *et al.*, who developed the ReaxFF for Si and Si-Oxide systems.⁷³ In this work, parameters were trained against a set of DFT-calculated data for a wide variety of well-known condensed phases and clusters, including equation of states (total energy versus volume) of Si (sc, diamond, $\beta - \text{Sn}$), SiO₂ ($\alpha - \text{quartz}$, trydimite, coesite, $\alpha - \text{cristobalite}$, stishovite), dissociation energies of single and double bonds of Si-Si and Si-O in Si/O/H clusters, energies of various Si/O/H clusters as a function of valence angles Si-O-Si, O-Si-O, and Si-Si-Si and distortion energies of rings of Si/O/H clusters. Fan *et al.*, ⁵⁹ further optimized the parameters against a training set from DFT calculations which contained a collection of energies, geometries, and charges relevant to the Li-Si system including equation of states for the

body-centered cubic (bcc), face-centered cubic (fcc), and hexagonal-close-packed (hcp) phases of Li and crystalline LiSi, Li₁₂Si₇, Li₁₃Si₄, and Li₁₅Si₄, as shown in **Fig. 3-1**.

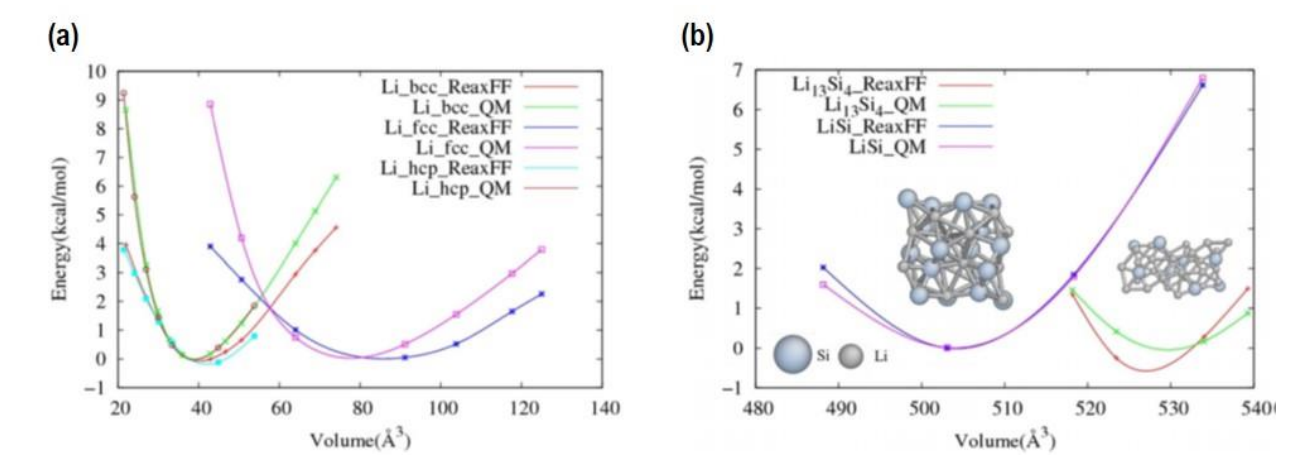


Figure 3-1 Energy versus volume of (a) Various Li crystals and (b) crystalline LiSi and Li₁₃Si₄ predicted by DFT and ReaxFF calculation (Adapted from reference [⁵⁹]. Copyright © Modelling and Simulation in Materials Science and Engineering 2013)

A total 10 parameters were fitted to a training set containing 142 data points using a successive single-parameter search method with multiple cycles to account for parameter correlation. The performance of ReaxFF for Li-Si was evaluated by open-cell voltage, volume expansion, and Young's modulus which agreed well with the experiment and DFT calculation results. Therefore, in this study, the ReaxFF developed for Li-Si system was employed to simulate the lithiaton process and determine the rate-limiting factor to accelerated lithiation rate and effect of Li concentration on Li diffusivity.

3.3.2 Molecular Dynamics Simulations

To study the lithiation dynamics, ReaxFF-based MD simulations implemented in the Large-scale Atomic/Molecular Massively Parallel Simulator (LAMMPS) were performed. It is well known that Si anodes undergo massive volume expansion and crystal-to-amorphous phase

transformation upon lithiation. Therefore, to obtain the optimized coordinates and lattice parameters, which incorporate the effect of volume expansion and phase transformation, density of a-LiSi structure at room temperature was first calculated and used as a reference to construct the simulation cell size. The c-LiSi was first melted at a high temperature (2500 K) and then quenched to room temperature using NPT ensemble while the ratio of Li and Si was kept constant. The obtained density of a-LiSi at 300 K was 1.91 g/cm³.

System	Simulation cell (Å)			# of	Time required to reach uniform concentration (ps)				
	X	y	Z	atoms	900K	1200K		1500K	
					Dense Si	Dense Si	Si with 5 % vacancies	Dense Si	Si with 5 % vacancies
a-Si	28.329	28.329	45.438	2400		800	720	520	460
c-Si (100)	26.881	26.881	57.700	2744	>1 ns	>1 ns	>1 ns	740	640
c-Si (110)	27.154	26.881	52.457	2520	>1 ns	>1 ns	>1 ns	660	580
c-Si (111)	26.605	26.881	57.108	2688	>1 ns	>1 ns	>1 ns	780	680

Table 3-1 Summary of time required to reach fully lithiated stage, together with simulation information of amorphous Si and crystalline Si with (100), (110), and (111) surface orientations

Once the targeted density for the simulation cell was determined, slab structures of a-Si and c-Si with surface orientations (100), (110), and (111) were prepared, and Li atoms were packed into the simulation cell as amorphous at both sides of the Si slab. Dimensions for simulation cells are listed in **Table 3-1**. 3D periodic boundary conditions were implemented to mimic an infinitely large Si slab sandwiched between two Li slabs, with two Li/Si interfaces included in each simulation cell. Therefore, the main lithiation direction is perpendicular to the Li/Si interfaces. In order to simulate the lithiation process, Li and Si atoms were initially completely separated and the negative heat of formation drove Li atoms to mix with c-Si and a-Si during the MD simulations. MD simulations of NVT ensemble with the Nosé-Hoover thermostat and the velocity verlet integration algorithm with a time step of 1.0 fs were applied to simulate the lithiation process,

especially the initial mixing process and the subsequent longtime random walk diffusion process. Within the NVT ensemble, the initial configurations were allowed to locally optimize their geometry by minimizing the energy for approximately 2000 MD time steps, corresponding to 2 ps. Then, lithiation dynamics simulations were performed for 1 ns in both a-Si and c-Si. MD simulations were performed at high temperatures (900 K \sim 1500 K) to accelerate the reactions, therefore reducing the simulation time. These temperatures are much lower than the melting temperature of Si, and thus will not change the reaction or diffusion mechanisms and allow us to study the chemical reactions on time scales relevant for MD simulations. 55,56,79,80

To determine the rate-limiting factor upon lithiation, 5 % random vacancies in Si and Li were created separately and lithiathion dynamics were compared. Furthermore, the lithiation dynamics was investigated in more detail for c-Si with 2 %, 4 %, 6 %, 8 %, and 10 % vacancies, in order to reveal the effect of vacancy concentration on lithiation rate.

In addition to slab models, bulk structures of a-Li_xSi with x ranging from $0.1 \sim 4.4$ were prepared using similar heating and quenching methods. NVT dynamics were performed at temperatures ranging from 900 K~1500 K and the diffusivities of Li and Si atoms during subsequent diffusion period were computed (the determination of the subsequent diffusion period will be discussed specifically for each case in **Section 3.4.4**).

3.3.3 Local Concentration and Diffusion Properties Analysis

In order to investigate the characteristic lithiation dynamics and track the evolution of Li concentrations, local concentrations of successive stages of lithiation were computed. The information regarding local concentrations was obtained by dividing the simulation cell length corresponding to the lithiation direction into 21 bins with equal size (~2 Å) and calculating the

ratio of Li and Si atoms corresponding to the specific bins. For Li_xSi, the Li concentration, y = 1/(1+x), was defined. The local y was tracked for each bin at different time steps to reveal the evolution of Li concentrations.

In typical MD simulations, mean squared displacement (MSD) is the most common measure of the average distance traveled by random motions in a time interval. Based on MSD, the diffusion coefficient at a given temperature was also calculated using the Einstein relation:

$$D = \lim_{\tau \to \infty} \frac{MSD(\tau)}{q_i \tau} = \lim_{\tau \to \infty} \frac{1}{q_i \tau} < |r_i(\tau + t_0) - r_i(t_0)|^2 >$$
 (3-1)

where $r_i(t)$ is the atomic positions at time t and q_i is a numerical constant that depends on dimensionality. In this work, q_i value is 6, which represents three-dimensional diffusion. During the initial mixing period, the motion of Li and Si are not random. So the MSD should only be calculated after the system evolves into subsequent diffusion period, where Li diffusion is characterized as "random" walking. Once the system reaches the subsequent diffusion period, the averaged MSD and diffusivity were calculated. Similar to local concentrations, local mean square displacements (LMSD) and diffusivities were also defined. The LMSD (τ) measures the average atomic diffusion distance during time interval of τ in each bin, as

LMSD
$$(\tau)_{Bin} = \frac{1}{N_{Bin}} \sum_{i}^{N_{Bin}} \langle |r_i(t_0 + \tau) - r_i(t_0)|^2 \rangle$$
 (3-2)

where N_{Bin} is the total number of atoms in the given bin. Since the atoms can move in and out of the bins, the final atomic positions at time $t_0 + \tau$ were used to assign atoms into different bins.

3.4 Results and Discussion

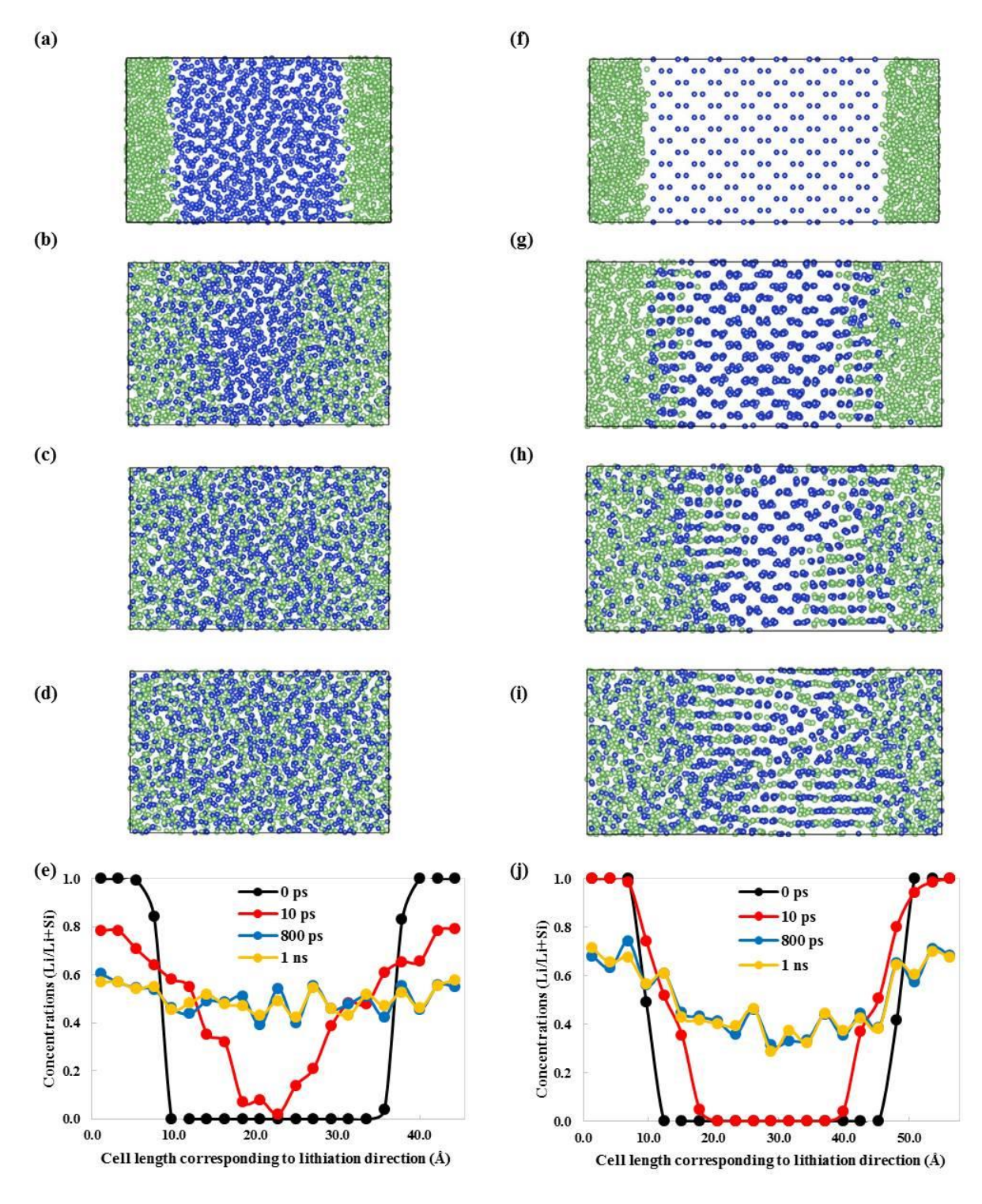


Figure 3-2 (a) \sim (e) Structural snapshots and local concentrations profile at successive stages of lithiation of a-Si and (f) \sim (j) c-Si with (100) surface orientation. All snapshots are taken at 1200 K. In the figure, spheres in blue and green color represent Si and Li atoms, respectively

3.4.1 How Lithiation Proceeds in a-Si

To track the lithiation dynamics of a-Si, a series of MD simulations at elevated temperatures (900 K, 1200 K, and 1500 K) were performed. Representative lithiation dynamics are illustrated in Fig. 3-2. The snapshots at 0 ps, 10 ps, 800 ps and 1 ns at 1200 K are shown in Fig. 3-2 (a) to (d). In order to accurately track the lithiation front, local concentrations for these four snapshots were compared in Fig. 3-2 (e). At time t = 0, a sharp interface separates the Li and a-Si slabs. The spontaneously lithiation process is driven by the negative heat of formation of Li_xSi . The mixing proceeds as Li atoms move into the Si slab and Si expands outward, resulting in increasing Li concentration in the center of the Si slab. At 10 ps, the center of the Si slab is still not lithiated (y = 0). The Li concentration in the Si slab increases as a function of time. At 800 ps, the concentration distribution in the a-Si is uniform, indicating it is completely mixed. Little change in local Li concentration is observed after 800 ps until 1 ns. By tracking the local concentration distribution, we determine the fully lithiation time as the time required to reach the uniform Li concentration through the simulation cells. At 1200 K, it requires 800 ps to fully lithiate the a-Si and it becomes faster at 1500 K, which only takes 520 ps. At 900 K, the structure did not reach its fully lithiated stage within our simulation time (>1 ns).

3.4.2 How Lithiation Proceeds in c-Si

Structural configurations during Li insertion into c-Si with (100) surface orientations at 1200 K are shown in **Fig. 3-2** (**f**) to (**j**). As shown in **Fig. 3-2** (**f**) and (**j**), lithiation into the initially c-Si is still in progress after 1 ns, whereas the initially a-Si is completely mixed after 800 ps. This clearly indicates that reaction is more active in a-Si, as expected due to the less ordered Si-Si covalent bonds, which result in easy dissociation upon lithiation.

We have observed the orientation dependent lithiation dynamics in c-Si, similarly to the anisotropic effect discussed in the literature. ^{16,43–45,81} It can be seen that lithiation behavior in c-Si is controlled by hopping diffusion of Li atoms between the tetrahedral sites, which has been proven to be the most stable position in c-Si upon Li insertion. ⁸² To verify whether ReaxFF successfully captures the preferential Li insertion into tetrahedral sites (T_d) in c-Si, we calculated the binding energies of Li atom in c-Si at four different potential Li atom insertion sites including tetrahedral, hexagonal, bond-center, and next nearest neighbor sites. Among all four sites, the tetrahedral site is the most stable position for Li atoms. It is 0.65 eV lower in energy compared to the hexagonal site (the second energetically favorable position), which is in good agreement with the value obtained from first-principles calculations (0.55 eV). ^{83,84} Furthermore, the calculated energy barrier for a Li atom to hop between two tetrahedral sites in the c-Si using ReaxFF is also in good agreement with that obtained from first principles calculations. ^{62,85} These results confirmed that ReaxFF can accurately capture the energetics of Li insertion and hopping diffusion in c-Si.

This lithiation pattern continues as Si gradually loses its crystalline structure and becomes amorphous. At 1 ns, although some local order can be observed in the structure, the overall radial distribution function shows a typical amorphous structure character. As lithiation proceeds, the Si-Si covalent bonds with all nearby tetrahedral sites occupied by Li atoms become weakened and eventually break. This phenomenon is due to both mechanical swelling and the charge transfer from Li to Si. The charge transferred to Si fills up the antibonding sp³ state of Si, subsequently weakens, and eventually breaks the corresponding Si-Si covalent bonds. Si Similar lithiation mechanism (Li occupying the first available tetrahedral sites) occurs in c-Si (111), however the location of first available tetrahedral sites are normal to the lithiation direction, thus creating a layer of Li atoms near the Li/Si interface. Accumulation of Li atoms results in a high local

concentration of Li atoms between the adjacent (111) planes, which causes breakage of Si-Si covalent bonds between the (111) bilayers. This results in a ledge mechanism, which is characterized by the peeling off of (111) planes. The layer-by-layer cleavage of (111) planes upon lithiation clearly explains the atomic mechanism of crystalline-to-amorphous phase transformation, which supports the *in situ* TEM observation.⁴³ The amount of time required for each structure to become fully lithiated is summarized in **Table 3-1**. For all of the cases, lithiation in a-Si proceeds faster than in c-Si. Among c-Si orientations, c-Si with surface orientation (110) reaches the fully lithiated stage the fastest due to fast Li ion diffusion channel along <110> direction, consistent with experiments. ⁴⁵

3.4.3 Si Vacancy Generation Accelerates Lithiation Dynamics

More importantly, the unanswered questions are what the rate-limiting factor is during the lithiation of the Si anode and how to accelerate the lithiation process.

As shown in **Fig. 3-3** (a) - (c), the lithiation rate is accelerated when vacancies are introduced in Si, whereas vacancies in Li have negligible impact on the lithiation dynamics. **Fig. 3-3** (d) represents the location of the reaction fronts of systems with no vacancies, 5 % Li vacancies, and 5 % Si vacancies after 10 ps at 1200 K. The location of the reaction front is marked by the furthest Si bins with non-zero Li concentration. As clearly indicated in the plot, the location of the reaction front is further into the Si slab when Si vacancies are introduced, which indicates the lithiation rate is dramatically increased by Si vacancies. In comparison, the presence of vacancies in Li does not change the lithiation rate at all.

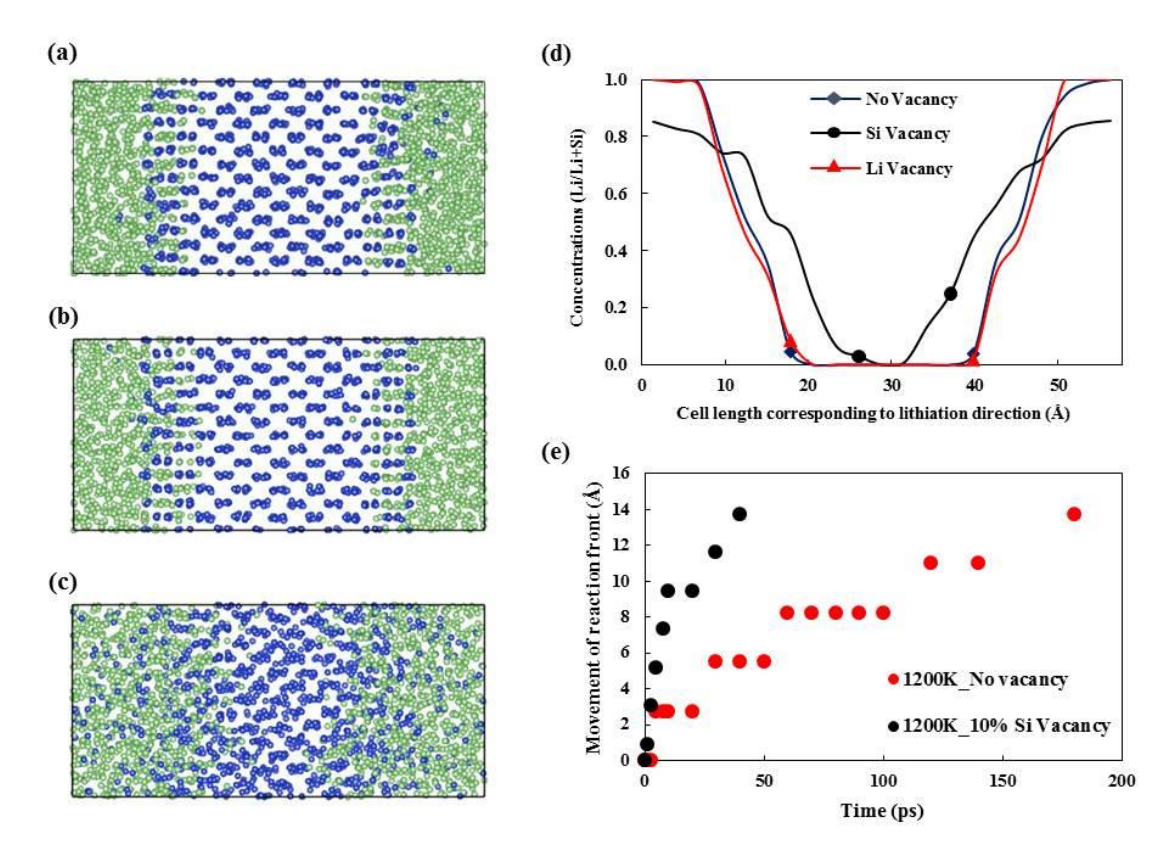


Figure 3-3 Structural snapshots of c-Si with (100) surface orientations with (a) no vacancy, (b) 5 % Li vacancy, (c) and 5 % Si vacancy after a reaction time of 10 ps at 1200 K. In the figure, spheres in blue and green color represent Si and Li atoms, respectively (d) The concentration profiles of the three snapshots. (e) Movement of reaction fronts with and without Si vacancies with respect to time at 1200 K

To further illustrate the effect of vacancies on lithiation dynamics, the locations of lithiation reaction fronts with and without Si vacancies were tracked as a function of time, as shown in **Fig. 3-3** (e). The lithiation rate is four times faster with 5 % Si vacancies. Additionally, a clear linear trend is observed in both cases indicating that short-range processes at the reaction front control the lithiation dynamics, agreeing well with *in situ* TEM experiments in both c-Si and a-Si. ^{44,47}

Even though our previous calculations suggested that Si atoms remain relatively stationary during lithiation,⁵⁶ the empty space generated by Si vacancies facilitates local rearrangement of Si atoms to readily accept Li insertion. Furthermore, our results indicate that the movement of Si

atoms is the control-factor of the lithiation process in Si electrodes and suggest that the lithiation rate can be enhanced by introducing vacancies in Si. Huang and co-workers performed first principle calculations to highlight the role of vacancies at the beginning of the lithiation process of c-Si. By calculating the binding energy, they concluded that vacancies can enhance Li binding energy significantly and make the initial Li insertion process thermodynamically more favorable. The vacancy-assisted diffusion of Li during the initial stage of lithiation provides the thermodynamic proof for the effect of vacancies, which is consistent with our MD simulation results. In addition, the MD results also show more dynamics information. We also calculated the time required to fully lithiate c-Si structures with 5 % Si vacancies, shown in **Table 3-1**. As expected, the lithiation rate becomes faster in all cases compared to the structures without vacancies. The anisotropic effect also becomes less pronounced as the vacancies disrupt the ordered crystalline network.

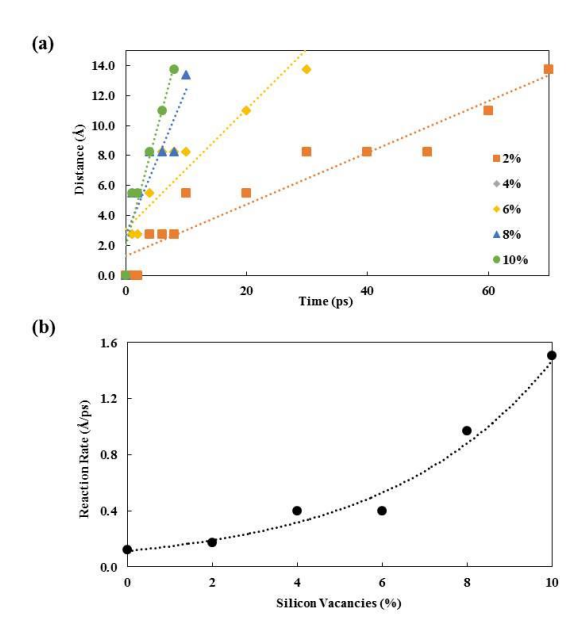


Figure 3-4 (a) Movement of reaction fronts with 2 %, 4 %, 6 %, 8 %, and 10 % Si vacancies with respect to time (b) Reaction rates with corresponding Si vacancy concentrations. All information was obtained during lithiation of c-Si with (100) orientation at corresponding Si vacancy concentration at 1500K

To elucidate the impact of Si vacancy concentration on the lithiation rate, we performed MD simulations of c-Si with 2 %, 4 %, 6 %, 8 %, and 10 % vacancies at 1500 K. The movement of the reaction front and the radial distribution functions $g_{Si-Si}(r)$ were analyzed to characterize the effect of Si vacancy concentration on lithiation dynamics. **Fig. 3-4** (a) demonstrates the movement of the reaction front as a function of time at different Si vacancy concentrations. As clearly indicated in the plot, the movement of the reaction front is faster with higher vacancy concentrations. With a linear fitting to describe the reaction front controlled lithiation dynamics, ^{44,47} the lithiation rate, k, was obtained for each different vacancy concentration. **Fig. 3-4** (b) shows that the lithiation rate exhibits an exponential relationship with respect to the vacancy concentration. This relationship can be explained by assuming the activation energy for the lithiation reaction, E_a , is proportional to the energy required to break Si-Si covalent bonds due to vacancy generation, as:

$$k \propto \exp\left(\frac{-E_a}{k_B T}\right) = \exp\left(\frac{-(1-c_v)\cdot 4\cdot N_{Si}\cdot E_f}{k_B T}\right) \propto \exp\left(\frac{c_v E_f}{k_B T}\right) \tag{3-3}$$

where c_v is the vacancy concentration, N_{Si} is the number of Si atoms, E_f is the vacancy formation energy, k_B is the Boltzmann constant, and T is the temperature. According to **Eqn. 3-3**, higher Si vacancy concentrations will result in faster reaction rates with an exponential relationship, which supports our data regarding the movement of the reaction front and further confirms that the bond breaking of Si is the rate-limiting factor during the lithiation.

To characterize the effect of Si vacancy concentrations on the crystal-to-amorphous phase transformation upon lithiation, structural evolutions during lithiation were investigated by comparing the $g_{Si-Si}(r)$ of the snapshots at 1 ps and 1 ns for systems with 2 % and 8 % Si vacancies

in **Fig. 3-5**. The initially sharp peak associated with the second nearest neighbors in $g_{Si-Si}(r)$ diminishes and becomes broader with time, demonstrating an amorphization process.

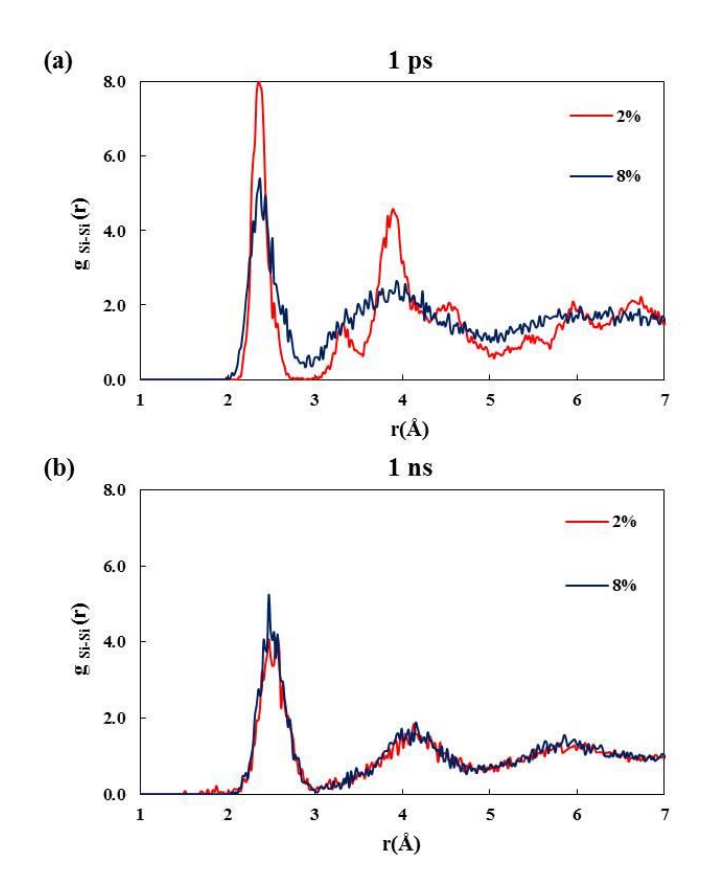


Figure 3-5 Radial distribution functions $g_{Si-Si}(r)$ at 1500K for c-Si with (100) orientation with 2 % and 8 % Si vacancies at (a) 1 ps and (b) 1 ns

The difference of peak intensities between c-Si structures with 2 % and 8 % Si vacancies at 1 ps clearly indicates that the crystal-to-amorphous phase transformation occurs much faster with more Si vacancies. After 1 ns, the second nearest neighbor peak disappears and remaining peaks become broader for both cases, suggesting a complete transformation from c-Si to a-LiSi.

To take advantage of vacancy accelerated lithiation dynamics, vacancies can be introduced into crystalline or amorphous Si experimentally via irradiation, chemical vapor deposition, and ion bombardment. ^{87–90} Previous experimental results and theoretical analysis also suggested the

vacancies and amorphization in Si induced by ion bombardment will lead to the formation of voids after high temperature annealing. Amorphous Si with 10 % vacancies can transform into porous Si or relax to Si with less excess volume. Thus, there must be a limit on the concentration of vacancies which can exist in a Si anode that experiences electrochemical lithiation and delithiation cycles, warranting further research.

3.4.4 Random Diffusion of Li in Si is Concentration Dependent

Experimental observations showed that lithiation dynamics depend on various factors; both two-phase formation during lithiation and asymmetric Li diffusion rates suggest that it is possible that Li diffusivity is higher in Li-rich phase and lower in Li-deficient phases. ^{46,93} To further quantify the dependency of the Li diffusivity on Li concentrations, we computed the Li diffusivity at different Li concentrations by first defining the period where Li diffusion was characterized by "random" walking.

3.4.4. (a) Local Concentration Evolution

In this study, the lithiation process in both a-Si and c-Si can be characterized as two stages: an initial mixing period, followed by a subsequent diffusion period. The initial mixing period is the time period when the covalent Si-Si bonding network breaking and Si volume swelling govern the lithiation dynamics. We defined the time of the initial mixing period to be from the beginning of the simulation until the local concentration become steady with a uniform concentration of 0.5. This time is summarized in **Table 3-1**. The initial mixing period is followed by a subsequent diffusion period, which is characterized by Li randomly diffusing in the a-Li_xSi formed with a uniform Li concentration. We defined the subsequent diffusion period to be from the time when

the local concentration at different positions became uniform (end of the initial mixing period) until the end of our simulation time (~ 1 ns).

The long time required to lithiate c-Si allowed us to analyze the local concentration evolution during lithiation in more details. We investigated the concentration distribution with respect to the time and position during lithiation of c-Si with (100) surface orientations at 1200 K and 1500 K as shown in **Fig. 3-6**.

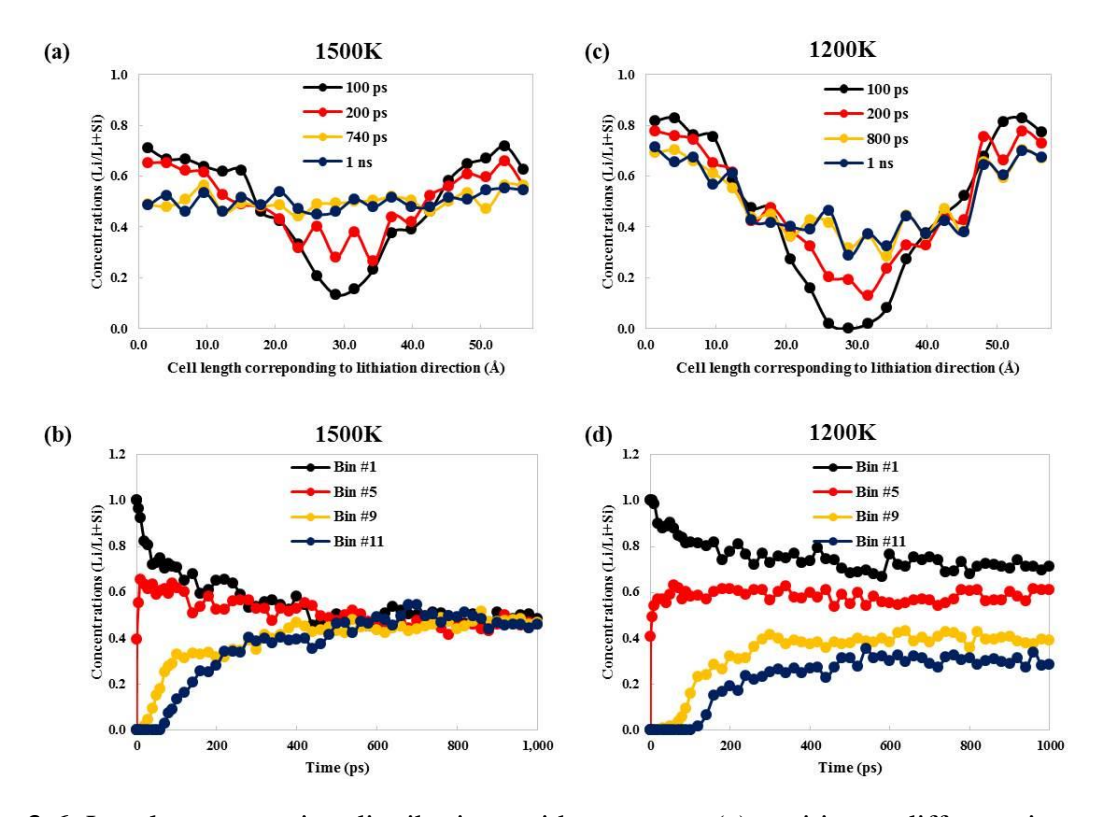


Figure 3-6 Local concentration distributions with respect to (a) position at different time and (b) time at different positions at 1500 K. Concentration distributions respect to (c) position at different time and (d) time at different positions at 1200 K. All concentration profile was obtained during lithiation of c-Si with (100) orientation at corresponding temperature

Fig. 3-6 (a) shows the concentration distribution at different simulation times at 1500 K. A uniform Li distribution has been reached after 740 ps. **Fig. 3-6 (b)** shows the concentration evolution in several representative locations. Bin #1 is located in the initial Li region, bin #5 is

located at the initial Li/Si interface region, bin #9 is in the Si region close to the Li/Si interface, and bin #11 is located at the center of Si slab, which should be lithiated the last. As lithiation proceeds, the Li concentration decreases in bin #1 and #5, while bin #9 starts to be lithiated after 25 ps and bin #11 starts to be lithiated after 70 ps. Concentrations in all bins evolved toward 0.5, a1:1 ratio of Li and Si atoms, and reached 0.5 at 740 ps. After 740 ps, the concentration change in each bin becomes negligible, confirming a uniform concentration of 0.5. This process occurs similarly at 1200 K, reaching a concentration of 0.5 at 800 ps, as shown in Fig. 3-6 (c) and (d). However, the lithiation at 1200 K shows that a slight concentration gradient concentration gradient still exists after 800 ps and becomes steady within our simulation time (~1 ns). This non-uniform Li concentration may indicates that lithiation is still in progress at 1200 K after 1 ns. Theoretically, a longer simulation time will result in a uniform concentration of 0.5 at all positions. In our case, such complete mixing did not occur within 1 ns. Hwang et al. 78 observed a stress effect on the reaction front, more specifically, compression slows down the lithiation and eventually becomes stagnated. However, since our system becomes completely lithiated at 1500 K, it is more likely due to a combination of temperature and simulation time effects rather than the stress effect.

Since Li diffusion in the initial mixing period deviates from random diffusion, it is unreasonable to compute the diffusion coefficient from averaged MSD calculations. However, we noticed that in **Fig. 3-6 (c)** and **(d)**, the local concentrations during lithiation of c-Si with surface orientation (100) stopped changing after 800 ps. Locally, the structures have become amorphous with a uniform concentration from 800 ps to 1 ns. This time range with constant concentrations may be reliable for diffusivity calculations, since random walking governs the diffusion during this time interval. Therefore, we computed the LMSD values at different bins using **Eqn. 3-2** and calculated local diffusivities of Li using the Einstein relation in **Eqn. 3-1**. The red dots in **Fig. 3-7**

(a) represent the Li diffusivities at different concentrations obtained from LMSD calculations. As local Li concentration increases, local Li diffusivity also increases.

3.4.4. (b) Random Diffusion of Li in Si is Concentration-Dependent

In order to obtain a concrete trend between the concentration and diffusion coefficient over possible Li_xSi structures, we also constructed various bulk structures of a-Li_xSi with x ranging from 0.1 to 4.4 and performed NVT dynamics at high temperatures ranging from 900 K to 1500 K. Once the concentration became uniformly distributed, the averaged MSD calculations were performed to calculate the diffusion coefficient at corresponding concentrations, according to **Eqn. 3-1**.

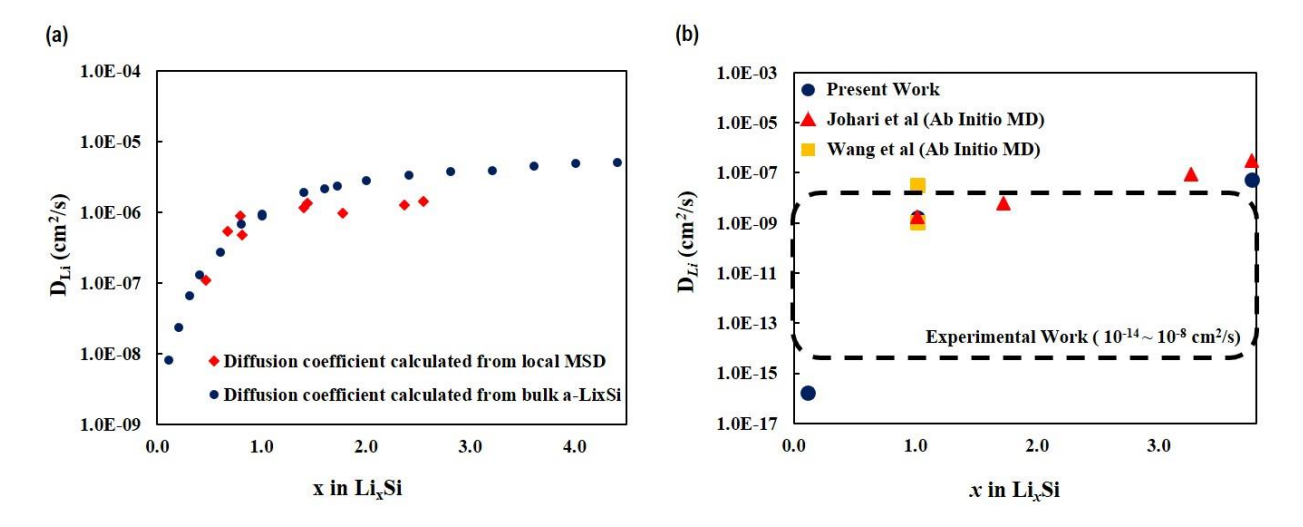


Figure 3-7 (a) Diffusion coefficients of Li at different concentrations in logarithmic scale at 1200 K. Diffusion coefficients with corresponding concentration upon lithiation from bulk a-Li_xSi is represented by blue dots. Red dots represent data obtained from local MSD calculations from initially c-Si with (100) surface orientation (b) Comparison Li diffusivity at with first-principle calculation and experiment

Diffusion coefficients computed at 1200 K at each corresponding concentration from bulk a-Li_xSi are represented by the blue dots in **Fig. 3-7** (a). The overall trend clearly indicates that an increase in concentration results in the increase in Li diffusivity. The local diffusivity data points

slightly deviate from bulk calculations due to the lack of statistics from our previous LMSD calculations. Interestingly, the relationship between the concentration and diffusion coefficient can be characterized by two distinctive regions, in which dramatic increase in Li diffusivity occurs below Li concentration of 0.8; and the increase becomes slower above Li concentration of 0.8. The overall trend indicates that increasing Li concentration results in faster Li diffusion, which is opposite from the intercalation type electrodes. 94,95 This phenomenon is likely due to the fact that semiconductor Si starts to show metallic behavior after the Li/Si ratio becomes larger than 1 (LiSi). The concept of concentration dependent Li diffusion in Si was recently revealed by AIMD calculations by Wang and co-workers. Even though their results have captured the increase of D_{Li} with Li content, the information was limited since the values of D_{Li} in Li_xSi were only calculated at x=1.0, 1.71, 3.25 and 3.75. Their results showed a linear trend between D_{Li} and these Li concentrations, x. With larger system sizes, longer simulation time, and a much broader concentration range of a-Li_xSi (0.1 < x < 4.4), our work shows a nonlinear relationship and provides a more complete picture regarding concentration dependent Li diffusion in Si.

The relationship of a faster Li diffusion with increasing Li concentration can be is the underlying reason for experimentally observed two-phase lithiation in both c-Si and a-Si. *In situ* TEM studies have revealed that during lithiation an atomically sharp (~1 nm) phase boundary forms, which abruptly separates the Li-rich region and Li-poor region. ⁴³ To mimic this two-phase phenomenon, finite element models with concentration dependent diffusion coefficient have to be implemented. ^{46,96} However, the origin of this relationship is still missing. Our simulation results predict a lower diffusivity in Li-poor regions and explain the origin of the two-phase lithiation. This relationship may also be the underlying reason for lithiation/delithiation hysteresis. During battery cycling, the cut-off voltage is only determined by the surface concentration, while a

concertation gradient can still exist inside the electrode particle. During the lithiation stage, the initial diffusivity at low concentrations is significantly slower whereas the initial diffusivity of Li during the delithiation stage is faster. This difference will result in two different concentration profiles (during lithiation and delithiation) at the same surface concentrations, leading to different charge and discharge capacities at the same voltage.

3.4.4. (c) Room-Temperature Li and Si Diffusivity Calculation

We have computed the diffusivity for three Li_xSi concentrations, where x=0.1, 1, and 4.4 at temperatures from 900 K to 1500 K. From the diffusivities calculated at different temperatures for a-Li_xSi, we extrapolated the diffusivities at room temperature at corresponding concentrations. The extrapolation is done by applying the Arrhenius expression for diffusivity as described in **Eqn.** 3-4:

$$D = D_0 \exp\left(\frac{-E_a}{k_B T}\right) \tag{3-4}$$

where E_a is the activation energy, k_B is the boltzmann constant, and T is the temperature. Li diffusivity at room temperature and at x values of 0.1, 1, and 4.4 are 2.002×10^{-16} , 1.965×10^{-9} , and 6.428×10^{-8} cm²/s, respectively, as shown in **Fig. 3-7** (b). Our results agree well with the result from AIMD calculations which provided the Li diffusivity at room temperature with x=1 to be ranging from $10^{-10} \sim 10^{-8}$ cm²/s.^{56,58,97} Within the Li content range of x=1.00 to 3.75, the calculated D_{Li} values using AIMD were in the range of 2.08×10^{-9} to 2.37×10^{-7} cm^2 /s at 298K so the ReaxFF MD results and AIMD results are in good agreement.⁵⁸ Si diffusivity for the x values of 0.1, 1, and 4.4 are 2.270×10^{-20} , 1.277×10^{-11} , and 6.428×10^{-10} cm²/s, respectively. The experimental results for the diffusivity of Li in Si suggests the value of D_{Li} to be from $10^{-14} \sim 10^{-8}$

cm²/s, ^{79,93,98} which agrees well with ReaxFF calculated values. Our result reveals that Si is almost immobile thus, the movement of Si atoms could significantly affect the lithiation rate.

3.5 Conclusions

In summary, we have performed ReaxFF-based MD simulations to study the diffusion dynamics of both c-Si and a-Si. We discovered the lithiaton dynamics can be characterized as two stages; initial mixing period followed by subsequent random walk diffusion period. During the initial mixing period where crystalline-to-amorphous phase transformation occurs, Li diffuses faster in a-Si than in c-Si. During this period, Li diffusion in c-Si is governed by hopping diffusion between energetically favorable tetrahedral sites. The lithiation proceeds by layer-by-layer peeling off of (111) planes, which illustrates the location of (111) plane plays a critical role in lithiationinduced amorphization process. On evaluating the rate-limiting factor during Li mixing with Si, we found that introduction of Si vacancies resulted in accelerated lithiation rate whereas Li vacancies have negligible impact. The lithiation rate increases exponentially with the Si vacancy concentration, suggesting that Si-Si bond breaking is the rate-limiting factor, which is lowered by Si vacancies. Our results also revealed that Li diffusivity increases with concentration, which highlights the concentration dependent diffusion. This result provides the basis for the experimentally observed two-phase lithiation mechanism and is the underlying reason for lithiation/delithiation hysteresis. During the lithiation stage, the initial diffusivity of Li at low concentration is significantly slower than the initial diffusivity of Li during delithiation stage (high Li concentration). Since the lithiation/delithiaiton capacity is directly related to the diffusivity and its dependence on Li concentration, the characteristic concentration dependent diffusion could significantly contribute to the lithiation/delithiation hysteresis. These findings provide important insight into understanding the dynamics upon lithiation in Si anodes, which could be utilized to design optimized batteries.

Chapter 4 Atomistic Simulation Derived Insight on the Irreversible Structural Changes of Si Electrode during Fast and Slow Delithiation

4.1 Summary

Quantifying the irreversible chemical and structural changes of Si during cycling remains challenging. In this study, a continuous reactive molecular dynamics delithiation algorithm, with well-controlled potential gradient and delithiation rate, was developed and used to investigate the "natural" delithiation responses of an aluminum-oxide coated silicon thin-film. Fast delithiation led to the formation of dense Si network near the surface and nanoporosity inside the a-Li_xSi, resulting in 141 % volume dilation and significant amount of Li trapped inside (a-Li_{1.2}Si) at the end of delithiation process. In contrast, slow delithiation allowed the a-Li_xSi to shrink by nearequilibrium condition, demonstrating no permanent inner pore with nearly Li-free structure (a-Li_{0.2}Si) and minimal volume dilation (44 %). However, even without trapped Li, the delithiated a-Li_xSi still exhibited higher volume (lower density) than the equilibrium structure with the same Li concentration, despite delithiation rate. The origin of this excess volume is the loss of directly bonded Si-Si pairs, which made the subsequent relithiation faster. Based on the atomistic modeling and the quantified degradation mechanism, battery operating guidelines, including the delithiation rate and the depth of charge to avoid trapped Li and coating delamination, were suggested to improve the durability Si electrodes.

This chapter is reproduced from the work published as: Kwang Jin Kim, James Wortman, Sung-Yup Kim, and Yue Qi, "Atomistic Simulation Derived Insight on the Irreversible Structural Changes of Si Electrode during Fast and Slow Delithiation," Nano Letters 2017, 17 (7), pp 4330 – 4338.

4.2 Introduction

Delithiation is not a reverse process of lithiation. Regardless of the initial phase of Si being lithiated is crystalline or amorphous, fully lithiated silicide (crystalline or amorphous Li₁₅Si₄) became amorphous upon delithiation. 33,35,36,38,99,100 It is obvious that the initial crystalline Si (c-Si) rarely went back to crystal after delithiation. 33,36,38,99 However, whether an amorphous Si (a-Si) structure returns to its original structure after lithiation and delithiation cycles remains unclear. Using in situ TEM, McDowell et al.46 observed a clear phase boundary (indicating a two-phase lithiation process) during the first lithiation cycle of a-Si nanospheres, but no phase boundary during the second lithiation cycle. This indicates that the initial amorphous structure might be different from those after cycling. Most experimental techniques, including X-ray diffraction, transmission electron microscopy (TEM), and nuclear magnetic resonance (NMR), are not sufficiently sensitive to reveal the amorphous characteristics. Therefore, this paper used atomistic simulations with a newly developed delithiation algorithm, to illustrate the detailed structural differences after delithiation and the effect of these structural changes on the subsequent lithiation process. It quantifies, for the first time, the irreversible volume change, amount of trapped Li, generation and distribution of pores, and atomistic structural difference in the amorphous structures, upon delithiation.

The irreversible volume change of Si nano-structures after cycling can be directly measured. Although nano-structures successfully mitigated fracture and pulverization of Si electrodes, ^{10,41} they still do not return to their original volume after cycling. ^{46,101,102} For example, using *in situ* TEM, Ghassemi *et al.* ¹⁰¹ reported the diameter of the delithiated a-Si nanorods was 5 % larger compared to the initial diameter; and McDowell *et al.* ⁴⁶ observed a 25 % volume dilation of delithiated a-Si nanospheres. The irreversible volume restoration becomes more interesting

when multiple lithiation/delithiation cycles are considered. Sun *et al.*¹⁰² tracked the volume variations of Si-beaded-string structure for 18 cycles. In the first few cycles, the volume of the dilated Si-beads was 70 % larger than the original volume. Interestingly, the degree of dilation dramatically decreased to 10 % as more cycles were repeated.

Two mechanisms, the formation of pores and voids inside the Si^{103–105} and the residual Li trapped in Si, can both contribute to the overall irreversible volume dilation after cycling. Choi et al. 104 demonstrated that Si nanowires became porous and the pore size increased with subsequent cycles. DeCaluwe et al. 105 observed the formation of nano-pores upon delithiation and further proposed a pore collapse and regrowth mechanism upon multiple cycles. However, the volume of these pores/voids is difficult to quantify experimentally. The contribution from the trapped Li atoms to the volume dilation is even more difficult to quantify. It was proposed that trapped Li atoms may be impossible to extract, since nano-structured Si electrode has higher density of defect sites, such as dangling bonds, which can bond Li more strongly. 106-109 Recently, Key and coworkers³⁵ confirmed the existence of trapped Li atoms after complete delithiation of Si electrode by analyzing the local structural changes with NMR, although the amount of Li is not yet determined. Besides contributing to the dilated volume, the trapped Li atoms are particularly interesting, as they directly lead to capacity loss. Furthermore, they may also significantly affect the final structure after delithiation and impact the subsequent lithiation process. Although the volume change induced solid electrolyte interphase (SEI) growth on Si electrode surface is also one of the main contributors to the irreversible capacity loss, ^{24–26,44,45,110} it is out of the scope of the current study. This paper mainly focuses on the irreversible structural change of Si and reveal the detailed mechanical degradation mechanism.

Atomistic simulations in conjunction with experiments have played an important role in revealing the lithiation mechanism^{24,32,33,34,37,38,41,43,58,63,66,95,96} but not the delithiation mechanism. It is relatively straightforward to simulate the lithiation process since simply putting Li and Si in contact will drive a spontaneous lithiation process due to the negative heat of mixing. However, it is challenging to accurately simulate the delithiation process since an external driving force is required to remove the Li from the lithiated silicon. M.K.Y. Chan et al. 51 developed a historydependent Li insertion and removal algorithm based on energy minimization using density functional theory (DFT), which limits the simulation size, so the long-range structural evolution and the information regarding volume contraction are difficult to obtain. Compared to DFT calculations, MD simulation with accurate interatomic potential, such as reactive force field (ReaxFF), can simultaneously track the chemical, structural, and mechanical evolution for larger system size and longer time. Regarding delithiation simulation, Jung et al. 63 simulated the delithiation process by removing the Li atoms from the surface of a-Li_xSi to generate a Li concentration gradient, which served as the driving force for delithiation. They revealed the formation of c-Si nuclei in the delithiated a-Li_xSi matrix and demonstrated that the volume of delithiated a-Li_xSi is larger than the original Si volume. However, removing all the Li from the surface abruptly disrupted the surface structure and may prevent a "natural" delithiation response in terms of volume contraction, structural evolution, Li diffusion in the Li-Si system.

To mimic a "natural" delithiation response, a continuous delithiation algorithm based on ReaxFF-MD simulations was developed. The continuous delithiation algorithm also captures the effect of different delithiation rate, which plays an important role in the irreversible structural change of delithiated Si. A lithiated a-Al₂O₃ coating layer on Si was utilized as a reservoir to generate a driving force for Li to naturally diffuse out of the Li_xSi. It is well known that a-Al₂O₃

is a promising coating material with high thermal stability, high dielectric constant, and excellent ability to withstand the volume expansion. Recently, the ReaxFF parameters for Li-Si-O-Al system were developed and used to simulate the lithiation process of coated-Si-nano-structures. The mechanical failure of the coating during delithiation is also critical to Si electrode. With this new systematic delithiation algorithm, the fundamental reasons of degradation was investigated, by analyzing the relationship between the depth of discharge and corresponding volume and structural changes at different rates. Furthermore, the effect of irreversible structural changes on subsequent lithiation processes was investigated. The Li trapping mechanism was also analyzed, which highlighted the important role of delithiation rates on irreversible capacity loss.

4.3 Simulation Methods

4.3.1 Reactive Force Field for Li-Si-Al-O-H System

To perform delithiation simulation of fully lithiated a-Li_{3.75}Si coated with aluminum oxide layer, we employed the reactive force field developed for Li-Si-Al-O-H system developed by Narayanan and co-workers.⁷⁴ Similar to the method Fan *et al.*,⁵⁹ implemented to develop force field for Li-Si system, Narayanan *et al.*, trained the parameters with DFT-calculated data for a wide variety of well-known condensed phases and clusters, as listed below (description and references within Narayanan *et al.*⁷⁴)

- 1) Equations of state for pure Al (fcc, hcp, bcc, sc, and diamond) and for corundum ($\alpha \text{Al}_2\text{O}_3$), surface energy of the fcc Al (111), charge distribution and dissociation energies of a number of Al-O-H clusters
- 2) Equations of state of Li (bcc, fcc, hcp, diamond, sc), LiH with sodium-chloride structure, dissociation energies and charge distributions in Li₂, LiH and LiH₂ clusters
- 3) Equations of state of Si (sc, diamond, β -Sn), SiO₂ (α -quartz, trydimite, coesite, α -cristobalite, stishovite), dissociation energies of single and double bonds of Si-Si and Si-O

in Si/O/H clusters, energies of various Si/O/H clusters as a function of valence angles Si-O-Si, O-Si-O, and Si-Si-Si and distortion energies of rings of Si/O/H clusters

- 4) Equations of state of Li-silicates: (a) Li₂SiO₃ (orthorhombic), (b) stable Li₂Si₂O₅ (monoclinic) and (c) metastable Li₂Si₃O₅ (orthorhombic)
- 5) Li oxides: α-Li₂O (cubic) and Li₂O₃ (hexagonal)
- 6) Li aluminates: three polymorphs of LiAlO₂ namely (a) α (rhombohedral), (b) β (orthorhombic) and (c) γ (tetragonal)
- 7) Al silicates: three polymorphs of Al₂SiO₅ namely (a) and alusite (orthorhombic), (b) sillimanite (orthorhombic) and (c) kyanite (triclinic)

For all the phases listed above $(1) \sim (7)$, heats of formation as function of volume was calculated by the equation;

$$\Delta H_f(V,\varepsilon) = E_{Li_k A l_l S i_m O_n}(V,\varepsilon) - k E_{Li} - l E_{Al} - m E_{Si} - \frac{n}{2} E_{O_2}$$

$$\tag{4-1}$$

where $E_{Li_kAl_lSi_mO_n}$ is the total energy of a given volume V of the phase Li_kAl_lSi_mO_n subjected to particular strain ε . The energies of the constituent elements Li, Al, Si, and O (E_{Li}, E_{Al}, E_{Si}, E_{O2}) are those of the most stable phases at equilibrium calculated by DFT. All the parameters were trained against the heat of formation and was confirmed that structural properties and heats of formation for selected condensed phases agree well within the results of DFT calculations and with experimental results. Therefore, we employed the reactive force field developed for Li-Al-Si-O-H system to investigation the irreversible structural evolution upon delithiation of a-Li_xSi with different rates.

4.3.2 Molecular Dynamics Simulations of the Delithiation Process

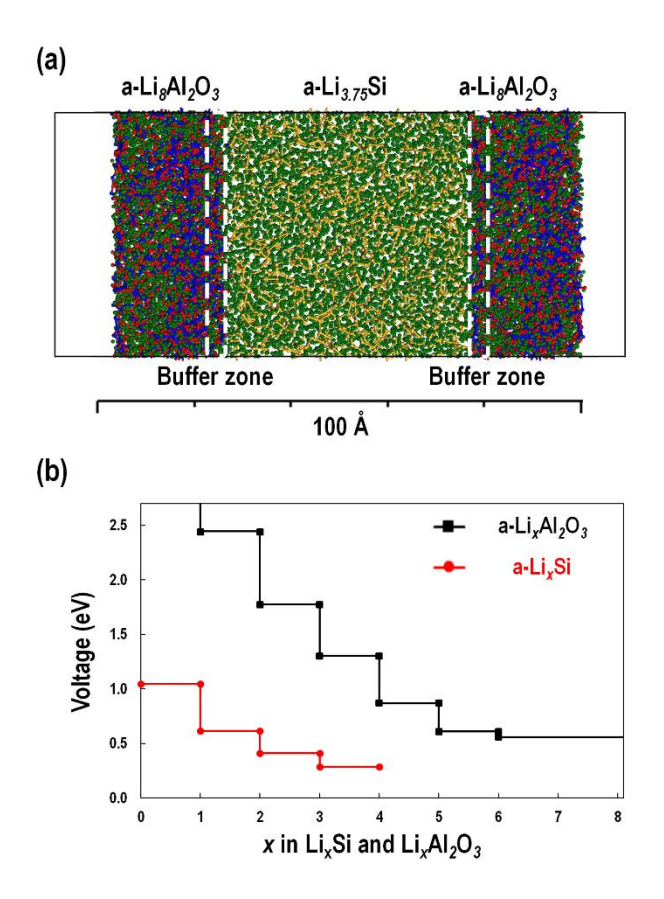


Figure 4-1 Model setup. (a) Initial structure of fully lithiated a-Li_{3.75}Si thin film sandwiched between fully lithiated aluminum oxide a-Li₈Al₂O₃ coatings, where spheres in yellow, green, red, and blue represent Si, Li, O, and Al atoms respectively (b) The computed open circuit voltage for a-Li_xSi and a-Li_xAl₂O₃. Continuously removing Li from the coating layer outside of the buffer zone (white region) will generate the chemical potential driving force for the Li inside Si thin film to "*naturally*" diffuse out

To study the volume variation, chemical reactions, and structural changes of a coated a-Li_xSi thin film upon delithiation, a continuous delithiation algorithm was developed. All ReaxFF-based MD simulations were performed with the Large-scale Atomic/Molecular Massively Parallel Simulator (LAMMPS). First, a slab structure of a-Li_{3.75}Si was prepared by melting (2500 K) and quenching (298 K) the c-Li_{3.75}Si using NPT ensemble. Similarly, fully lithiated a-Al₂O₃ (a-Li₈Al₂O₃) coating layers were obtained and attached to the both sides of a-Li_{3.75}Si, mimicking a

coated Si-thin film as seen in **Fig. 4-1 (a)**. The obtained density of a-Li_{3.75}Si and a-Li₈Al₂O₃ at 298 K is 1.12 g/cm³ and 1.68 g/cm³, respectively. Both values are in good agreement with experiments. The fully lithiated a-Al₂O₃ (a-Li₈Al₂O₃) coating layer was utilized as a Li reservoir source, where Li atoms were continuously removed to drive delithiation normal to the Si thin film direction. More specifically, a buffer zone was defined as the region occupied by 10 % Al atoms in the coating layer near the interface. Only the Li atoms outside the buffer zone were randomly removed. Confining the Li removal region to be outside of the buffer zone allows the "natural" delithiation responses, including atomic rearrangement and coating delamination, to be successfully captured without interrupting the a-Li_xSi surface or the Li_xSi/coating interface.

At equilibrium, the chemical potential of Li should be the same in the coating and Si phases. This can be illustrated by the computed open circuit voltage (OCV) curve in **Fig. 4-1 (b)**, which is also the Li chemical potential change as a function of Li concentration. Decreasing Li concentration in the a-Li_xAl₂O₃ coating layer will decrease the Li chemical potential, causing a higher OCV in a-Li_xAl₂O₃ coating than a-Li_xSi film. This Li chemical potential gradient will naturally drive Li atoms to diffuse out of a-Li_xSi film in order to reach equilibrium. Based on this concept, a step-by-step delithiation algorithm was developed. At each delithiation step, a fixed number of Li atoms, $\Delta N = 100$ in this work, was randomly removed from the lithiated coating layer outside of the buffer zone. Then, the structure was subject to NVT MD simulations for relaxation (with the Nose-Hoover thermostat and the velocity Verlet integration algorithm at a time step of 0.1 fs) at 900 K. 900K is about 50% of the melting temperature of Si (1687 K). Both experiments⁸⁰ and molecular dynamics simulations^{56,58,62,78,112} (based on DFT or ReaxFF) have obtained diffusivity for Li-Si system at high temperature ranging from 600 K ~ 1500 K then extrapolated the room temperature diffusivity using Arrhenius equation. The extrapolated room

temperature Li diffusivity from the ReaxFF-MD simulation agreed well with experimental results, 79,98 which confirmed the usage of 900K in this study only accelerates the diffusion, thus reducing the simulation time without changing the diffusion mechanism. The relaxation time (Δt) will allow the Li inside the a-Li_xSi film to diffuse to the a-Li_xAl₂O₃ coating layer. To mimic the "natural" diffusion of Li out of Si at different delithiation rates ($\Delta N/\Delta t$), Δt was varied. Delithiation steps were repeated until there is insufficient amount of Li atoms remained in the a-Li_xAl₂O₃ layer to be removed, which is considered to be the fully delithiated state.

Based on the geometry used in our simulation, a delithiation rate of 100Li/1 picosecond (ps) is equivalent to a current density,

Current Density =
$$\frac{100 \text{ Li} \cdot (1.602 \times 10^{-19} \text{C})}{2500 \text{ Å}^2} = 6.4 \times 10^7 \text{A/cm}^2$$
 (4-2)

which is much higher than the typical current densities used in experiments ($10^{-3} \sim 10^{-6}$ A/cm²). 105,116 The fast delithiation rate in MD simulation is expected and similar to the high strain rate used in MD simulations of deformation processes. 117 In order to determine Δt for the a-Li_xSi structure to reach equilibrium at each delithiation step, we implemented a 1 D diffusion equation for the slab structure as described in the following equation

$$\frac{C-C_0}{C_S-C_0} = 1 - \frac{\pi}{4} \sum_{n=0}^{\infty} \frac{(-1)^n}{2n+1} exp\left\{\frac{-D(2n+1)^2 \pi^2 t}{4l^2}\right\} cos\frac{(2n+1)\pi x}{2l}$$
(4-3)

Initial Condition: $C(x, 0) = C_0$ for -L < x < L

Boundary Condition: $C(-L,t) = C(L,t) = C_s$ at all t

In this calculation, $C_0 = 1.095 \times 10^5 \text{ mol/m}^3$, $C_0 = 1.032 \times 10^5 \text{ mol/m}^3$, $D = 5.15 \times 10^6 \text{ cm}^2/\text{s}$, L = 24 Å

where C_0 is the initial concentration of a-Li_{3.75}Si before delithiation and C_s is the surface concentration after 100 Li atoms are removed from the a-Li₈Al₂O₃ coating. For D, constant Li

diffusivity (5.15 \times 10⁻⁶ cm²/s, determined in **Chapter 3, Section 3.4.4.** (b) for a-Li_{3,75}Si at 900 K)¹¹² was employed since at each delithiation step, the concentration gradient ($\Delta c = 3\%$) caused by removing ~ 100 Li atoms was small enough. Although the initial slab is only ~2.4 nm thick, the time estimated to reach equilibrium by solving the diffusion equation is ~ 30 ns. In other words, it still requires ~30 ns for Li to diffuse through the Si slab and reach the new uniform concentration in response to the concentration gradient ($\Delta c = 3\%$) caused by removing ~ 100 Li atoms. Such simulation time seems to be too long. Fortunately, a statistically uniform concentration within the simulation cell can be reached faster. The local Li concentration was calculated via a binning method as described in Chapter 3, Section 3.3.3. The fully equilibrated a-Li_{3.75}Si structure shows a fluctuation of c = 0.06 in each bin, where c is defined as c = x/(1+x). Based on this analysis, we can consider an equilibrium conditions or a uniform Li concentration is reached when the Li concentration difference between adjacent bins and between the maximum and minimum values were both less than c = 0.06. The time to reach this feature of equilibrium structure is approximately 0.9 ps based on local Li concentration comparison. Comparing the structures from delithiation simulation with $\Delta t = 10$ ps and $\Delta t = 1.0$ ps after 20 delithiation steps, the difference is negligible. This confirmed that $\Delta t = 1.0$ ps provides enough time for Li to diffuse and for the a-Li_xSi to relax in response to the concentration gradient caused by Li removal. Therefore, $\Delta t = 0.1$ ps and $\Delta t = 1.0$ ps were chosen to represent delithiation at fast and slow rates.

4.3.3 Analysis of Volume Contraction, Pore Evolution, and Li Trapping

In *in situ* TEM experiments, the total volume of the lithiated Si was determined by measuring the volume enclosed by the outer surface. Analogous to this definition, the volume of the slab structure, V_{total} , can be determined by the two outer surfaces. ^{46,101} Thus, the outer surface was first defined by averaging the coordination corresponding to the delithiation direction of the

outer most 10 % of Si atoms. Li concentration of the a-Li_xSi film was defined by the numbers of Li and Si atoms within the two outer boundaries, as x in Li_xSi. The local concentrations were obtained by dividing the a-Li_xSi film along the delithiation direction into 9 bins with equal size.

Upon delithiation, a-Li_xSi structures can become porous and the coating layer can also delaminate. Therefore, it is necessary and insightful to separately calculate the pore volume, V_{pore} , and the volume truly occupied by a-Li_xSi atoms, V_{true} , as

$$V_{total} = V_{pore} + V_{true} (4-4)$$

to form a complete picture. V_{pore} is the volume of any empty space generated inside the a-Li_xSi (pore) and the empty space between the a-Li_xAl₂O₃ coating layer and a-Li_xSi, leading to coating delamination. V_{pore} is computed via the Connolly volume method^{118,119} implemented in Material Studio.

The idea of "Rolling Probe" algorithm is widely implemented to calculate the accessible surface area of molecules in the field of chemistry and biology. 118,119 In the schematic, the accessible surface area is drawn with green dashed line, which is generated by tracing the center of the probe (in green) as it rolls along the surface of the atoms. Similarly, in our calculation, the volume within the locus of the probe center was considered as the volume occupied by the system. By applying the probe radius of 1.2 Å (half of the Si-Si bond length), the vacancy with single atom size was excluded (**Fig. 4-2 (b)**) but other empty spaces larger than two atoms was treated as the pore volume (**Fig. 4-2 (c)**, regions in yellow). V_{true} is computed as $V_{total} - V_{pore}$. It represents the volume of truly occupied a-Li_xSi by interconnected Li and Si, within the distance of the first nearest neighbor bond distance.

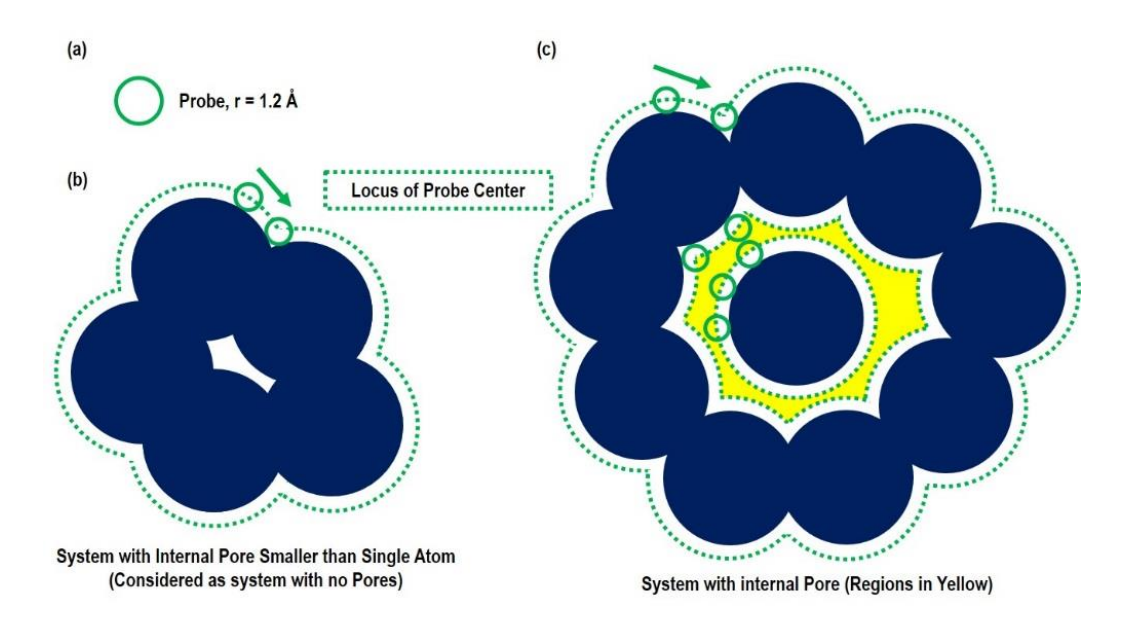


Figure 4-2 Schematic representation of Connolly volume calculation with (a) probe (b) structure with internal pore smaller than single atom size and (c) system with internal pore larger than single atom size (considered as isolated-inner pore, region in yellow)

4.3.4 Comparison between a-Li_xSi at Equilibrium and Relithiated a-Li_xSi

In addition to the slab model for delithiation, bulk a-Li_xSi with x ranging from 0.1 to 3.75 were prepared by heating and quenching method using NPT ensemble to obtain the equilibrium a-Li_xSi structures.

To study the effect of the structural changes on the subsequent lithiation cycles, the simulation was restarted from the delithiated a-Li_xSi slab after the slow delithiation. The slab was sandwiched in between two Li slabs, a similar geometry used in our previous lithiation simulation, 105 to be fully re-lithiated to Li_{3.75}Si (c = 0.789) during the 400 ps long NVT MD simulations.

4.4 Results and Discussion

4.4.1 Delithiation Proceeds with Different Rates

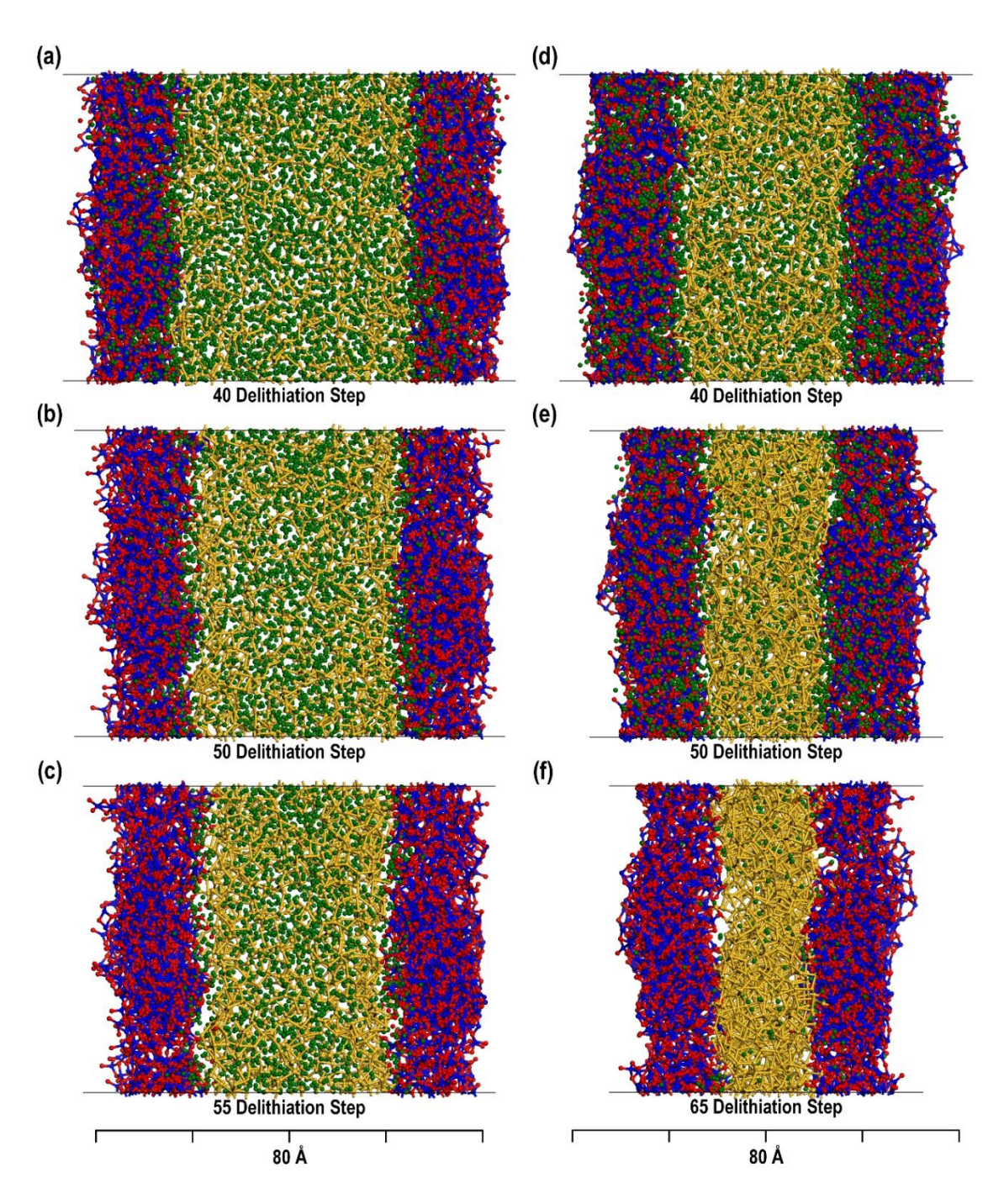


Figure 4-3 Atomic Structure Evolution. Structural snapshots at the specified delithiation steps during the continuous delithiation process with the (a) - (c) fast and (d) - (f) slow rates. In the figure, spheres in yellow, green, red, and blue represent Si, Li, O, and Al atoms, respectively

The newly developed continuous delithiation algorithm was used to track the atomistic structure evolution of a coated-Si-thin film subject to fast (shown in **Fig. 4-3 (a) - (c)**) and slow (shown in **Fig. 4-3 (d) - (f)**) delithiation rates. At time t = 0, both the a-Li_{3.75}Si film and a-Li₈Al₂O₃ coating layers were fully lithiated (**Fig. 4-1 (a)**). During each delithiation step, Li diffused from the a-Li_xSi film to the a-Li_xAl₂O₃ coating layers in response to the chemical potential gradient induced by Li-removal from the coating layer, causing the a-Li_xAl₂O₃ coating layers to be replenished. As Li atoms continuously diffused out of the a-Li_xSi, significant volume contraction occurred, accompanied by isolated inner-pores generation in the a-Li_xSi and surface delamination.

As shown in **Fig. 4-3**, the initial a-Li₈Al₂O₃ coated a-Li_{3.75}Si thin film responded differently to delithiation rates. Although the same amount of Li was removed from both structures, the volume of the delithiated a-Li_{3.75}Si thin film was always larger in the fast rate. After 55 fast delithiation steps (**Fig. 4-3 (c)**), only negligible amount of Li remained in the a-Li_xAl₂O₃ coating layers, so the delithiation simulation was terminated. In this completely delithiated structure, significant amount of Li still remained in the a-Li_xSi film. In contrast to the delithiation with fast rate, the increased relaxation time (10 times slower) is sufficient for Li to diffuse out from the a-Li_xSi to the a-Li_xAl₂O₃ layer. As a result, as shown in **Fig. 4-3 (d) - (f)**, replenishment of Li in the delithiated a-Li_xAl₂O₃ occurred, thus extending the delithiation steps up to 65. This led to a higher total delithiation capacity in the slow rate. **Fig. 4-3 (f)** shows the fully delithiated structure with the slow rate. Compared to **Fig. 4-3 (c)**, only negligible amount of Li remained in the a-Li_xSi and the higher degree of volume contraction was observed.

4.4.2 Porous Structures Evolution and Coating Delamination

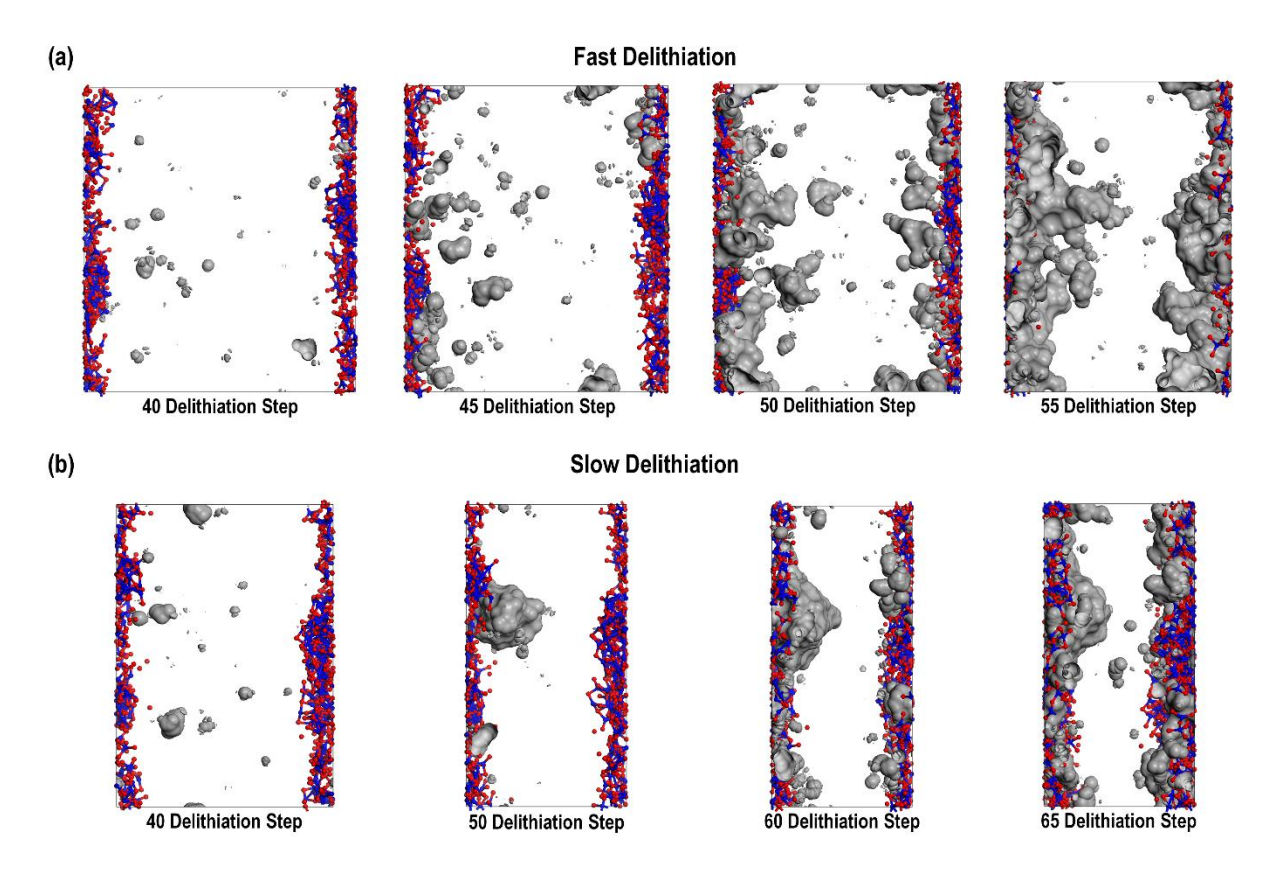


Figure 4-4 Pore Structure Evolution. Structural snapshots of the pore structure and distribution in the highlighted a-Li_xSi region during continuous delithiation process with the (a) fast and (b) slow rate

Pore structure evolution during delithiation can highlight the rate dependent irreversible structural change. **Fig. 4-4** visualizes the pores formed in the a-Li_xSi during delithiation at the given steps. During the fast delithiation, no indication of isolated inner-pores was observed until the delithiation step of 33, corresponding to a-Li_{2.8}Si. Then, isolated inner-pores formed inside the a-Li_xSi and near the interface between a-Li_xSi and the coating layer, as shown in the structure after 40 delithiation steps. As the delithiation proceeded, the isolated inner-pores and interface-pores continuously collapsed and reformed but gradually increased in size. After 50 delithiation steps, in a-Li_{1.5}Si, the pore size became significantly larger and the interface-pore size grew faster.

Eventually, most of the isolated inner-pores agglomerated with the interface-pores, generating a huge delamination pore between the coating layer and a-Li_xSi-film. In comparison, during slow delithiation, the formation of isolated inner-pores inside the delithiated a-Li_xSi was first observed after 35 delithiation steps in a-Li_{1.8}Si, but the number of pores was much less than that found in fast delithiation. As delithiation proceeded, isolated inner-pores temporarily formed and disappeared, since Li atoms had sufficient time to diffuse and the a-Li_xSi film can reach a fully relaxed state. At 45 delithiation steps with a-Li_{1.0}Si, the formation of interface-pores was observed, but no isolated inner-pores were left. Then, the interface-pore size rapidly increased around a-Li_{0.4}Si due to the severe surface delamination.

The fast and slow rates in the simulation represents equilibrium and non-equilibrium delithiaion process. Under slow rate, pores might be temporarily generated, but Li and Si atoms inside the a-Li_xSi have sufficient time to diffuse and fill the pore. The continuous formation and collapse of pores indicate that the delithiation proceeds by the formation of thermodynamically stable a-Li_xSi. During the fast rate delithiation, Li and Si atoms have insufficient time to diffuse out, especially Si will only rearrange near small pores to minimize the number of dangling bonds. Continuous removal of Li leads to pit formation and porosity; and eventually, the pore rapidly grows and agglomerates into larger voids. This confirms the nano-pores generation is a non-equilibrium process.

The evolution of porosity in Si upon delithiation resembles the selective electrochemical de-alloying process, where the evolution of nanoporous structure depends on alloy composition, particle size, and de-alloying rate. Chen *et al.* investigated the spontaneous nanostructures evolution in de-alloyed Li-Sn system and demonstrate that increasing de-alloying rate results in

nanoporous structure and pores.¹²⁰ The relationship between the pore size and diffusivity of the atoms upon de-alloying can be expressed as

$$\lambda \propto \left(\frac{D_s}{F}\right)^{\mu} \tag{4-5}$$

where the λ represents the characteristic length scale of the nanostructure, D_s is the diffusivity of adatom (Si in this case), and F is the stripping rate (delithiation rate). Thus, higher delithiation rate and slow diffusivity lead to smaller nanostructure features and more porosity while slow delithation rate and faster diffusivity lead to larger structure feature and less porosity. Even though further quantitative analysis is required, our simulation clearly captures and agrees well with this scaling law, which can also be used to control Si morphology experimentally.

The interface delamination began to grow at the stage of charge (SOC) of a-Li_{2.2}Si and a-Li_{1.0}Si, under fast and slow delithiation rate, respectively, suggesting the a-Al₂O₃ coating delamination occurs earlier with faster delithiation rate. The failure mechanism of the a-Li_xAl₂O₃ coating layer depends on the initial geometry and the mechanical constraints during lithiation/delithiation. During lithiation, the a-Al₂O₃ coating on Si-nano-wires can crack, below a critical thickness, due to the volume expansion of Si. During delithiation, it could delaminate, buckle, or crack. However, the slab model with 1-D delithiation direction implemented in this study is analogous to a Si-thin film subject to thickness change during cycling (no in-plane deformation). Although this geometry is likely to prevent buckling or cracking, it is interesting that the interface delamination occurs at the a-Li_xSi/a-Al₂O₃ interface. This is different from the a-Li_xSi/a-C coating, where the delamination occurs inside a-Li_xSi phase rather than at the interface. 122

4.4.3 Quantifying the Volume Contribution

Experimental evidence as well as MD simulations clearly indicated that the total volume of the starting material is not restored after delithiation. However, V_{total} contraction analysis analogous to experimentally measurements imposes significant limitation on understanding the effect of delithiation rates and corresponding internal volume and structural changes buried inside. Therefore, we extended our study to separate V_{pore} and V_{true} and quantified their contribution to the V_{total} of the delithiated a-Li_xSi, by the methods introduced in **Section 4.3.3**.

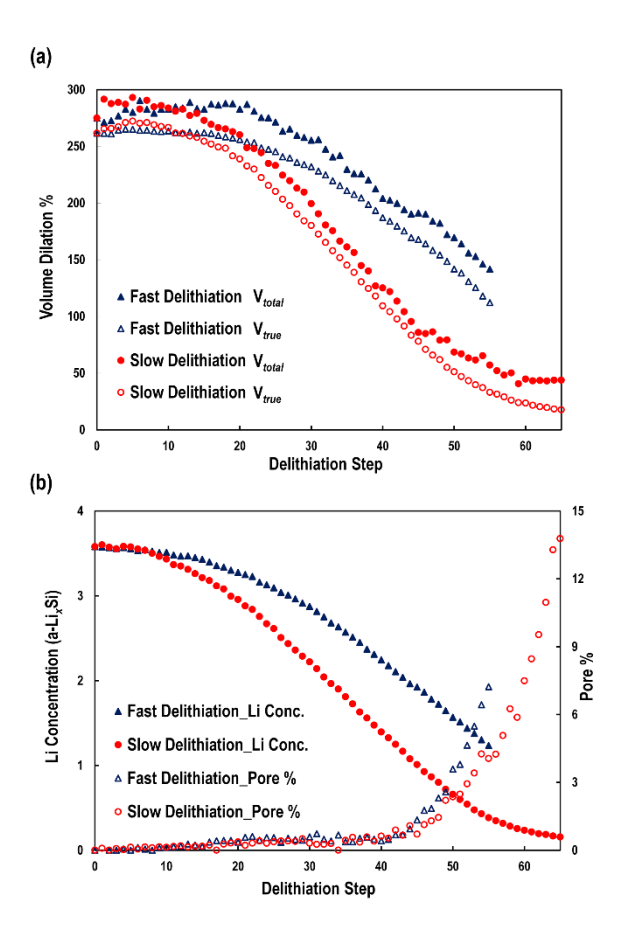


Figure 4-5 Volume and Concentration Evolution. (a) The total volume (V_{total}) and truly occupied a-Li_xSi volume (V_{true}) change normalized with respect to the unlithiated Si and (b) Li concentration and the pore volume contribution (V_{pore} / V_{total}), upon delithiation with the fast and slow rate

Fig. 4-5 (a) plotted the V_{total} and V_{true} dilation percentage with respect to the initial unlithiated Si during delithiation at different rate. The overall V_{true} contraction trend resembles V_{total} . The difference between V_{total} and V_{true} stems from V_{pore} , the total volume of all the innerpores and interface-pores formed during delithiation. Fig. 4-5 (b) quantifies the evolution of V_{pore} to V_{true} ratio as well as the Li amount left in the a-Li_xSi film.

During the initial stages of delithiation with fast rate (solid triangles on Fig. 4-5 (a)), V_{total} remained relatively constant and began to decrease after 20 delithiation steps, at a-L_{3.2}Si. The volume contraction continued throughout the remaining delithiation steps and at the final stage, the volume of the delithiated a-Li_xSi became 141 % dilated with x = 1.2 residual Li left inside. The change of volume during delithiation with slow rate (solid dots in Fig. 4-5 (a)) is characterized by three stages. Initially, V_{total} remained relatively constant until a-Li_{3.2}Si, then the volume began to decrease at a constant rate. At approximately 50 steps, the degree of V_{total} contraction decreased and leveled out around 44 % dilated with x = 0.2 residual Li left in the a-Li_xSi core.

The simulation not only captured experimentally observed trapped Li and pore generation but also provided additional quantified information and internal structural change details. Apparently, faster delithiation rate leads to more Li trapped inside the a-Li_xSi core. Although the trapped Li inside a-Li_xSi core is minimum after slow delithiation, the total volume still did not return to the original Si volume and ~ 44 % volume dilation was observed. However, the contribution of this volume dilation was not just from the porosity, which was only ~ 10 % of the V_{total} . Even V_{true} showed 17 % dilation after full delithation at slow rate. This suggests the fully delithiated a-Si may be different from the initial unlithiated a-Si.

4.4.4 Dilated a-Li_xSi Exhibits Faster Lithiation Rate in the Second Cycle

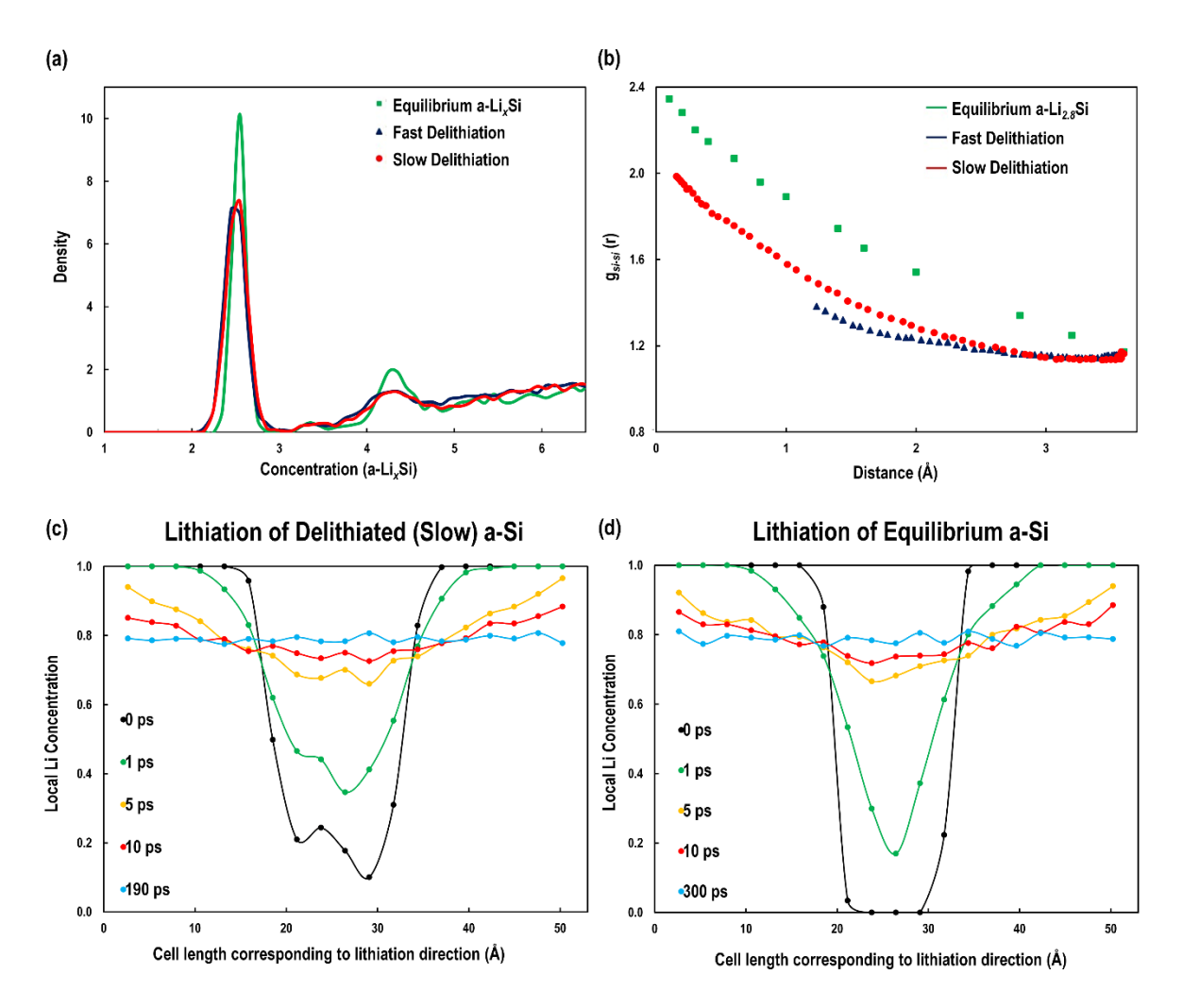


Figure 4-6 Difference in Amorphous Structures. (a) a-Li_xSi structures formed during delithiation have lower density than the equilibrium structures. Density corresponding to the delithiated a-Li_xSi upon delithiation with fast and slow rate are represented by blue and red dots. Green dots represent density obtained from the equilibrium a-Li_xSi structures (b) RDF of g_{Si-Si} (r) at 900 K of delithiated a-Li_xSi upon delithiation with fast and slow rate and equilibrium a-Li_xSi, all at concentration 2.8. Local concentration distributions at different stages of lithiation of (c) delithiated a-Si with slow rate and (d) equilibrium a-Si at 1200 K

With quantified V_{true} and Li composition in the a-Li_xSi core, the density of the delithiated a-Li_xSi structures with fast and slow rates are computed and compared with that of the equilibrium structure. **Fig. 4-6** (a) clearly indicates that delithiated a-Li_xSi with both fast and slow rates have lower density compared to the equilibrium a-Li_xSi structure at the same Li concentration. To

further investigate the structural differences, the radial distribution function of Si-Si, Li-Si, and Li-Li were analyzed for a-Li_{2.8}Si structures, which had no indication of isolated inner-pores or surface delamination. g(r) for Li-Si and Li-Li pairs were very similar with the equilibrium structure. However, the Si-Si distance, g_{Si-Si} (r), of the delithiated a-Li_{2.8}Si with fast and slow rates were different from that of the equilibrium a-Li_xSi structure, as shown in **Fig. 4-6** (b). The difference between the intensity of the peaks corresponding to the first and second nearest neighbor clearly indicates that there are less number of first and second nearest Si-Si bonds in the delithiated a-Li_{2.8}Si structures with both rates. Therefore, the excess volume in the delithiated a-Li_xSi is due to the loss of directly bonded Si-Si pairs upon delithiation.

The loss of directly bonded Si-Si pairs could impact the re-lithiation process. Kim and Qi demonstrated that breaking of the Si-Si bond is the rate limiting step of lithiation and increasing Si vacancy is one of the methods to create broken Si-Si bond in order to accelerate Si lithiation. To reveal the effect of the structural changes on subsequent lithiation rate, the a-Li_xSi structure obtained after slow rate was re-lithiated (**Fig. 4-6 (c)**) and compared with the first lithiation of an equilibrium a-Si with the same number of atoms (**Fig. 4-6 (d)**). As shown in **Fig. 4-6 (c) - (d)**, delithiated a-Li_{0.2}Si is completely mixed after 190 ps, whereas 300 ps is required to lithiated the equilibrium a-Si to become fully mixed in the first cycle. This clearly indicates that the loss of directly bonded Si-Si pairs and maybe the small amount of residual Li jointly make the delithiated a-Li_{0.2}Si exhibit faster lithiation rate in the subsequent cycle. This is likely to be the underlying reason for the change from two-phase lithiation process^{46,47} in the first cycle to one-phase lithiation process in the subsequent cycles.

4.4.5 Si Cage as the Origin of Li Trapping-Induced Irreversible Capacity Loss

Structural configurations shown in **Fig. 4-3** and Li concentration evolution of the a-Li_xSi shown in **Fig. 4-5** (b) clearly indicate that different amount of Li remained in the delithated a-Li_xSi depending on the delithiation rates. In the case of the fast delithiation, even upon complete delithiation, there was a significant amount of Li remaining in the a-Li_{1,2}Si whereas negligible amount of Li remained in the a-Li_{0,2}Si at the end of slow delithiation process.

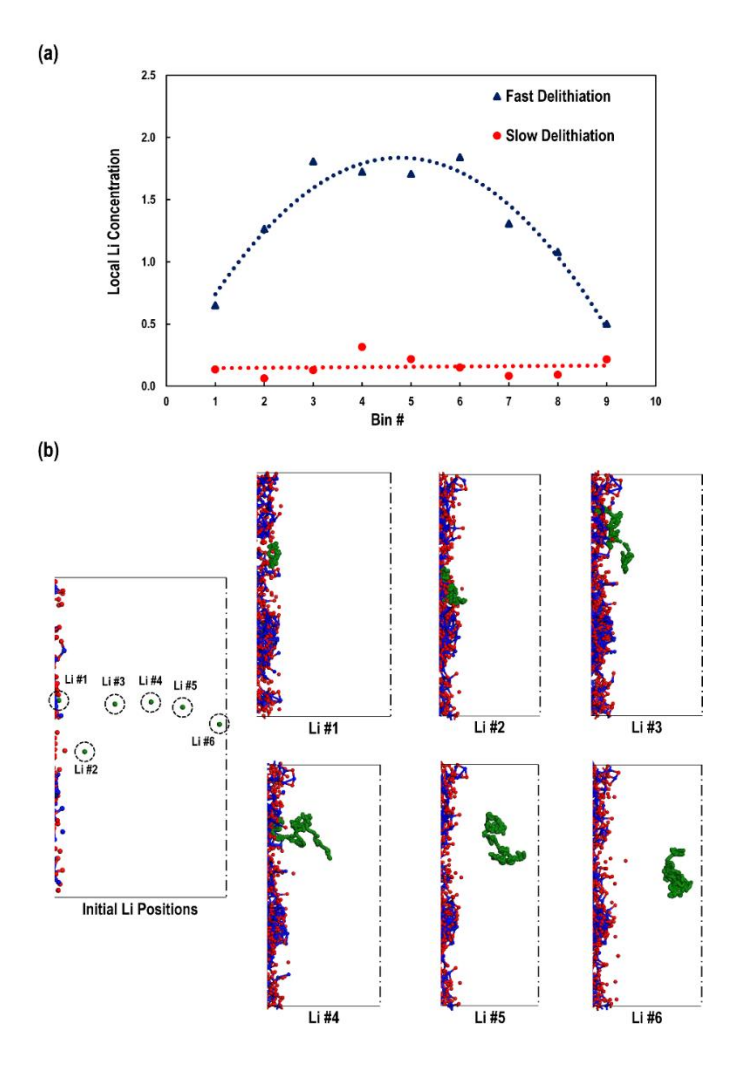


Figure 4-7 Si Cage and Trapped Li. (a) Local Li concentration distribution at the final stage of delithiation with the fast (55 step) and slow (65 step) rate (b) Li motion tracking with various initial positions during fast delithiation. In the figure, Si and Li atoms are excluded to improve the clarity. Spheres in green, red, and blue represent Li, O, Al atoms, respectively

During fast delithiation, the movement of the six individual Li atoms, at different depths inside the a-Li_xSi thin film, was tracked. The trajectories shown in Fig. 4-7 (b) indicate that, Li # $1 \sim \# 4$ all diffused out of the a-Li_xSi to the a-Li_xAl₂O₃ coating, and it took longer time for the Li deep inside the film to diffuse out. However, the Li atoms deeper inside the a-Li_xSi film (Li # 5 and Li # 6) never diffused to the surface of the a-Li_xSi, despite the driving force. As a result, the Li concentration near the surface was significantly lower than the core region. This non-uniform concentration was kept toward the end of the fast delithiation process, as shown in Fig. 4-7 (a) for the a-Li_{L2}Si structure. The lower Li concentration on the surface in turn hinders Li diffusion, since Li diffusivity is lower at low Li concentrations. 112 Therefore, a cage-like locally dense Si network was formed near the surface, in which the low Li concentration prevented other Li atoms trapped inside to escape the caged surface, as demonstrated by the motion of Li # 5 and Li # 6. In comparison, during the slow delithiation, Li had sufficient time to diffuse from the a-Li_xSi to the a-Li_xAl₂O₃ coating layer, preventing the formation of Li concentration gradient and allowed the delithiated structure to reach its fully relaxed state. Therefore, Li continuously diffused out from the a-Li_xSi and formed a-Li_{0.2}Si with uniform Li concentration, as shown in Fig. 4-7 (a).

Since the number of available Li atoms is directly related to the capacity, slow delithiation will minimize the irreversible capacity due to the number of Li trapped in the a-Li_xSi. Another efficient way to minimize the capacity loss is to avoid protective coating delamination by restricting the delithiation amount. For the slow delithiation rate (assuming equilibrium was reached in experiments), the surface delamination did not occur before Li_{1.0}Si. Therefore, if the coated Si-thin-film electrode can be cycled between a-Li_{1.0}Si \sim a-Li_{3.75}Si, coating delamination can be prevented. This can be achieved by controlling the upper cutoff voltage. Even though controlling the operating voltage limits the Si anode capacity, ^{9,33} it can beneficial in terms of the

overall battery life since it prevents the protective coating delamination from the severe volume contraction. Although this method will only use 73 % of the theoretical capacity provided by Si electrode, the capacity is still much higher than graphite electrode.

4.5 Conclusions

In this study, a ReaxFF-based MD delithiation algorithm with controlled delithiation rate was developed. The delithiation response of aluminum-oxide coated Si thin-film was simulated under slow and fast rates, representing deliathion process near and far away from equilibrium. Characteristic structural features of the Li-Si system regarding the irreversible volume change, amount of trapped Li, generation and distribution of pores, and atomistic structural difference in the amorphous structures, upon delithiation were investigated.

During the fast delithiation, due to insufficient diffusion time, a cage-like Si-rich structure was formed near the surface. Since Li diffusion in Si-rich phase is slower, the Si-cage trapped significant amount of Li inside the Si thin film. Therefore, at the end of delithiation, the composition is $\text{Li}_{1.2}\text{Si}$ and the volume dilation is ~141 %. In contrast, the slow delithiation gave Li sufficient time to diffuse out. Thus, an almost Li-free structure, $\text{Li}_{0.2}\text{Si}$, with 44 % volume dilation was obtained, and no permanent inner pores, except coating delamination was observed. Even when there is no trapped Li, the delithiated amorphous Li_xSi always exhibited larger volume (lower density) than the equilibrium structure with the same Li concentration, regardless of the delithiation rates. This is due to the loss of directly bonded Si-Si pairs, which made the delithiated a-Li_{0.2}Si exhibit faster lithiation rate in the next cycle.

Quantifying the trapped Li clearly indicates that fast delithiation resulted in higher irreversible capacity loss compared to the slow delithiation due to the significant amount of Li

trapped in the a-Li_xSi. This study also suggests that controlling the upper cutoff voltage to keep the coated Si-thin-film electrode to be cycled between a-Li_{1.0}Si \sim a-Li_{3.75}Si will benefit the overall battery life since it prevents the protective coating delamination.

Chapter 5 Reactive Force Field Evaluation for Lithiation/Delithiation in Si-O

5.1 Introduction

Silicon Monoxide (SiO) is another promising candidate for anode material with significantly higher capacity than graphite and enhanced cycle life compared to Si due to its unique microstructure and formation of irreversible sub-phases that can alleviate the volume expansion upon lithiation/delithiation. ¹⁰⁷⁻¹²³

The microstructure of SiO has been debated over the past few decades with two main models. In the random bonding model (RB), SiO is considered as a single-phase material with randomly distributed Si-Si and Si-O bonds. ^{123,124} Random mixture model (RM) assumed SiO is composed of randomly distributed n-Si grains within a SiO₂ matrix, implying a two-phase mixture. ^{125,126} Recently, experimental observation and theoretical calculations have suggested that solid SiO is thermodynamically unstable and undergoes a disproportionation reaction, where SiO segregates into Si and SiO₂ clusters surrounded by the Si-suboxide matrix under heat treatment, suggesting the RM model. ^{129,131,137} To elucidate the controversial microstructure of SiO, Schulmeister *et al.* ¹³⁰ performed structural analysis of a-SiO using TEM, EELS, and ESI and revealed that SiO is rather inhomogeneous mixture of a-Si and a-SiO₂ than single-phase compounds (a RM model). Furthermore, Park *et al.* ¹²⁹ investigated the structural evolution of SiO upon heat treatment at high temperature ranging from 800 °C ~ 1200 °C and observed segregation of thermodynamically unstable SiO into well-distributed nanocrystalline Si grains within an a-SiO₃ matrix (a RM model), also known as the disproportionation reaction.

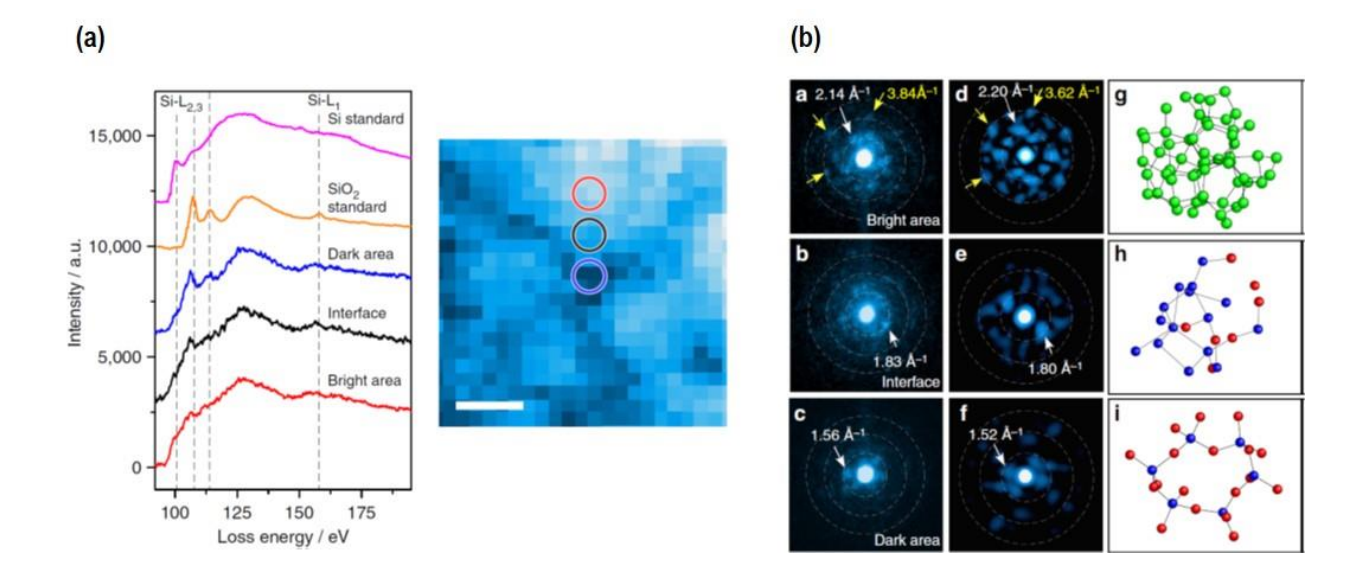


Figure 5-1 (a) EELS profiles (Si-K edge) taken from the three different regions in the HAADF-STEM image (b) Experimental (a) - (c) and simulated (d) - (f) ABED images corresponding to Si ,SiO₂, and interface regions (Adapted from reference [¹³³]. Copyright © Nature Communications 2016)

Direct evidence on the atomic-scale disproportionation reaction and existence of the distinctive interface in SiO were proved by local structural analysis of SiO using angstrom-beam electron diffraction (ABED) and synchrotron high-energy XRD (HEXRD). As shown in **Fig. 5-1** (a), EELS profiles (Si-K edge) taken from the dark (a-SiO₂), interface, and bright regions (a-Si) clearly indicates that each regions have characteristic Si bonding environment. Furthermore, complicated bonding nature at the interface and ABED patterns were computationally investigated using Molecular Dynamics and Reverse Monte Carlo Method, ¹³³ which confirmed the presence of suboxide-type tetrahedral coordinates (Si-(3Si,O), Si-(2Si,2O), and Si-(Si,3O)) in the interface regions.

Electrochemical reaction of SiO is characterized by the formation of irreversible subphases and reversible $\text{Li}_x\text{Si.}^{29,127,131,135}$ Various experimental methods including NMR, ^{127,135} XPS, ¹²⁷ electrochemical dilatometry were used to analyze the structure before and after the electrochemical lithiathion/delithiation and verified the existence of Li-silicates, mainly Li₄SiO₄, and Li₂O. Based on the initial capacity, irreversible capacity, and presence of irreversible Li-silicates and Li₂O, lithiation of SiO was proposed to proceed by lithiation of SiO_x sub-oxide with generation of various Li-silicates, followed by lithiation of c-Si or a-Si into Li_xSi with continuous formation of Li₄SiO₄ and Li₂O. Since the densities of Li₄SiO₄ and Li₂O are much higher than Li_xSi, they are considered to act as a buffer to accommodate the large volume expansion. Jung and co-workers¹³ further investigated the roles of various Li-silicates (Li₂Si₂O₅, Li₆Si₂O₇, and Li₄SiO₄) and Li₂O using DFT and validated oxygen atoms reduce the space occupied by Li, thus responsible for the alleviated volume expansion. Also, it was suggested that Li-silicates (mainly Li₄SiO₄) are dominant over Li₂O as irreversible sub-phases. Finally, Li diffusivity calculation using climbing-image nudged elastic band (CI-NEB) revealed Li diffusion in Li₂O is at least 2 orders faster than that of other silicates, highlighting the importance of Li₂O in mitigating the volume expansion and increasing the rate performance.

Evolution of the RM-two-phase microstructure upon lithiation and failure mechanism upon delithiation still remains unclear due to the limitation of experiment methods and computational power. Experiment methods are not sensitive enough to capture the atomic-level evolution of the dynamic structural changes upon lithiation/delithiation. In terms of simulation using DFT, it is even more challenging since the RM-two-phase geometry is difficult to describe with limited number of atoms. Therefore, it is necessary to use atomistic simulations to simultaneously track and correlate the microstructural evolution and failure mechanism of SiO upon lithiation/delithiation. Prior to simulating the lithiation and delithiation dynamics of SiO, it is necessary to evaluate whether the reactive force field parameters can successfully capture the phase stability of Li-Si-O system. Therefore, we evaluated the performance of reactive force field⁷⁴

developed for Li/Al/Si/O/H system (ReaxFF used in delithiation simulation from chapter 4) to check its application to simulate lithiation/delithiation of SiO.

5.2 Simulation Methods

5.2.1 First-principles DFT Calculations

To generate the optimized RB-single-phase structures of a-Si, a-SiO, and a-SiO₂ using first-principle DFT calculations, AIMD was performed, as implemented in the Vienna Ab Initio Simulation Package (VASP). Projector-Augmented-Wave (PAW) potentials were used to calculate the interaction between ion cores and valence electrons. For exchange-correlation functional, generalized gradient approximation (GGA) in the Perdew-Burke-Ernzerhof (PBE) was utilized. Due to the large simulation size and amorphous nature, k-point mesh of 1×1×1 was employed to save an enormous amount of computational time during the ab initio molecular dynamics simulations. From the convergence test with criteria of 1 meV/atom, 550 eV used as the energy cutoff.

The initial RB-single-phase structures for a-Si, a-SiO, and a-SiO₂ were generated by randomly distributing Si and O atoms into a simulation cell with appropriate ratio at a density of 2.26, 2.21, and 2.17 g/cm³, which values were adopted from first-principle calculation of Si-O system.¹³⁹ Once the initial structures were prepared, amorphous Si, SiO, and SiO₂ were generated by melting-and-quenching process using AIMD, followed by relaxation. First, the initial structures were completely melted at 2500K for 5 ps, which temperature is sufficiently higher than the melting point of a-Si, a-SiO, and a-SiO₂. Then, the structure was sequentially quenched to the room temperature at a rapid rate of 200 K per 1000 MD time steps, where each MD timestep corresponded to 1.0 fs. Once the temperature reached the room temperature, each system was

allowed to equilibrate for 5 ps, followed by relaxation with energy cutoff of 550 eV and atomic force tolerance of 0.02 eV/Å. The calculated density of a-Si, a-SiO, and a-SiO₂ were 2.28, 2.19, and 2.23g/cm³, which were good agreement with the experiments and theoretical studies. ^{13,29,139}

5.2.2 ReaxFF-based Molecular Dynamics Calculations

To generate the optimized structures of a-Si, a-SiO, and a-SiO₂ using ReaxFF, density of a-Si, a-SiO, and a-SiO₂ were calculated by using the initial RB-single-phase structure generated in **Section 5.2.1**. Each structure was first melted at a high temperature (2500 K) and then quenched to room temperature via NPT ensemble, resulting in density of 2.44, 2.76, and 2.29 g/cm³ for a-Si, a-SiO, and a-SiO₂, respectively. The optimized structure generated for a-SiO is a RB-single-phase material with uniformly distributed network of Si and O.

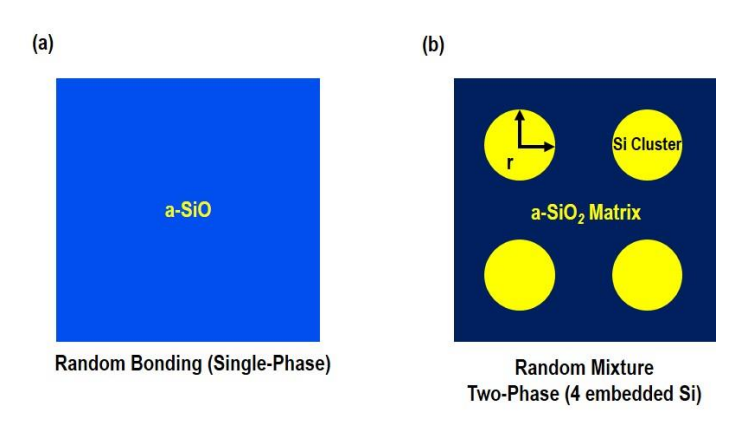


Figure 5-2 Schematic of (a) random bonding and (b) random mixture a-SiO

To construct a RM-two-phase SiO structure observed in experiments, three representative random mixture SiO structures were generated. To generate these structures, the microstructure of the initial structure was simplified into a model with a-Si embedded inside the a-SiO₂ matrix. Based on the density obtained by ReaxFF-NPT MD simulations, three independent structures with

1, 4, 9 embedded Si regions were engineered inside a simulation cell of 50 Å \times 50 Å \times 20 Å (**Fig. 5-2 (b)**). To represent the experimentally observed random mixture microstructure with the size of the Si cluster regions around 1 \sim 5 nm^{29,140}, radius of each structures were designed to be 15.572, 7.786, and 5.191 Å. Each system was composed of 1600 Si atoms and 1600 O atoms with total density of 2.34 g/cm³.

To compare the phase stability between the RB-one-phase and the RM-two-phase microstructures, two RB-one-phase SiO structures with different densities of 2.34 and 2.76 g/cm³ were generated. Each density was chosen to represent the structure directly comparable to the simplified RM-two-phase SiO with a linear combination of the densities and RB-single-phase structure optimized by ReaxFF-NPT simulation. To prepare the RB-single-phase SiO, simulation cells with 1600 Si atoms and 1600 O atoms with density of 2.34 and 2.76 g/cm³ were prepared. Then, ReaxFF-NVT simulations were performed at 4000K for 10 ps, followed by continuous run at 300K for 10 ps. The volume was kept constant throughout MD simulations to maintain the density. Detailed dimensions for simulation cells are listed in **Table 5-1**.

Structure	Microstrucure	# of Si	Radius of Si	Total Density	Density Cell Le		(Å)	# of atoms	
		Clusters	Clusters (Å)	(g/cm^3)	X	y	Z	Si	О
a-Si	Random Bonding	-	1	2.44	-	-	1	ı	-
a-SiO ₂	Random Bonding	-	-	2.29	-	-	-	1	-
a-SiO	Random Bonding	-	-	2.76	42.304	50	20		
		-	-	2.34	50.047	50	20		
	Random Mixture	1	15.572	2.34	50.000	50	20	1600	1600
		4	7.786	2.34	50.000	50	20		
		9	5.191	2.34	50.000	50	20		

Table 5-1 Summary of density, microstructure, and simulation size of a-Si, a-SiO, and a-SiO₂

5.3 Results and Discussions

5.3.1 Direct Energy Comparison of ReaxFF versus DFT

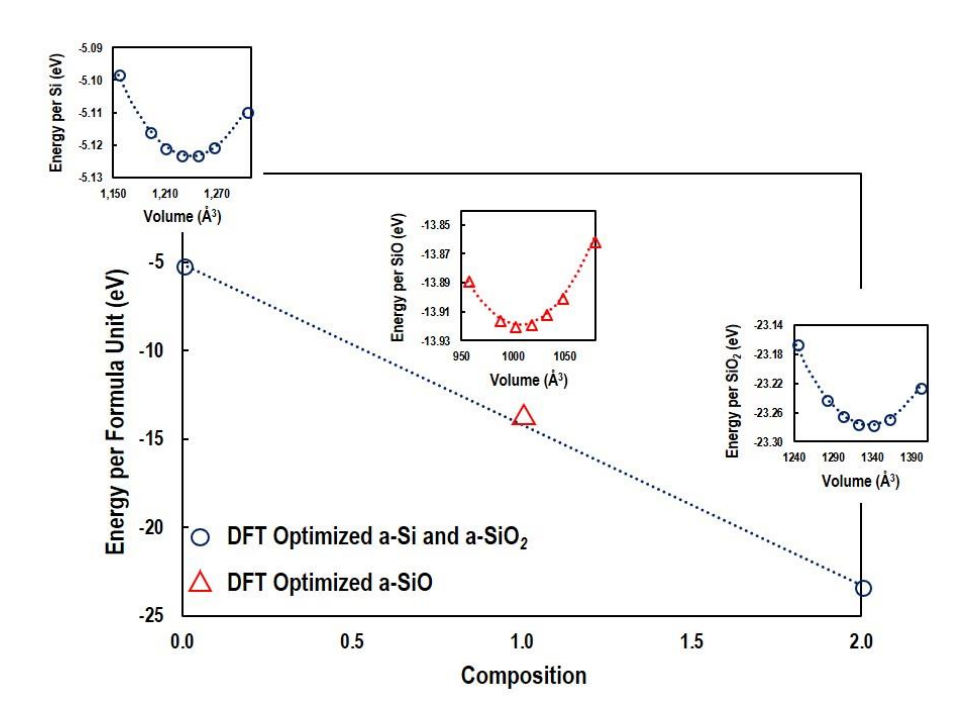


Figure 5-3 Energy calculation of a-SiO $_{0.5}$, a-SiO, and a-SiO $_{2}$ with equation of states

In addition to the large systems, bulk structures of a-Si, a-SiO ($\rho = 2.76~g/cm^3$), and a-SiO₂ with much smaller size (total number of atoms being less than 100 atoms) were also generated using the density predicted by ReaxFF-NPT simulation, followed by ReaxFF-NVT simulation at 4000K and 300K. The energies of smaller structures were calculated by DFT and ReaxFF to evaluate the performance of the ReaxFF parameters.

The energy of the DFT-optimized a-Si, a-SiO, and a-SiO₂ along with equation of states using DFT are presented in **Fig. 5-3**. The energy of the optimized a-Si, a-SiO, and a-SiO₂ structures generated using first-principle DFT calculations are -5.17 eV, -13.96 eV, and -23.39 eV,

respectively. Phase stability of SiO was determined by calculating the "Formation Energy (ΔE_f)" for a-SiO, which can be expressed as

$$\Delta E_f = E_{SiO} - \frac{1}{2} \left(E_{Si} + E_{SiO_2} \right) \tag{5-1}$$

where E_{Si} , E_{SiO} , and E_{SiO_2} represents the total energy per formula unit of a-Si, a-SiO, and a-SiO₂, respectively.

Structure	Energy Calculation	Energy per Formula Unit (eV)			Formation Energy	Phase Stability of Random Bonding	
Generation Method	Method	a-Si	a-SiO	a-SiO ₂	(eV)	SiO	
AIMD	DFT	-5.173	-13.959	-23.387	0.321	Unstable	
Alvid	ReaxFF	-4.395	-10.336	-17.312	0.518	Unstable	
ReaxFF-MD	DFT	-4.928	-7.716	-21.929	5.713	Unstable	
Keaxi'r-MD	ReaxFF	-4.651	-14.620	-19.901	-2.344	Stable	

Table 5-2 Summary of energy calculation of a-Si, a-SiO, and a-SiO₂ from optimized structures generated by first-principle DFT calculations and ReaxFF-MD simulations

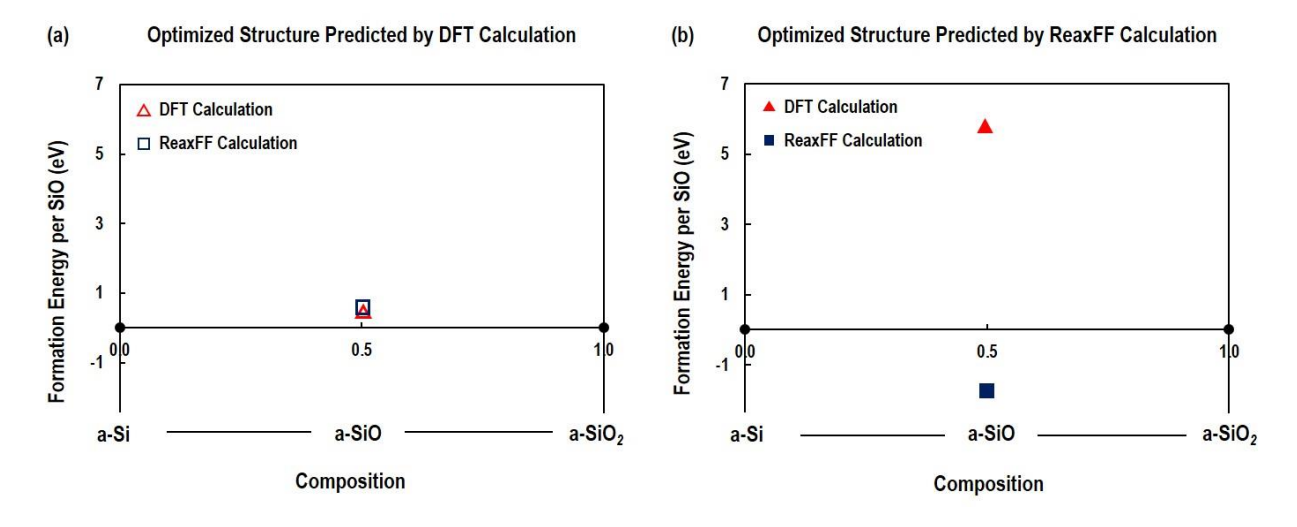


Figure 5-4 Formation energy of a-SiO with (a) DFT optimized and (b) ReaxFF-MD optimized structure. The red and blue data points represent DFT and ReaxFF-MD energy calculation, respectively

Table 5-2 summarizes the information regarding the energy of a-Si, a-SiO, and a-SiO₂ calculated from the DFT-optimized and ReaxFF-MD optimized structures. Fig. 5-4 compares the formation energy calculated using different calculation methods for the two structures generated by AIMD and ReaxFF-MD, respectively. The formation energy of the DFT-optimized RB-singlephase structure using DFT method is 0.321 eV. This indicates that RB-single-phase SiO is thermodynamically unstable and the microstructure should segregate into two-phase. Also, the formation energy of the AIMD generated RB-single-phase a-SiO calculated by ReaxFF method is 0.518 eV, which indicates ReaxFF can successfully predict the energetics of the thermodynamically unstable a-SiO structure generated by AIMD calculation. In contrast to the energy calculation from the AIMD-optimized structure which both calculation method agrees with each other, the energy calculation of the ReaxFF-MD optimized structure using ReaxFF predicts a negative formation energy whereas DFT method predicts a positive formation energy, as shown in Fig. 5-4 (b). In other words, even though ReaxFF-MD optimized structure is unstable with positive formation energy as predicted by DFT method, ReaxFF is predicting this structure to be stable with negative formation energy. This is why this erroneous structured can be generated by the ReaxFF-MD.

5.3.2 Non-Physical SiO Structure Predicted by ReaxFF-MD

In this section, the phase stability of the SiO with RB-single phase and RM-two-pahse microstructures was further evaluated by ReaxFF method.

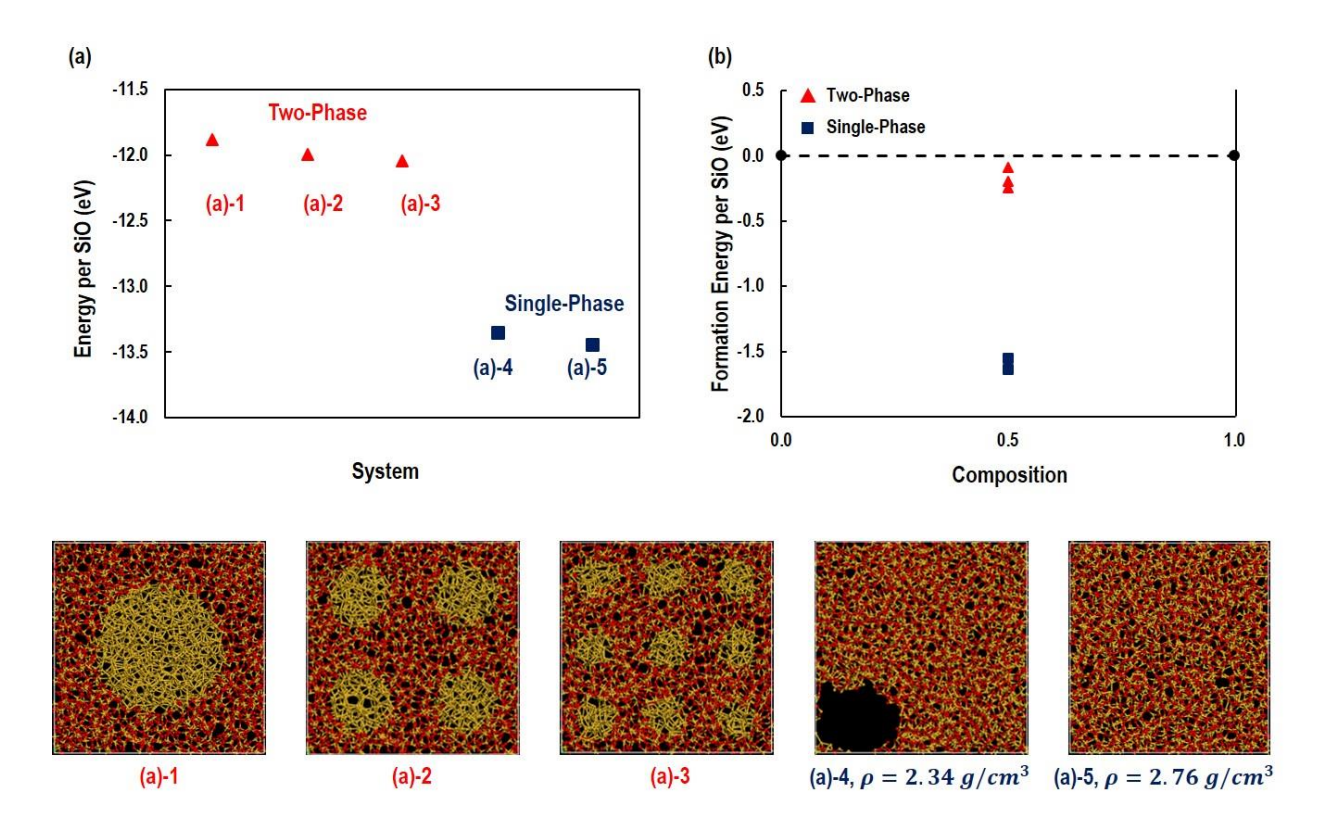


Figure 5-5 (a) Energy Comparison of random bonding and random mixture a-SiO with its unique microstructure. (a) - # represents the microstructure of a-SiO corresponding to the energy. In the figure, spheres in red and yellow represent O and Si atoms, respectively (b) Formation energy (ΔE_f) of a-SiO structures

As clearly indicated from the energy plot (**Fig. 5-5 (a)**), the energy of RB-single-phase SiO is significantly lower than those of RM-two-phase SiO. In other words, ReaxFF-MD predicts the RB-single-phase a-SiO is more thermodynamically stable than the RM-two-phase a-SiO. It is interesting to note ReaxFF-NVT simulations at density of 2.33 g/cm³ (**Fig. 5-5 (a) - 4**) results in a structure with a huge hole at the left corner of the simulation box, indicating the RB-sinlge-phase SiO is extremely unstable at this density (strong Si-O bond predicted by ReaxFF) and returns to it optimized state at density of 2.76 g/cm³. Also, the formation energy of each structures was computed using the energies obtained from ReaxFF-MD NPT simulations for a-Si and a-SiO₂. Regardless of the microstructures, ReaxFF predicted negative formation energies for all the

structures. This is not consistent with many reported experimental observations and contradicts the DFT calculations, which predicted RB-single-two-phase is energetically unstable.

5.3.3 Reason for the Errors in the MD Results

The discrepancy between the optimized structures and corresponding energetic using first-principle DFT and ReaxFF is due to the scope of the training set which ReaxFF is trained on. As described in **Chapter 3**, **Section 3.3.1**, van duin *et al.*⁷³ trained the ReaxFF for Si and Si-Oxide system for a wide variety of well-known condensed phases and clusters of Si and SiO₂.

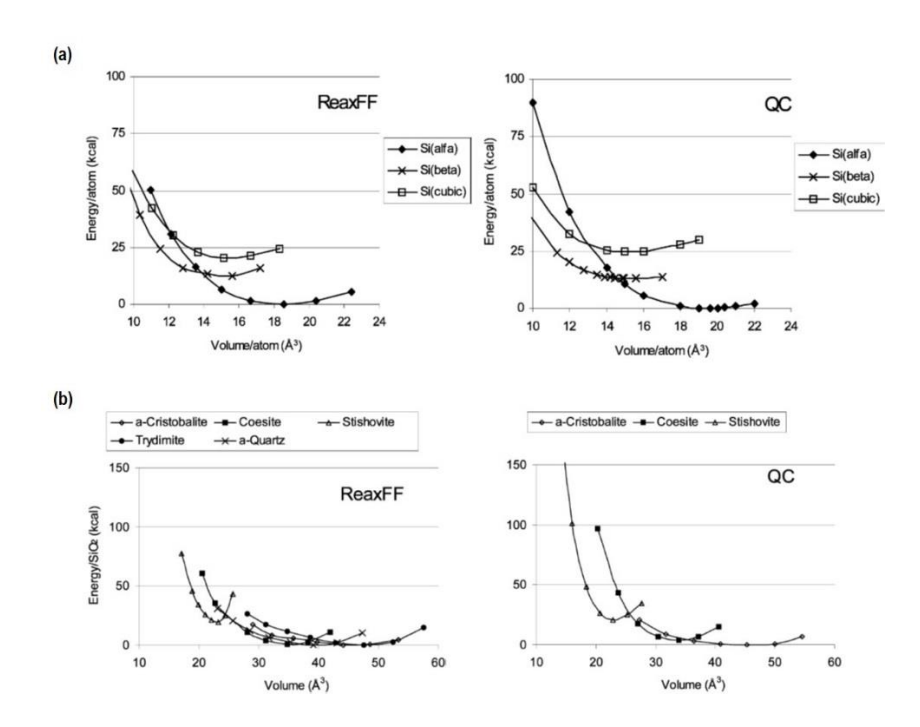


Figure 5-6 Energy calculation using DFT and ReaxFF methods for (a) three different Si phases and (b) various silicon dioxide phases at different densities for ReaxFF fitting (Adapted from reference [⁷³]. Copyright © The Journal of Physical Chemistry A 2003)

Fig. 5-6 shows one example of the evaluation of the ReaxFF trained for Si and SiO₂ with different crystal structures based on equation of states comparison. As clearly shown in the energetics, ReaxFF successfully captures the energy change upon different densities of different

Si $(\alpha, \beta, \text{ and simple cubic Si})$ and SiO₂ phases $(\alpha - \text{cristobalite}, \text{coesite}, \text{ and stishovite SiO}_2)$. Even though this set of ReaxFF parameters can accurately describe the chemistry and physical environment of the Si and SiO₂ phases which were accurately fitted to against the quantum calculation, they perform poorly in the regions which are not included in the training set, such as SiO. As explained, the RB-single-phase SiO is thermodynamically unstable phases. Since the set of ReaxFF parameters was not carefully fitted or learned from this unique environment of SiO, it is extremely difficult to successfully capture the properties of SiO accurately. This is the reason behind the contradiction of the formation energy calculated from the ReaxFF-optimized structure. Therefore, it is necessary to refit the ReaxFF parameters with a range of metastable a-SiO_x structures between a-Si and a-SiO₂ to properly describe the phase stability of SiO.

5.3.4 Design of the Training Set for Li-Si-O System

To successfully describe the phase stability and further simulate lithiation/delithiation of SiO, the training set which describes the Li-Si-O system needs to be extended and include range of a-SiO $_x$ structures between a-Si and a-SiO $_z$ with corresponding energies calculated from first-principle DFT calculations.

Parametrization of ReaxFF with extended training set should be proceeded via a two-step procedure. First, to capture the energetics of unique SiO_x microstructure, it is important to successfully describe all possible environments between the composition range of $x = 0 \sim 2$ for SiO_x . Also, structures within this range must be allowed to evolve to the optimized structures with the correct energies at the corresponding composition. Therefore, it is necessary to optimize Si/O parameters by fitting against equations of state of several representative metastable phases including a-Si, a-SiO_{0.5}, a-SiO, a-SiO_{1.5}, and a-SiO₂. Once the Si/O parameters were tuned, then

Li/Si/O parameters also require modification to accurately simulate the lithiation/delithiation of SiO_x system. For this purpose, Li/Si/O parameters should also be refitted against equation of state of a-Li_xSiO_{0.5}, a-Li_xSiO, a-Li_xSiO_{1.5}, and a-Li_xSiO₂ where x ranges from 0 to 6. Similar to the method used in the original training set,⁷⁴ these equations of state should be computed for volume changes ranging from 50 % compression to 20 % expansion.

5.4 Conclusions

In this study, the performance of ReaxFF developed for Li/Al/Si/O/H system was evaluated to check its transferability to describe the phase stability of SiO. Formation energy of DFT-optimized and ReaxFF-MD optimized SiO structure was compared using DFT and ReaxFF calculation method.

Formation energy calculation of DFT-optimized SiO structure indicates that regardless of the calculation method, the structure is predicted to be thermodynamically unstable with positive formation energy. However, the sign of the formation energy of the ReaxFF-MD optimized SiO structure differs depending on the calculation method. DFT method predicts a positive formation energy whereas ReaxFF method predicts a negative formation energy, which discrepancies stems from the lack of training set describing the metastable a-SiO regions. Since the parameters describing the reaction of Si and O was only learned from equation of state of various c-Si and c-SiO₂ and some clusters, it is extremely difficult for ReaxFF to predict metastable a-SiO regions with completely different structural motifs than Si and SiO₂. Therefore, to successfully describe the phase stability and further perform lithiation/delithiation of SiO, it is necessary to expand the training set with a range of metastable a-SiO_x including a-Si, a-SiO_{0.5}, a-SiO, a-SiO_{1.5}, and a-SiO₂ as well as their lithiated phases.

The training set for SiO_x system which include different crystal structures of Si and SiO_2 as well as amorphous $SiO_{0.5}$, SiO, and $SiO_{1.5}$ has been generated. The new parameters will be generated via fitting procedure using genetic algorithm through a collaboration with Dr. Aktulga and Dr. van Duin's group.

Chapter 6 Generation of Li-Si Training Set for Machine-Learning Potential

6.1 Introduction

Up to this point, all the ReaxFF-based atomic simulations were performed using the ReaxFF developed for Li-Si ⁵⁹ and Li-Si-Al-O-H system. ⁷⁴ Although ReaxFF trained against DFT calculations can accurately describe the chemical reaction, methodology regarding the development of such force field has several disadvantages. ^{141–143} The construction of accurate interatomic potentials (or force field) is a repetitive task of training against extensive first-principle calculations which generally result in several months of "laborious iterative fitting". Furthermore, even after an acceptable potential has been formed, extension to new systems is difficult because of the complex interdependence of all parameters which often requires introduction of new energy terms based on trial and error. To efficiently develop interatomic potentials which provide reliable energies and forces, currently a paradigm change is taking place in the development methodology.

Machine-Learning Potentials (MLP)^{142–147} have been introduced as an alternative approach to obtain the accuracy of first-principle calculations and the efficiency of a force field based on functional forms. Different from the force fields which are developed on functional forms, MLP employs purely mathematical fitting techniques to construct a direct relation between the atomic configuration and corresponding energies based on the training-set consisted of accurate first-principle calculations. The advantage of MLP is that the development procedure can be well-automated so that extension of the potentials for new system can be performed with minimum human intervention. Also, the flexibility of the mathematical potential model allows the MLP to reach the accuracy that is comparable to the training set used in their construction. However, the

characteristic mathematical potential model of MLP also causes a significant limitation. Due to the non-physical form of MLP, it is difficult to directly interpret the model parameters and describe the regions that are not included in the training set. Therefore, the quality of the MLP significantly depends on the training set and it is most important to construct an extensive training set which samples all relevant atomic interactions and environments.

In this chapter, systematic method to generate accurate and extensive training set for Li-Si system is introduced. Li-Si system was specifically chosen because of its wide application in battery simulation since Si is widely studied as a promising anode material. Furthermore, lithiation of c-Si at room temperature proceeds via solid-state amorphization, thus require investigation of amorphous systems. Generally, it is difficult to characterize the amorphous phases with experiment techniques since they are not sensitive enough to capture the wide variety of local structural motifs. First-principle calculations can provide insights regarding phase stability and atomic structures but due to the computational cost, the number of the atoms are limited to hundreds of atoms. Therefore, it is particularly important for amorphous phases to be studied in large scale with longer dynamics with first-principle accuracy and interatomic potential efficiency. In this purpose, extensive training set which MLP can be learned was developed and the performance of the training set was evaluated by computing energies, voltages, chemical properties, and mechanical properties with DFT calculations.

6.2 Automated Construction of the Training Set with Crystalline and Amorphous Li_xSi

6.2.1 $c-Li_xSi$ structures

The crystalline phases with composition Si, Li, LiSi, Li₁₂Si₇, Li₁₂Si₃, Li₁₃Si₄, and c-Li₁₅Si₄ were obtained from crystal structure database from Material Project. First-principle DFT

calculations were performed as implemented in the VASP with PAW method to describe the interaction between ion cores and valence electrons. For exchange-correlation functionals, GGA method was utilized. The energy cutoff was determined to be 550 eV. The optimized lattice parameters and K-point mesh are summarized in **Table 6-1**.

Phase	Space Group	a (Å)	b (Å)	c (Å)	k-point Mesh
Si	$Fd\overline{3}m$	10.861	10.861	10.861	4×4×4
LiSi	I41/a	9.340	9.340	5.760	4×4×4
Li ₁₂ Si ₇	Pnma	8.554	19.657	14.310	4×4×4
Li ₇ Si ₃	C2/m	7.629	6.607	18.009	5×5×5
Li ₁₃ Si ₄	Pbam	7.972	15.143	4.450	6×6×6
Li ₁₅ Si ₄	<i>I</i> 43d	10.655	10.655	10.655	3×3×3
Li	Im3	7.018	7.018	7.018	6×6×6

Table 6-1 Structural parameters for c-Li, c-Si, and c-Li_xSi alloys at equilibrium

6.2.2 a-Li_xSi Structures

To generate extensive training set which includes a wide range of local structural motifs of a-Li_xSi system, I classified the training set into three categories based on their energy states. These three categories are 1) **Liquid-like a-Li_xSi structures, 2**) **Near-Ground-State a-Li_xSi structures,** and 3) **Intermediate a-Li_xSi structures.** The Liquid-like a-Li_xSi structures represents the local structural motifs at the highest energy state. The near-ground-state a-Li_xSi represents the equilibrium structures of metastable a-Li_xSi with the lowest energy. The intermediate a-Li_xSi structures represent the configurational space between the liquid-like and near-ground-state a-Li_xSi. These three categories together cover the possible configurational space occurring in a-Li_xSi system. Amorphous Li_xSi structures at different energy states were generated using a combination of ReaxFF-based MD along with AIMD and optimization protocol in the framework of DFT.

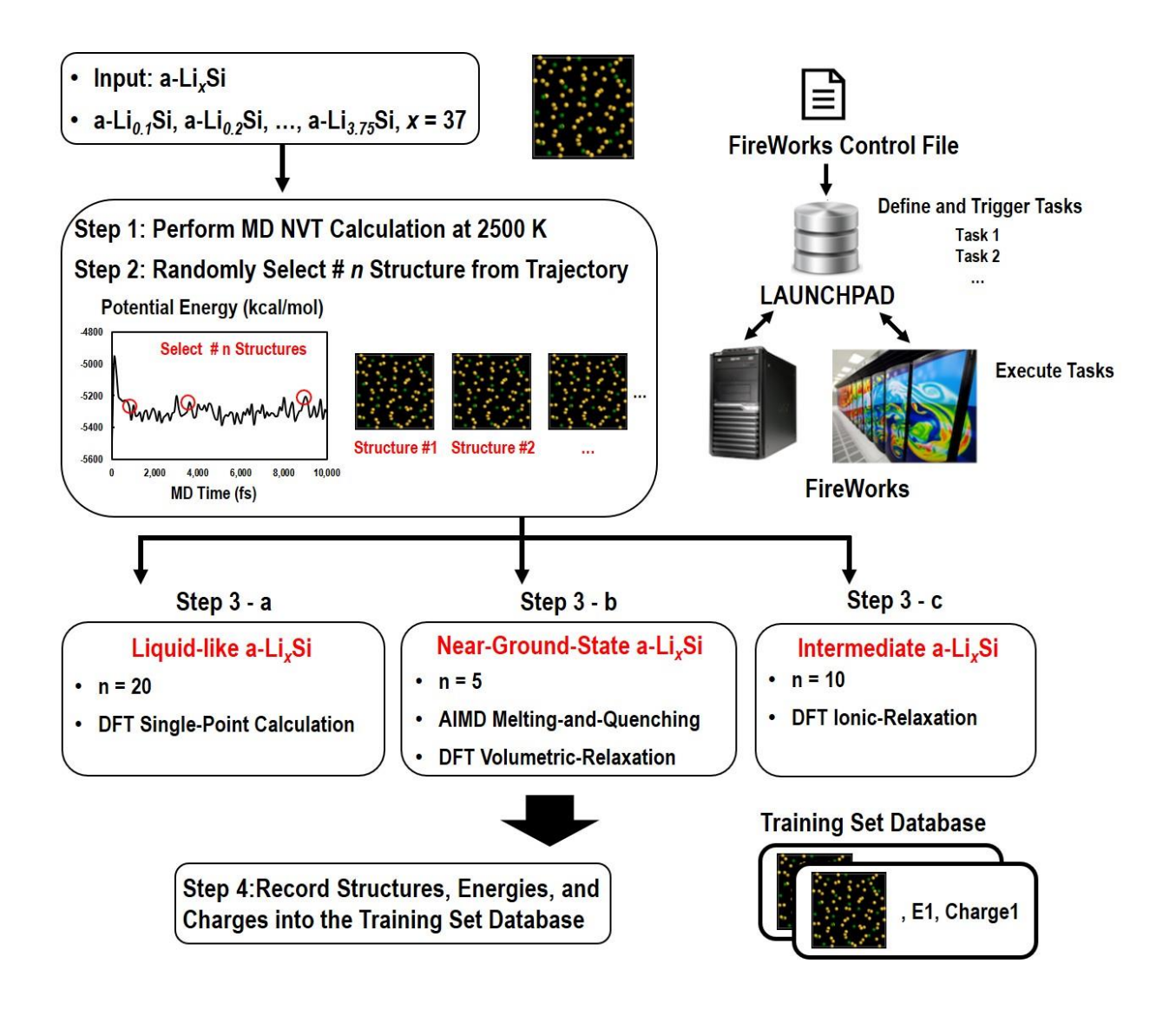


Figure 6-1 Flow chart describing the automated protocol to construct the Li-Si training set

Fig. 6-1 illustrates the flow chart of the automated protocol to construct the Li-Si training set. First, initial configurations of a-Li_xSi structures with concentration ranging from $x = 0.1 \sim 3.75$ were prepared by approximating the densities with corresponding concentrations. The densities of a-Si, a-LiSi, a-Li₂Si₇, a-Li₇Si₃, a-Li₁₃Si₄, and a-Li₁₅Si₄ were calculated from melting-and-quenching process from their crystalline counterparts. Similar to the process used in **Chapter 3**, **Section 3.3.3**, each structure was melted at high temperature of 2500K, followed by quenching process to room temperature using NPT dynamics while the ratio of Li and Si was kept constant.

The calculated density of a-Si, a-LiSi, a-Li $_{12}$ Si $_{7}$, a-Li $_{7}$ Si $_{3}$, a-Li $_{13}$ Si $_{4}$, and a-Li $_{15}$ Si $_{4}$ were 2.44, 1.91, 1.64, 1.48, 1.26, and 1.19 g/cm $_{3}$, respectively.

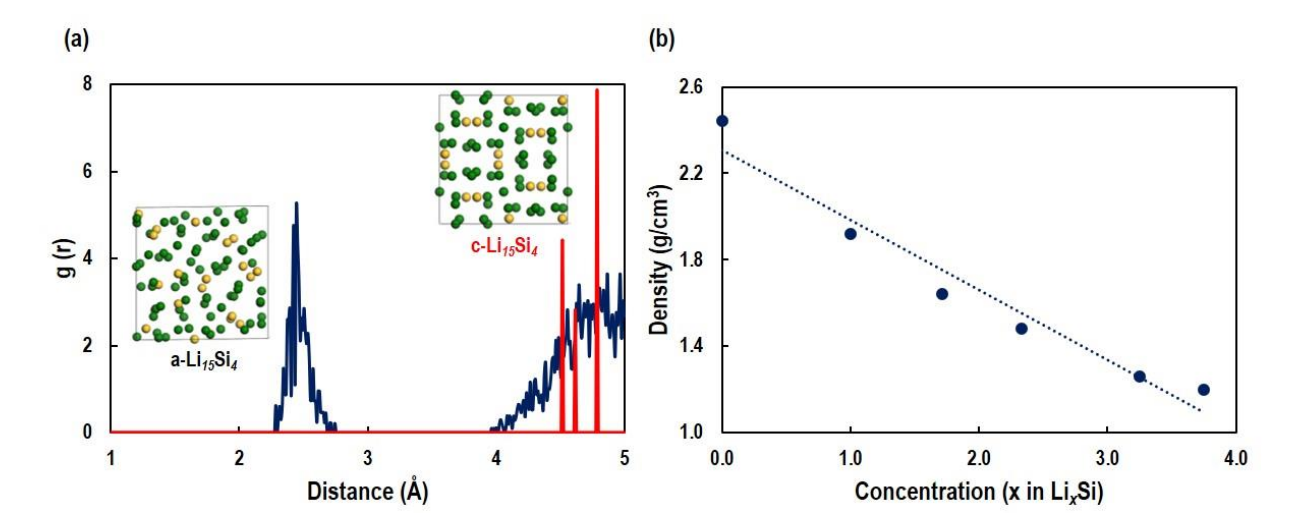


Figure 6-2 (a) Radial distribution function of c-Li₁₅Si₄ and a-Li₁₅Si₄ (b) Densities of a-Si, a-LiSi, a-Li₁₂Si₇, a-Li₁₂Si₃, a-Li₁₃Si₄, and a-Li₁₅Si₄ calculated from ReaxFF-NPT simulations via melting-and-quenching process

Linear fitting of the density as a function of x was obtained based on the densities calculated for representative concentrations and utilized to generate configurations at corresponding concentrations, as shown in **Fig. 6-2** (b). Each structure was generated with concentration interval of 0.1, resulting in 37 initial structures with concentration ranging from x = 0.1, 0.2, ..., 3.6, 3.75 which sufficiently cover the entire concentration range. The initial configurations were generated using random generation method in material studio with the number of Si varying at different concentrations. Total 50, 30, and 20 number of Si were used for the concentration range $x \le 1.0, 1.0 < x \le 2.0$, and $2.0 < x \le 3.75$ to ensure the total number of atoms were within ~ 150 atoms for efficient DFT calculations.

Once the initial configurations of a-Li_xSi at 37 concentrations were prepared, ReaxFF-MD simulations using NVT dynamics at high temperature (2500K) was performed for 10 ps to

completely melt the structure (**Fig. 6-1 Step 1**). Then, independent configurations were randomly chosen from the trajectory to generate liquid-like, near-ground-state, and intermediate a-Li_xSi structures (**Fig. 6-1 Step 2**). Amorphous Li_xSi structures were generated using AIMD and different optimization protocol. For AIMD, a $1\times1\times1$ K-point mesh and energy cutoff of 450 eV were employed to save enormous amount of computational time. Besides the K-point mesh and energy cutoff for AIMD, all the DFT calculation setups were kept identical to those used in the calculation of crystalline phases.

Liquid-like a-Li_xSi structures representing the highest energy state of the metastable a-Li_xSi were generated by following **Step 3-a** in **Fig. 6-1**. Twenty independent configurations from the high temperature MD trajectories for each concentration were obtained and DFT single-point energy calculation was performed to correlate the local structural motifs to the corresponding energies. Total 740 liquid-like configurations with corresponding energies were generated and incorporated into the database.

To obtain near-ground-state a-Li_xSi structures which represent the equilibrium state with the lowest energy, melting-and-quenching process were performed using AIMD (**Step 3-b** in **Fig. 6-1**). Five independent configurations from the high temperature AIMD trajectories for each concentration were chosen and each configuration was quenched to the room temperature at rapid rate of 300 K per 1000 MD time steps, where each MD timestep corresponded to 1.0 fs. Then the corresponding structures were relaxed with energy cutoff of 550 eV and atomic force tolerance of 0.02 eV/Å. To completely relax the structure and obtain near-ground-state structures, atomic coordinates, dimensions, and the shape of each structures was allowed to relax. Total 185 near-ground-state configurations with corresponding energies were generated and incorporated into the database.

Finally, to sample intermediate a-Li_xSi structures which covers the configurational space between the highest and lowest energy states, DFT relaxation with fixed volume were performed on the five independent structures obtained from the high temperature MD trajectories for each concentration (Step 3-c in Fig. 6-1). All the configurations and corresponding energies during the relaxation, which represent the local structural changes from high energy to low energy states, were collected and incorporated into the database (total 87270 structures). These structures will be critical if both energy and force will be fitted through machine learning.

6.2.3 Formation Energy and OCV for the Training Set

The formation energy is an important parameter to judge the stability of a compound, which can be determined by Gibb's free energy. In DFT calculation, the entropy and pressure contribution are negligible at T=0 K. Therefore, the Gibb's free energy can be approximated to be the total energy of a system calculated at T=0 K. In case of Li-Si alloys, the formation energy is defined as

$$E_f(x) = E_{Li_xSi} - (xE_{Li} + E_{Si})$$
 (6-1)

where x is the number of Li atoms per Si atom. E_f is the formation energy per Si (formula unit of Li_xSi) and E_{Li_xSi} is the total energy of the Li_xSi structure per Si (formula unit of Li_xSi). E_{Li} and E_{Si} are the energy of a single atom in the elemental body-centered cubic Li in elemental Si in a diamond lattice.

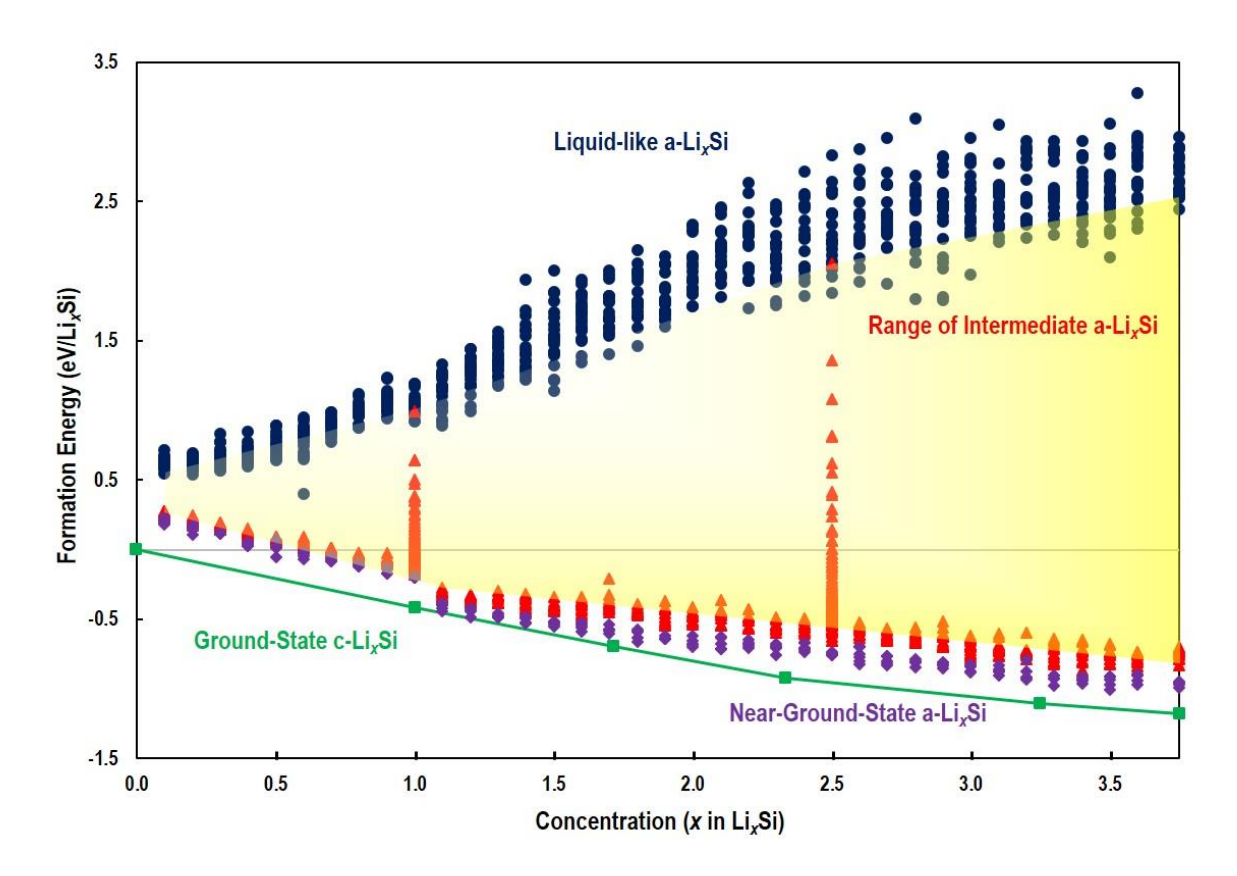


Figure 6-3 Formation energies of crystalline and amorphous Li_xSi included in the training set. The training set is consisted of total 88201 structures

The formation energies per Si atoms of the ground-state c-Li_xSi and metastable a-Li_xSi as a function of Li concentration are shown in **Fig. 6-3**. As expected, thermodynamically stable ground-state c-Li_xSi (green data points in **Fig. 6-3**) and liquid-like a-Li_xSi (blue data points in **Fig. 6-3**) have the lowest and highest formation energies, respectively. The formation energies of nearground-state a-Li_xSi (purple data points in **Fig. 6-3**) are lowest among the a-Li_xSi since they are the equilibrium structure for the metastable a-Li_xSi. Also, they agree well with the formation energies calculated from amorphous structures generated by different protocol, ^{52,147} which confirmed the protocol to generate equilibrium a-Li_xSi structure in this study successfully captures the local structural motifs and corresponding energies.

To further relate the energies to the experimental results, the OCV was computed using the following equation

$$V = -\frac{dE_f(x)}{dx} = -\frac{E(Li_{x_1}Si) - E(Li_{x_2}Si) - (x_1 - x_2) \cdot E(Li)}{(x_1 - x_2) \cdot F}, with \ x_1 > x_2$$
 (6-2)

where F is the Faraday's constant and $E(Li_xSi)$ is the formation energy obtained from DFT calculations at T = 0 K.

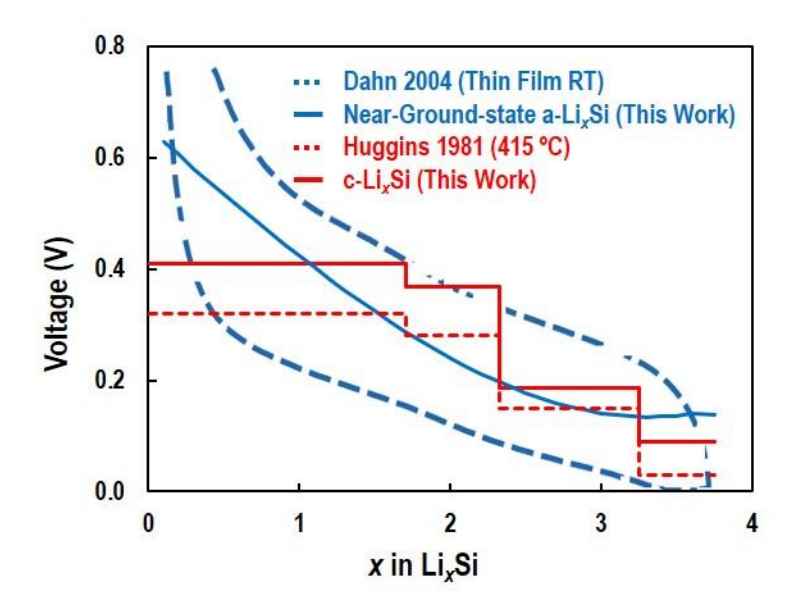


Figure 6-4 Experimental^{34,42} and calculated OCV vs. composition curves of Li/Si system at high temperature (lines in red) and room temperature (curves in blue) (Adapted from reference [³⁴]. Copyright © Journal of the Electrochemical Society 2004)

Fig. 6-4 represents the experimentally measured and computationally calculated OCV as a function of Li concentration (x) for crystalline Li $_x$ Si structures (red curve) and metastable nearground-state a-Li $_x$ Si (blue curve). Dotted red curve represents the experimentally measured OCV at high temperature and solid red curve represents the computationally calculated OCV in this study. Similarly, dotted blue curve represents the experimentally measure OCV upon electrochemical lithiation of a-Si and solid blue curve represents the computationally calculated

OCV from our near-ground-state a-Li_xSi structures. Both the computed voltage profile agrees well with the experimentally measured voltages, which confirms that the 0 K voltage profile is a reasonable approximation and the near-ground-state a-Li_xSi successfully represent the amorphous structures in equilibrium.

Finally, the red data points in **Fig. 6-3** represents the formation energies of the structure in between the high energy and near-ground-state a-Li_xSi. For clarity, the figure only shows the lowest formation energies at all concentrations and the relaxation string for concentration 1.0 and 2.5. The area in yellow represents the configurational space which the intermediate a-Li_xSi covers. From the plot, it is confirmed that our method covers all the possible configurational spaces (structural motifs) occurring at a-Li_xSi.

6.3 Elastic Property Calculation to Validate Machine Learning Results

In this section, the elastic properties were calculated for the near-ground-state a-Li_xSi structures, which will not be included in the training set but will be used to evaluate the accuracy of the machine learning potentials developed based on our training set provided in **Section 6.2** (currently working with Dr. Hirn's group to generate Li-Si potential through their machine learning techniques).

The elastic properties of a-Li_xSi are determined by computing the energetics of the deformed unit cells. Due to the isotropic nature of amorphous phases, different elastic constants can be deduced from the bulk modulus (B) and modulus C_{II} . Therefore, bulk modulus (B) and modulus C_{II} were first calculated and then used to calculate Shear Modulus and Young's Modulus. To calculate the bulk modulus, uniform tensile/compressive stress (ε , percentage) were applied on the a-Li_xSi alloys to achieve \pm 10 % volume variation. The relaxed energy of the deformed cells

were fitted to the equation $E(\varepsilon) = E_0 + a \varepsilon^2$, where E_0 is the energy of the undeformed cell. Then, bulk modulus was calculated using formula;

$$B = \frac{2a}{9V_0}$$
 (6-3)

where V_0 is the volume of the unstrained cell and a is the coefficient of ε^2 in the quadratic fit. Similarly, modulus C_{II} was calculated by imposing tensile/compressive stress (ε , percentage) on one orthogonal axe and computing the energies of the deformed configurations. The relaxed energy of the deform cells were fitted to the fit to the expression $E(\varepsilon) = E_0 + b \varepsilon^2$, modulus C_{II} was calculated by using formula

$$C_{11} = \frac{2b}{V_0} \tag{6-4}$$

Once the bulk modulus and modulus C_{II} was determined, Shear modulus and Young's modulus were then calculated using the expression;

Shear Modulus =
$$G = \frac{3(C_{11}-B)}{4}$$
 (6-5)

Young's Modulus = E =
$$\frac{9B(C_{11}-B)}{(C_{11}+3B)}$$
 (6-6)

Fig. 6-5 (b) represents the bulk modulus of c-Li_xSi and near-ground-state a-Li_xSi structures at five representative concentrations (a-LiSi, Li₂Si, Li₃Si, and Li_{3.75}Si) along with the computed bulk modulus taken from the literature.^{49,55} The bulk modulus of near-ground-state a-Li_xSi structures decreases linearly, which successfully capture the elastic softening of Li-Si phases with increasing Li concentration.⁵⁵

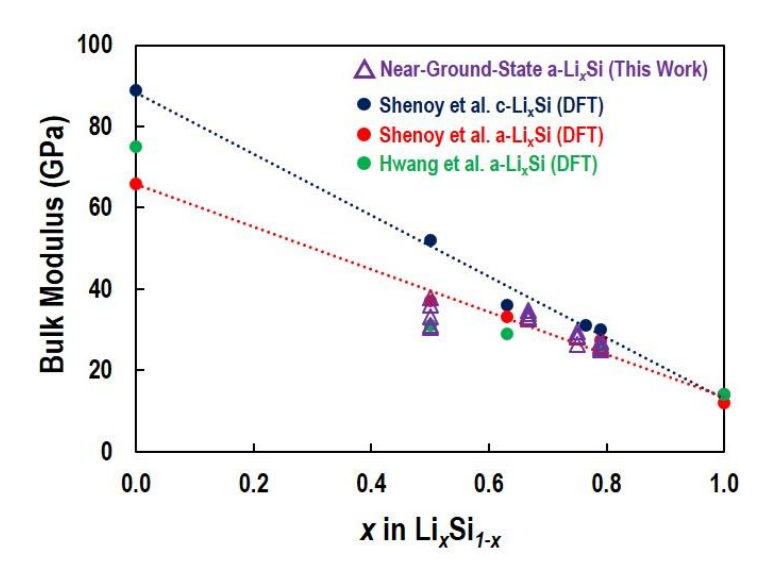


Figure 6-5 Bulk modulus for a-Li_xSi with comparison with literature (DFT)^{49,55}

Similarly, Shear modulus and Young's modulus of a-Si, a-LiSi, a-Li₂Si, a-Li₃Si, and a-Li_{3.75}Si were computed which agree well from the literature value.⁴⁹ Thus, the results further confirmed the training set generated in this work can successfully describe the elastic properties of Li-Si alloys. Such elastic information will be used to check the performance of the potentials developed using machine learning techniques, which is only fitted on the relationship between the structures and corresponding energetics.

6.4 Conclusions

In this study, I systematically developed an extensive training set of Li-Si alloys, which includes thermodynamically stable crystalline and metastable amorphous phases. Our methodology is based on a combination of ReaxFF-MD and first-principle DFT calculation through a FireWork work flow. To represent a wide range of structural motifs, Li-Si data base with concentration ranging from x = 0.1, 0.2, ..., 3.75 was classified in three categories based on their energy states. For the databased, 740 liquid-like a-Li_xSi structures at the highest energy and 185

near-ground-state a-Li_xSi structures at equilibrium was prepared. Also, 87270 intermediate structures in between the two extreme energy states were collected. I demonstrated that our training set successfully describe the metastable a-Li_xSi in different energy states which covers all the configurational space for Li-Si systems. The systematic method used herein is not limited to a specific material or amorphization mechanism and can be generally applied for simulating amorphous materials, which can be further utilized to develop machine learning potentials which can simulate materials with first-principle accuracy and force field efficiency.

The training set is currently used by Dr. Hirn's group to generate Li-Si potential through their machine learning techniques.

Chapter 7 Conclusions

In this thesis, atomic-scale MD simulations with Reactive force field were performed to obtain insights on the lithiation mechanism to accelerate the lithiation rate and elucidate the irreversible changes that are inherent at atomic-scale upon delithiation with rate effects. Also, the application of the reactive force field to the SiO_x system was investigated, which allowed us to better understand and design an extensive training set for force field development.

To elucidate the rate-limiting factor of lithiation, ReaxFF-based MD simulations to study the diffusion dynamics of both c-Si and a-Si were performed. The rate-limiting factor during lithiation of Si is the Si-Si bond breaking process and introducing Si vacancies exponentially increases the lithiation rate. Our results also revealed that Li diffusivity increases with concentration, which highlights the concentration dependent diffusion. Since the lithiation/delithiaiton capacity is directly related to the diffusivity and its dependence on Li concentration, the characteristic concentration dependent diffusion significantly contributes to the lithiation/delithiation hysteresis. These findings provide important insight into understanding the dynamics upon lithiation in Si anodes and suggest methods to enhance the lithiation rate, which knowledge can be utilized to design batteries with enhanced rate performance.

The irreversible changes that are inherent at atomic-scale upon delithiation with rate effects was studied by utilizing the self-developed ReaxFF-based MD delithiation algorithm with controlled delithiation rate, which represent non-equilibrium (fast) and near-equilibrium (slow) process. Fast delithiation led to the formation of dense Si network near the surface and nanoporosity inside the a-Li_xSi, resulting in 141 % volume dilation and significant amount of Li trapped inside (a-Li_{1,2}Si) at the end of delithiation process. In contrast, slow delithiation proceeds

with no permanent inner pore with nearly Li-free structure (a-Li_{0.2}Si) and minimal volume dilation (44 %). Regardless of the delithiation rate and existence of the trapped Li, continuous loss of the directly bonded Si-Si pairs caused the volume of the delithiated a-Li_xSi to be higher than the equilibrium structure with the same Li concentration, resulting in faster lithiation rate in the subsequent cycle. Based on the atomistic modeling and the quantified degradation mechanism, battery operating guidelines, including the delithiation rate and the depth of charge to avoid trapped Li and coating delamination, were suggested to improve the durability Si electrodes.

The application of the reactive force field used in our lithiation and delithiation simulation (Li/Si and Li/Al/Si/O/H system) to SiO_x system was evaluated by calculation and comparison of thermodynamic stability of SiO structures with DFT calculations. The formation energy of SiO respect to Si and SiO₂ was calculated to be a positive value for DFT calculations, whereas determined to be a negative value for ReaxFF calculations. Discrepancies between the thermodynamics stabilities originated from the training set of the ReaxFF, which only included various Si and SiO₂ phases. Since ReaxFF can only capture the configuration space described in the training set, I propose a guideline to extend of training set with metastable a-SiO_x phases to cover the composition range of SiO_x with $x=0 \sim 2$.

Based on the limitation on the transferability of the reactive force field, I designed and construct an accurate and extensive training set for Li-Si system well-suited for development of machine-learning potentials. First principle DFT calculation (Ab Initio MD quenching and optimization) were performed to generate training set with c-Li_xSi and a-Li_xSi with $x = 0 \sim 3.75$. The liquid-like a-Li_xSi structures at high temperature to ground-state a-Li_xSi were all included in the training set, covering the entire configurational space for metastable a-Li_xSi. The systematic strategy to construct an extensive training set can be further utilized to develop machine-learning

potential for different systems, which quality emulating the accuracy of the first-principle calculations and efficiency of the force fields.

APPENDIX

APPENDIX

Delithiation Algorithm

```
program track outer Si
implicit none
!! Parameters
!!!!!!!!!!NAME OF THE OUTPUT LAMMPS STRUCTURE FILE!!!!!!!!!!!!!!
character(len=*), parameter :: output file = "print"
integer, parameter :: frames = 51, bin no = 125, inner bin no=21, total types = 4, frame step=10
character(len=*), parameter :: input_trajectory = "MD.xyz" real, parameter :: Li_vacancy_conc = 0.100,c_x=50, c_y=50, c_z = 150 !Cell size
real, parameter :: band thickness = c z/bin no, init tolerance = 1.00 ! Angstroms
real, parameter :: percent_Al_used_for_buffer = .10
real, parameter :: percent Si used to average = .10
!NEW, 12/30/15
integer, parameter :: to_delete_from left = 100
integer, parameter :: to delete from right = 100
! define atom type
type :: atom
     character (len=2) :: name
         real :: x(frames), y(frames), z(frames)
         integer :: bin
         logical:: rflag = .false. , lflag = .false., remove=.false., middleSi= .false.
    integer :: type
end type
!Initialize
character(len=100) :: line1, line2
integer :: Li=0, Si=0, Al=0, Ox=0, Li_remove_run=0, Li_delcount = 0, removed_from_left=0
integer :: Ox_Al_l = 0, Ox_Al_r = 0, outer=0, L_Li=0, R_Li = 0, removed = 0, middle=0
real:: lmost = c z/2, rmost = c z/2, ave left = 0, ave right = 0, inner bin size real:: lmostSi = c z/2, rmostSi = c z/2, shell thickness, permanent bin size, perm L, perm R integer:: i=0, j=0, atom_number, rcount = 0, lcount = 0, Si_total=0
integer :: innerSi = 0, innerLi = 0, bin, outer_right=0, outer_left=0, Al_right=0, Al_left=0
integer :: Si count (frames, bin no), other count (frames, bin no), Li count (frames, bin no)
integer :: Si_count_inner(frames, inner_bin_no), Li_count_inner(frames, inner_bin_no) integer :: Si_count_inner_nochange(frames, inner_bin_no), Li_count_inner_nochange(frames,
inner bin no)
integer :: number_used, innerLi_last=0, number_used_2, dummy=0
real :: rightmost_Si = c_z / 2, leftmost_Si = c_z / 2, ave_L_L=0, ave_R_R=0, ave_L_R=0,ave_R_L=0
integer, allocatable, dimension(:) :: Li_left, Li_right
type(atom), allocatable, dimension(:):: atom array !New, 1/29/2016
real, allocatable, dimension(:) :: Al left shell, Al right shell, Si list
integer :: count_l=1,count_r=1
!character(len=*), parameter ::
path name="/mnt/research/msce/wortman5/Continuous Delithiation/2 19/"
!open files
open (unit=1, file=input_trajectory)
open (unit=3, file='Si band traj01.xyz')
open (unit=4, file='Si band traj02.xyz')
open (unit=6, file = "middleLi and ALL Si snapshot.xyz")
open(unit=7, file="Delithiated Snapshot.xyz")
open(unit=8,file="SI_LIST_TRACKER.txt")
open (unit=20, file="/mnt/home/kimkwa12/Delithiation/1D_Slab/MD/100/0.1ps/Si_band_width.txt",&
form="formatted", access="sequential", status="old", position="append")
open (unit=21, file="/mnt/home/kimkwa12/Delithiation/1D_Slab/MD/100/0.1ps/Si boundary left.txt",&
```

```
form="formatted", access="sequential", status="old", position="append")
open (unit=22,
file="/mnt/home/kimkwa12/Delithiation/1D Slab/MD/100/0.1ps/Si boundary right.txt", &
form="formatted", access="sequential", status="old", position="append")
open (unit=24, file="/mnt/home/kimkwa12/Delithiation/1D Slab/MD/100/0.1ps/inner Si number.txt",&
form="formatted", access="sequential", status="old", position="append")
open (unit=30, file="/mnt/home/kimkwa12/Delithiation/1D Slab/MD/100/0.1ps/Li deleted left.txt",&
form="formatted", access="sequential", status="old", position="append")
open (unit=31, file="/mnt/home/kimkwa12/Delithiation/1D Slab/MD/100/0.1ps/Li deleted right.txt",&
form="formatted", access="sequential", status="old", position="append")
open (unit=32, file="/mnt/home/kimkwa12/Delithiation/1D Slab/MD/100/0.1ps/Li deleted total.txt",&
form="formatted", access="sequential", status="old", position="append")
open (unit=33,
file="/mnt/home/kimkwa12/Delithiation/1D_Slab/MD/100/0.1ps/Li_deleted_from_shell_only.txt",&
form="formatted", access="sequential", status="old", position="append")
open (unit=40,
file="/mnt/home/kimkwa12/Delithiation/1D Slab/MD/100/0.1ps/Li remaining in left shell.txt",&
form="formatted", access="sequential", status="old", position="append")
file="/mnt/home/kimkwa12/Delithiation/1D Slab/MD/100/0.1ps/Li remaining in right shell.txt",&
form="formatted", access="sequential", status="old", position="append")
open (unit=50,
file="/mnt/home/kimkwa12/Delithiation/1D Slab/MD/100/0.1ps/bin ratios changingBinSize.txt",&
form="formatted", access="sequential", status="old", position="append")
open (unit=51,
file="/mnt/home/kimkwa12/Delithiation/1D Slab/MD/100/0.1ps/bin concentrations changingBinSize.txt
", &
form="formatted", access="sequential", status="old", position="append")
file="/mnt/home/kimkwa12/Delithiation/1D Slab/MD/100/0.1ps/bin ratios unchanging size.txt",&
form="formatted", access="sequential", status="old", position="append")
open (unit=53.
file="/mnt/home/kimkwa12/Delithiation/1D Slab/MD/100/0.1ps/bin concentrations unchanging size.txt
", &
form="formatted", access="sequential", status="old", position="append")
open (unit=60, file="/mnt/home/kimkwa12/Delithiation/1D Slab/MD/100/0.1ps/conc development.txt",&
form="formatted", access="sequential", status="old", position="append")
!NEW UNITS: 1/18
open (unit=70,
file="/mnt/home/kimkwa12/Delithiation/1D Slab/MD/100/0.1ps/Li deleted from outside left.txt",&
form="formatted", access="sequential", status="old", position="append")
open (unit=71,
file="/mnt/home/kimkwa12/Delithiation/1D Slab/MD/100/0.1ps/Li deleted from outside right.txt",&
form="formatted", access="sequential", status="old", position="append")
file="/mnt/home/kimkwa12/Delithiation/1D Slab/MD/100/0.1ps/Li deleted left TOTAL.txt",&
form="formatted", access="sequential", status="old", position="append")
```

```
open (unit=73,
file="/mnt/home/kimkwa12/Delithiation/1D Slab/MD/100/0.1ps/Li deleted right TOTAL.txt", &
form="formatted", access="sequential", status="old", position="append")
open (unit=80,
file="/mnt/home/kimkwa12/Delithiation/1D Slab/MD/100/0.1ps/X in LIXA1203 LEFT.txt",&
form="formatted", access="sequential", status="old", position="append")
file="/mnt/home/kimkwa12/Delithiation/1D Slab/MD/100/0.1ps/X in LIxAl203 RIGHT.txt",&
form="formatted", access="sequential", status="old", position="append")
open (unit=82,
file="/mnt/home/kimkwa12/Delithiation/1D Slab/MD/100/0.1ps/X in LIXA1203 AVERAGE.txt",&
form="formatted", access="sequential", status="old", position="append")
open (unit=83, file="/mnt/home/kimkwa12/Delithiation/1D Slab/MD/100/0.1ps/Left shell Li.txt",&
form="formatted", access="sequential", status="old", position="append")
open (unit=84, file="/mnt/home/kimkwa12/Delithiation/1D Slab/MD/100/0.1ps/Right shell Li.txt",&
form="formatted", access="sequential", status="old", position="append")
open (unit=90, file="/mnt/home/kimkwa12/Delithiation/1D Slab/MD/100/0.1ps/inner Li.txt",&
form="formatted", access="sequential", status="old", position="append")
open (unit=100, file="/mnt/home/kimkwa12/Delithiation/1D Slab/MD/100/0.1ps/inner bin size.txt",&
form="formatted", access="sequential", status="old", position="append")
open (unit=101.
file="/mnt/home/kimkwa12/Delithiation/1D_Slab/MD/100/0.1ps/Si_bin_to_Si_total.txt",&
form="formatted", access="sequential", status="old", position="append")
open (unit=102,
file="/mnt/home/kimkwa12/Delithiation/1D Slab/MD/100/0.1ps/Li bin to Li total.txt",&
form="formatted", access="sequential", status="old", position="append")
open (unit=103.
file="/mnt/home/kimkwa12/Delithiation/1D Slab/MD/100/0.1ps/outermost Si width.txt",&
form="formatted", access="sequential", status="old", position="append")
do i = 1, frames
    do j = 1, bin no
        Si_count(\bar{i},j) = 0
        Li\_count(i,j) = 0
        other count(i,j) = 0
    end do
    do j=1, inner bin no
        Si count \overline{i}nner(i, j)=0
        Li_count_inner(i,j)=0
        Si_count_inner_nochange(i, j)=0
Li_count_inner_nochange(i,j)=0
    end do
end do
read(1,*) atom_number
allocate(atom array(atom number))
read(1,*)
! find the rightmost and leftmost atoms
do i = 1, atom number
    read(1,*) atom array(i)%name, atom array(i)%x(1), &
```

```
atom_array(i)%y(1), atom_array(i)%z(1)
    bin = int(atom_array(i)\sqrt[8]{z}(1) / (c z / bin no)) + 1
    if (bin>bin no) then
      bin=bin no
    else if (bin<=0) then
      bin=0
    end if
    if (atom array(i)%name == "Si") then
        Si\_count(1, bin) = Si\_count(1, bin) + 1
        Si total=Si total+1
    atom array(i)%type = 4
    else if (atom array(i)%name == "O") then
    other count (1, bin) = other count (1, bin) + 1
        atom_array(i)%type = 3
    else if ( atom array(i)%name == "Al") then
        other_count(1,bin) = other_count(1,bin) + 1
        atom array(i)%type = 1
        if (atom array(i) %z(1)>c z/2) then
          Al right=Al right+1
        else
          Al_left=Al left+1
        end if
    else
    Li count (1, bin) = Li count (1, bin) + 1
    atom array(i)%type = 2
    end if
end do
!call write bin conc(1)
allocate(Si_list(Si_total))
Si total=0
do i=1, atom number
  if (atom array(i)%name=="Si") then
   Si list(Si total+1) = atom array(i)%z(1)
   Si total=Si total+1
  end if
end do
 ! find the left and right-most at this timestep
call update left right(1)
  write(20,*)
              rightmost Si-leftmost Si
  write(21,*) leftmost Si
  write(22,*) rightmost Si
allocate (Al right shell (Al right))
allocate (Al left shell (Al left))
Si total=0
!decide if each atom starts within a certain distance of the rmost or lmost
do i = 1, atom number
  if ( leftmost Si + band thickness > atom array(i)%z(1) &
   .and. atom array(i)%z(1) > leftmost Si) then
    if (atom\_array(i) %name == "Si" .and. atom\_array(i) %z(1) > 0) then
      atom_array(i)%lflag = .true.
      lcount = lcount + 1
    end if
  else if ( rightmost Si - band thickness < atom array(i)%z(1) &
    .and. atom array(i)%z(1) < rightmost Si) then
    if (atom array(i) %name == "Si" .and. atom_array(i) %z(1) < c_z) then
      atom array(i)%rflag = .true.
      rcount = rcount + 1
    end if
```

```
else if ( atom array(i)%z(1) > leftmost Si .and. atom array(i)%z(1) < rightmost Si) then
        if (atom array(i) %name == "Si" .and. atom array(i) %z(1) < c z) then
             atom array(i)%middleSi = .true.
             middle = middle + 1
        end if
  end if
end do
do i = 1, bin no
    Si_count(1, i) = 0
    \text{Li count}(1,i) = 0
    other count (1,i) = 0
end do
permanent_bin_size = 1.0*(rightmost_Si-leftmost_Si)/ inner_bin_no
perm L=leftmost Si
perm_R=rightmost_Si
rewind(unit=1)
!write the 2 xyz files
do j = 1, frames
  Si total=0
read(1,*)
read(1,'(a)') line1
write(3,'(i5)') lcount
write(3,*) line1
write (4, '(i5)') rcount
write(4,*) line1
!write(6,'(i5)') middle
!write(6,*) line1
inner_bin_size = (rightmost_Si-leftmost_Si) / inner_bin_no
write(100,*) inner bin size
Al left=0
Al_right=0
do i = 1, atom_number
  read(1,*) atom array(i)%name, atom array(i)%x(j), &
  atom array(i)%y(j), atom array(i)%z(j)
 bin = int(atom_array(i) %z(j) / (c_z / bin_no)) + 1
  if (bin \le 0) then
  bin = 0
  else if (bin>=bin no) then
  bin = bin_no
  end if
  if (atom array(i)%name == "Si") then
      Si_{count(j, bin)} = Si_{count(j, bin)} + 1
  else if (atom array(i)%name == "O" .or. atom array(i)%name == "Al") then
      other count(j,bin) = other count(j,bin) + 1
      Li count(j,bin) = Li count(j,bin) + 1
  end if
  if (atom_array(i)%z(j) > leftmost_Si .and. atom_array(i)%z(j)<rightmost_Si) then
      bin = int(((atom_array(i)%z(j) - leftmost_Si)/ inner bin_size) + 1)
    if (atom array(i)%name == "Si") then
      innerSi = innerSi + 1
      Si count_inner(j, bin)=Si_count_inner(j, bin)+1
    else if (atom array(i) % name == "Li") then
      innerLi = innerLi + 1
```

```
Li count inner(j, bin)=Li count inner(j, bin)+1
  end if
end if
if (atom\_array(i) %z(j) > perm\_L .and. atom\_array(i) %z(j) < perm\_R) then
    bin = int(((atom array(i)%z(j) - perm L)/ permanent bin size) + 1)
  if (atom_array(i)%name == "Si") then
    Si_count_inner_nochange(j, bin)=Si_count_inner_nochange(j, bin)+1
  else if (atom_array(i)%name == "Li") then
   Li count inner nochange(j, bin)=Li count inner nochange(j, bin)+1
  end if
end if
if (atom array(i)%name=="Al") then
  if (atom array(i) %z(j) > (c z/2)) then
    if (Al_right<size(Al_right_shell)) then
        Al_right=Al_right+1
        Al right=size(Al right shell)-1
    end if
   Al_right_shell(Al_right) = atom_array(i)%z(j)!before, had Al right+1
    if (Al left<size(Al left shell)) then
        Al left=Al left+1
    else
        Al left=size(Al left_shell)-1
        Al left shell(Al left) = atom array(i)%z(j)
      end if
    end if
  end do
do i=1, atom number
  if (atom array(i)%name=="Si") then
    Si list(Si total+1)=0
    Si list(Si total+1) = atom array(i) % z(j)
   Si_total=Si_total+1
  end if
end do
  call sort(Si list, Si total)
  !number used=Si total*percent Si used to average
  leftmost_Si=sum(Si_list(1:50))/(50)
  !number used=(Si total-(Si total*percent Si used to average))
  !number used 2=Si total-1
  rightmost Si=sum(Si list(1563:1612))/(50)
 call sort(Al_left_shell,Al_left)
  call sort (Al right shell, Al right)
  ave L R=0
 ave L L=0
 ave R L=0
 ave R R=0
  !define the shell boundaries based on aluminum
!number used=(Al left*(1-percent Al used for buffer))
ave_L_R=sum(Al_left_shell(911:Al_left))/50
!number_used=Al_right*percent_Al_used_for_buffer
ave R L=sum(Al right shell(1:50))/50
```

```
!number used=Al left*percent Al used for buffer
ave L L=sum(Al left shell(1:10))/10
!number used=Al right*(1-percent Al used for buffer)
ave R R=sum(Al right shell(951:Al right))/(10)
write(8,*) ave_L_L, ave_L_R, ave_R_L, ave_R_R
  do i=1, atom number
    if (atom_array(i)%name=="Li") then
      if (atom array(i)%z(j)>ave L L .and. atom array(i)%z(j)<ave L R ) then
        L Li=L Li+1
      else if (atom_array(i) %z(j) > ave_R_L .and. atom_array(i) %z(j) < ave_R_R ) then
        R Li=R Li+1
      end if
    end if
  end do
  !write(80,*) L Li*2.0/(Al left*(1-percent Al used for buffer))!left
  write(80,*) L Li*2.0/(960)
  !write(81,*) R_Li*2.0/(Al_right*(1-percent_Al_used_for_buffer))!right
  write(81,*) R_Li*2.0/(960)
  !write(82,*)
  1.0*((L Li*2.0/(Al left*(1-percent Al used for buffer)))+(R Li*2.0/(Al right*(1-percent Al used
   for_buffer))))/2
  write(82,*) 1.0*((L Li*2.0/960)+(R Li*2.0/960))/2
  write(83,*) L Li
  write(84,*) R_Li
  L Li=0
  R Li=0
  call write conc()
  write(20,*) rightmost Si-leftmost Si
  write(21,*) leftmost_Si
write(22,*) rightmost_Si
  write(103,*) Si list(Si total)-Si list(1)
  do i=1,Si total
    Si list(i) = 0
  end do
end do !End of main do loop for each frame
j=frames
write(6,*) Si_total+innerLi_last-1
write(6,*) "Atoms. Timestep:0"
do i=1, atom number
  if (atom_array(i)%name=="Si") then
      write(6,"(a)",advance="no") atom_array(i)%name
write(6,"(4f11.6)") atom_array(i)%x(j), &
      atom_array(i)%y(j), atom_array(i)%z(j)
  else if (atom_array(i)%name=="Li") then
      if (atom array(i)%z(j)>=leftmost Si .and. atom array(i)%z(j)<=rightmost Si) then
        write(6,"(a)",advance="no") atom array(i)%name
        write(6,"(4f11.6)") atom_array(i)%x(j), &
        atom_array(i)%y(j), atom_array(i)%z(j)
  end if
end do
! Write data for concentration profile. Set frame step in parameters
do j = 1, frames, frame_step
    call write bin conc(j)
end do
```

```
j=frames
open(2, file = output file, status = "replace")
call init random seed()
do i = 1, atom number + 2
   backspace(unit=1) ! This line should put you right where you need to be in the file,
   whether it's XYZ or trajectory file
end do
read(1,"(a)") line1
read(1,"(a)") line2
do i = 1, atom number
   if (atom_array(i)%name == "Li") then
       Li = Li + 1
   else if (atom_array(i)%name == "Si") then
       Si = Si + 1
       call check left right()
   else if (atom_array(i)%name == "Al") then
       Al = Al + 1
       call check left right()
   else if (atom_array(i)%name == "O") then
       Ox = Ox + 1
       call check left right()
   end if
end do
call find Si bounds()
ave right = ave right / Ox Al r
ave left = ave left / Ox Al l
!shell thickness = 1.0 * (ave right -rmostSi)
allocate(Li_left(atom_number))
allocate(Li right(atom number))
do i = 1, atom_number
 Li left(i) = 0
 Li right(i) = 0
 if (atom array(i)%name == "Li") then
   if (atom array(i)%z(j) > ave R R ) then
           outer right=outer right+1
           outer = outer + 1
           atom array(i)%remove = .true.
   else if (atom\_array(i)%z(j) < ave\_L\_L) then
           outer left=outer left+1
           outer = outer + 1
           atom_array(i)%remove = .true.
   end if
 else if (atom_array(i)%name == "Al") then
   if (atom array(i) %z(j) > c z/2) then
       !Al_right=Al_right+1
   else
       !Al left=Al left+1
   end if
 end if
end do
!do i=1,atom number
! if (atom array(i)%name =="Al") then
 ! if (atom array(i) %z(j) > c z/2) then
```

```
Al right_shell(count_r) = atom_array(i)%z(j)
      count r=count r+1
        else
    ! Al left shell(count_l) = atom_array(i)%z(j)
    ! count l=count l+1
  !end if
!end do
call sort(Al right shell, Al right)!before, was count r-1
call sort (Al left shell, Al left)
ave left=0
ave right=0
!number used=(Al left*(1-percent Al used for buffer))
do i=Al left, 50, -1
  ave_left=ave_left+Al_left_shell(i)
ave left=ave left/(50)
!number used=Al right*percent Al used for buffer
do i=1,50
 ave right=ave right+Al right shell(i)
end do
ave_right=ave_right/(50)
call Li track()
write(70,*) outer_left
write(71,*) outer right
!This method will mark a certain number of Li atoms by "remove = .true."
!NEW 1/18/16: Adjust the number deleted based on how many have already been deleted from
left/right outer portions
call shuffle pick(Li left, L Li, to delete from left - outer left )
write(30, '(a)', advance="yes")
removed from left=Li remove run
write(30,'(5i5)',advance="no") Li remove run
write(72,*) Li_remove_run + outer_left
call shuffle pick(Li right, R Li, to delete from right - outer right)
write(31,'(5i5)',advance="yes") Li remove run
write(73,*) Li remove run + outer right
write (33, '(5i5)', advance="no") Li remove run + removed from left
write(32,'(5i5)',advance="yes")Li remove run + removed from left+outer right+outer left
write (40,*) L Li - removed from left
write(41,*) R_Li - Li_remove_run
if (Al_left > 0) then
    write(80,*) 1.0*(L Li - removed from left) * 2 / (Al left)
else
    write(80,*) "No Al found: Division by 0"
end if
if (Al right > 0) then
    write(81,*) 1.0*(R Li - Li remove run) * 2 / (Al right)
    write (81, *) "No Al found: Division by 0"
end if
```

```
do i = 1, atom number
    if (atom array(i)%remove) then
           Li delcount = Li delcount + 1
    end if
end do
!write(2,*) Li delcount
!write(3,*) "Total # of Li deleted:", Li delcount
!!!! Write the output file!
write(2,*) "LAMMPS data file. CGCMM style. atom_style charge generated by VMD/TopoTools v1.5 on
Tue Jul 28 15:06:41 -0400 2015"
write(2,*) atom number - (Li delcount), " atoms"
write(2,*) "0 bonds"
write(2,*) "0 angles"
write(2,*) "0 dihedrals"
write(2,*) "0 impropers"
write(2,*) total_types," atom types"
write(2,*) "0 bond types"
write(2,*) "0 angle types"
write(2,*) "0 dihedral types"
write(2,*) "0 improper types"
write(2,*) "0.00000", c_x, " xlo xhi" write(2,*) "0.00000", c_y, " ylo yhi"
write(2,*) "0.00000", c z, " zlo zhi"
write (2, *)
write(2,*) "# Pair Coeffs"
write(2,*) "#"
write(2,*) "# 1 Al"
write(2,*) "# 2 Li"
write(2,*) "# 3 0"
write(2,*) "# 4 Si"
write(2,*)
write(2,*) "Masses"
write(2,*)
write(2,*) "1 26.981539 # Al"
write(2,*) "2 6.9410000 # Li"
write(2,*) "3 15.999999 # 0"
write(2,*) "4 28.085500 # Si"
write(2,*)
write(2,*) "Atoms"
write(2,*)
write(7,*) atom_number - Li_delcount
write(7,*) "Atoms. Timestep=0"
do i = 1, atom number
    if (.not. atom array(i)%remove) then
        write(2,"(2i5)",advance="no") i-removed, atom array(i)%type
         write(2,"(4f11.6)",advance="no") 0.000000, atom array(i)%x(j), &
        atom_array(i)%y(j), atom_array(i)%z(j)
        write(2,*) " # ", atom_array(i)%name
        write(7,*) atom_array(i)%name, atom_array(i)%x(j), atom_array(i)%y(j),
        atom array(i)%z(j)
    else
        removed = removed + 1
            end if
end do
deallocate (atom array)
deallocate (Li right)
deallocate (Li left)
deallocate (Al_left_shell)
deallocate (Al right shell)
```

```
deallocate (Si list)
contains
subroutine write conc()
    write(60,*) innerLi*1.0 / (innerSi)
    write(90,*) innerLi
    write(24,*) innerSi
    if (j==frames) then
      innerLi last=innerLi
    end if
    innerSi = 0
    innerLi = 0
end subroutine write conc
subroutine write bin conc(frame)
    implicit none
    integer :: frame
    !write(51,"(1i5)",advance="no") frame
    !write(50,"(1i5)",advance="no") frame
    !write(52, "(115)", advance="no") frame
    !write(53,"(115)",advance="no") frame
    !Note: each column is a bin
    ! Each row is a timestep:
    ! Ex:
    ! Bin 1 Time 1, Bin 2 Time 1, Bin 3 Time 1
    ! Bin 1 Time 2, Bin 2 Time 2, etc
    do i=1, inner bin no
        if (Si_count_inner(frame,i)>0) then
        write (\overline{50},"(2\overline{0}f11.6)",advance="no") Li count inner(frame, i) * 1.0 /
        Si count inner(frame, i)
        else
          write(50,*) "Infinity:no Si in this bin"
        write(51,"(20f11.6)",advance="no") Li count inner(frame, i) * &
        1.0 / (Si count inner(frame, i)+Li count inner(frame, i))
        if (Si count inner nochange(frame, i) > 0) then
        write (\overline{52},"(2\overline{0}f11.6)",advance="no") Li count inner nochange (frame, i) * &
        1.0 / Si count inner nochange(frame, i)
        else
          write(52,*) "Infinity:no Si in this bin"
        write(53,"(20f11.6)",advance="no") Li_count_inner_nochange(frame, i) * &
        1.0 / (Si_count_inner_nochange(frame, i)+Li_count_inner_nochange(frame, i))
        write(101, "(20f11.6)", advance="no") 1.0*Si count inner(frame,
        i)/sum(Si_count_inner(frame, 1:inner_bin_no))
        write (102, "(20f11.6)", advance="no") \overline{1.0}*Li count inner (frame,
        i)/sum(Li count inner(frame, 1:inner bin no))
    end do
        write(50, *)
        write(51,*)
        write(52,*)
        write(53,*)
        write(101,*)
        write(102,*)
    end subroutine write bin conc
    subroutine update left right(t)
      implicit none
      integer :: t, arb
      real :: 1 sum=0, r sum=0
        rcount=Si total*percent Si used to average
```

```
lcount=Si total*percent Si used to average
    call sort (Si list, Si total)
    do i=1, lcount
      l_sum=l_sum+Si_list(i)
    end do
    arb=Si total-rcount
    do i=Si total, arb,-1
     r_sum=r_sum+Si_list(i)
    end do
    rightmost Si = r sum / rcount ! find the average
    leftmost \overline{Si} = 1 \overline{sum} / lcount
    1 \text{ sum} = \overline{0}
    r_sum = 0
    !rightmost Si=(c z/2)+2
    !leftmost \overline{Si} = (c \overline{z}/2) - 2
end subroutine update_left_right
subroutine shuffle_pick(in_list, non_zero, amount)
! Each Li in the right or left shells has their own integer value (1st, 2nd,etc)
! in list is a list containing either 0 or the integer value of a "shell" lithium (could be
right or left)
! Non-zero is an integer count of how many non-zero elements should be in "in list"
! amount is the total number of vacancies to be generated
    implicit none
    integer :: i, position, temporary=1, amount, non zero
    integer :: in list(:)
    integer, dimension(non zero) :: list
    real :: rand
    do i= 1, size(list)
      list(i) = 0
    end do
    Li remove run = 0
    if (amount>non zero) then
        amount=non zero
    end if
    temporary = 1
    do i = 1, size(in_list)
      if (in_list(i) \overline{/}= 0) then
        list(temporary) = in list(i)
        temporary = temporary + 1
      end if
    end do
    do i = size(list), 1, -1
                                   ! this part shuffles the list
      call random number (rand)
      position = \overline{int}(rand*i + 1)
      temporary = list(position)
      list(position) = list(i)
      list(i) = temporary
    end do
    Li_remove_run=0
    i=\overline{0}
    do
        if (list(i) /= 0) then
```

```
if (.not. atom_array(list(i))%remove) then
                 Li_remove_run = Li_remove_run + 1
                 atom_array(list(i))%remove = .true.
                 if (\overline{Li}_{remove}_{run} >= amount) then
                     exit
                 end if
            end if
        end if
    end do
    dummy=0
    do i=1, atom number
      if (atom array(i)%remove) then
        dummy=dummy+1
      end if
    end do
    write(8,*) "Li marked to be removed total:", dummy
end subroutine shuffle pick
subroutine check left right()
    if (atom array(i)%name /= "Li") then ! if it's NOT a Li
        if (atom array(i)%z(j) > rmost ) then
            \verb|rmost| = \verb|atom_array(i)| % \verb|z(j)|! | this is the rightmost overall atom (excluding Li)|
        else if (atom array(i) %z(j) < lmost) then
            lmost = atom_array(i)%z(j)
        end if
        end if
    if ( atom array(i)%name == "Al" ) then
        if (atom\_array(i)%z(j) > c\_z/2) then
            ave right = ave right + atom array(i)%z(j)
            Ox_Al_r = Ox_Al_r + 1
                else
            ave left = ave left + atom array(i)%z(j)
            Ox \overline{A}1 1 = Ox \overline{A}1 1 + 1
        end if
    end if
end subroutine check left right
subroutine Li track() ! This keeps track of the "index" of all the Li atoms within the "shell
region" in an array
                       ! It also keeps an integer count of the total number in each one of these
                       shells
    do i = 1, atom number
        if (atom_array(i)%name=="Li") then
             if (atom array(i)%z(j)>ave L L .and. atom array(i)%z(j)<ave L R ) then
                 \text{Li left(i)} = i
                 L Li=L Li+1
            else \overline{i}f (a\overline{t}om array(i)%z(j)>ave R L .and. atom array(i)%z(j)<ave R R ) then
                R Li=R Li+1
                 Li right(i) = i
            end if
    end if
end subroutine Li track
subroutine find Si bounds() ! Find the leftmost and rightmost Si according to some criteria
    logical :: in region = .false.
    do i = 1, int(bin no / 2)
        if (Si count(j,i) > 5) then
            lmostSi = 1.0 * (i-1) * (c_z / bin_no )
```

```
exit
        end if
   end do
   do i = int(bin_no / 2), bin_no
       if (Si_count(j,i) > 5) then
           in region = .true.
        else \overline{if} (in region .and. Si count(j,i) < 5) then
           rmostSi = 1.0 * (i-2) * (c_z / bin_no)
            in region = .false.
           exit
        end if
    end do
end subroutine find Si bounds
subroutine init random seed() ! Calls to the clock to get a true random seed
      INTEGER :: i, n, clock
     INTEGER, DIMENSION(:), ALLOCATABLE :: seed
     CALL RANDOM SEED (size = n)
     ALLOCATE (seed(n))
     CALL SYSTEM CLOCK (COUNT=clock)
      seed = clock + 37 * (/ (i - 1, i = 1, n) /)
     CALL RANDOM SEED (PUT = seed)
     DEALLOCATE (seed)
end subroutine init random seed
INTEGER FUNCTION FindMinimum(x, Start, End)
     IMPLICIT NONE
     REAL, DIMENSION(1:), INTENT(IN) :: x
     INTEGER, INTENT(IN)
                                        :: Start, End
     Real
                                        :: Minimum
     INTEGER
                                        :: Location
     INTEGER
                                        :: i
                                 ! assume the first is the min
     Minimum = x(Start)
     Location = Start
                                  ! record its position
     DO i = Start+1, End ! start with next elements
        IF (x(i) < Minimum) THEN ! if x(i) less than the min?
           Minimum = x(i)!
                                       Yes, a new minimum found
           Location = i
                                       !
                                             record its position
        END IF
     END DO
     FindMinimum = Location
                                     ! return the position
END FUNCTION FindMinimum
SUBROUTINE Swap(a, b)
     IMPLICIT NONE
     REAL, INTENT(INOUT) :: a, b
                         :: Temp
     Temp = a
     a = b
        = Temp
     b
  END SUBROUTINE Swap
SUBROUTINE sort(x, Size)
     IMPLICIT NONE
      real, DIMENSION(1:), INTENT(INOUT) :: x
      INTEGER, INTENT(IN)
                                           :: Size
      INTEGER
                                           :: i
     INTEGER
                                           :: Location
```

```
DO i = 1, Size-1 ! except for the last
Location = FindMinimum(x, i, Size) ! find min from this to last
CALL Swap(x(i), x(Location)) ! swap this and the minimum
END DO
END SUBROUTINE Sort
end program track_outer_Si
```

Firework Codes (Generation of Automated Training Set)

Global Setting

```
%% This file sets all parameters needed in the whole workflow
%% Generate lammps job
structureDir = 'originalStructures/';
lammpsSampleDir = 'lammpsJob/';
minimization = 1;
eqStep = 10000;
trajInterval = 50;
eqTemperature = 2500;
lparam = ' ';
nnodes1 = 2;
ppnode1 = 7;
walltime1 = '03:59:59, feature=intel16, mem=10gb';
parentDir = '/mnt/home/kimkwa12/SPG/AutomaticTrainingSet/';
%% Extract structures from lammps job
NSample = 5;
workingDir = '/mnt/home/kimkwa12/SPG/AutomaticTrainingSet/';
trainingSetDir = '/mnt/home/kimkwa12/SPG/AutomaticTrainingSet/trainingSet/';
atomName = 'Si Li';
%% Generate VASP job
E cutoff = 550;
VASPStructureDir = 'trainingSet/';
VASPSampleDir = 'VASPJob/';
lparam2 = ' ';
nnodes2 = 2;
ppnode2 = 14;
walltime2 = '96:00:00, feature=intel16, mem=80gb';
parentDir2 = '/mnt/home/kimkwa12/SPG/AutomaticTrainingSet/';
%% Extract energy and add to info file
%% Add matlab functions
path(path,[parentDir '/matlabLibs'])
```

Generate Firework Jobs

```
%% Generate firework input files from originalStructures
응응
clear;
% load settings
globalSettings
nStart = 1;
% read structures
% Read all structures
structureList = dir(structureDir);
fwFile = 'fws:';
% add "generate lammps job" task
fwFile = char(fwFile,...
    ['- fw id: ' num2str(nStart)],...
    ' name: GenerateLammpsJob',...
      spec:',...
    [ '
          launch dir: ' parentDir],...
          tasks:',...
          _fw_name: ScriptTask',...
           script: bash generateLammpsJob.sh');
nStep1 = nStart;
% add lammps job tasks
nStart = nStart + 1;
for i = 3:size(structureList,1)
    currentFileName = structureList(i).name;
    if(~strcmp(currentFileName(end-3:end),'data'))
    end
    folderName = [currentFileName(1:end-5) '-lammps'];
    fwFile = char(fwFile,...
        ['- fw id: ' num2str(nStart)],...
        [' name: ' folderName],...
           spec:',...
               launch dir: ' parentDir folderName],...
             tasks:',...
             - _fw_name: ScriptTask',...
               script: bash lammpsJob.qsub',...
             queueadapter:',...
              walltime: 'walltime1],...
        [ '
                nnodes: ' num2str(nnodes1)],...
        [ '
                ppnode: ' num2str(ppnode1)]);
    nStart = nStart + 1;
end
% add "generate vasp job" task
fwFile = char(fwFile,...
    ['- fw id: ' num2str(nStart)],...
    ' name: extractStructuresFromLammpsJob',...
       spec:',...
    [ '
           launch dir: 'parentDir],...
         tasks:',...
         - fw name: ScriptTask',...
           script: bash extractStructuresFromLammpsJob.sh');
nStep2 = nStart;
nStart = nStart + 1;
fwFile = char(fwFile,...
    ['- fw id: ' num2str(nStart)],...
      name: GenerateVASPJob',...
       spec:',...
          _launch_dir: ' parentDir],...
          tasks:',...
         - fw name: ScriptTask',...
           script: bash generateVaspJob.sh');
nStep3 = nStart;
```

```
nStart = nStart + 1;
% add vasp job task
for i = 3:size(structureList,1)
     currentFileName = structureList(i).name;
    if(~strcmp(currentFileName(end-3:end),'data'))
         continue
    end
     for j = 1:NSample
         folderName = [currentFileName(1:end-5) '-' num2str(j) '-vasp'];
         fwFile = char(fwFile,...
             ['- fw_id: ' num2str(nStart)],...
[' name: ' folderName],...
' spec:',...
             [ '
                   launch dir: ' parentDir folderName],...
                   tasks:',...
                   fw name: ScriptTask',...
                    script: bash vaspJob.qsub',...
                  queueadapter:',...
             [ '
                     walltime: 'walltime2],...
                     nnodes: ' num2str(nnodes2)],...
             [ '
                     ppnode: ' num2str(ppnode2)]);
             [ '
         nStart = nStart + 1;
         end
end
nStep4 = nStart;
% add "generate vasp job" task
fwFile = char(fwFile,...
     ['- fw id: ' num2str(nStart)],...
      name: extractEnergyFromVaspJob',...
       spec:',...
           launch dir: 'parentDir],...
          _tasks:',...
          - _fw_name: ScriptTask',...
            script: bash extractEnergyFromVaspJob.sh');
nStart = nStart + 1;
 % add links and metadata
fwFile = char(fwFile,...
     'links:',...
     [' ' num2str(nStep1) ':']);
 % step1 - g lammps -> run lammps
for i = (nStep1 + 1): (nStep2 - 1)
     fwFile = char(fwFile,...
     [' - ' num2str(i)]);
end
 % step2 run lammps -> g vasp
 for i = (nStep1 + 1): (nStep2 - 1)
    fwFile = char(fwFile,...
     [' ' num2str(i) ':'],...
[' - ' num2str(nStep2)]);
 end
 fwFile = char(fwFile,...
     [' ' num2str(nStep2) ':'],...
     [' - ' num2str(nStep3)]);
% step3 g vasp -> run vasp
fwFile = char(fwFile,...
    [' ' num2str(nStep3) ':']);
for i = (nStep3 + 1): (nStep4 - 1)
   fwFile = char(fwFile,...
    [' - ' num2str(i)]);
```

```
end
% step4 collect data
for i = (nStep3 + 1):(nStep4 - 1)
    fwFile = char(fwFile,...
    [' ' num2str(i) ':'],...
    [' - ' num2str(nStep4)]);
end

fwFile = char(fwFile,...
    'metadata: {}');
% write fw file
writeList('trainingSet.yaml',fwFile);
if(~strcmp(computer,'PCWIN64'))
    exit;
end
```

Generate LAMMPS Job

```
%% Generate the lammps eq job from a structure file
900
clear;
% Load settings
globalSettings
% Pre-process
if (minimization)
    miniStr = 'minimize 1e-7 1e-7 5000 10000';
else
    miniStr = '# minimize 1e-7 1e-7 5000 10000';
end
% Read all structures
structureList = dir(structureDir);
for i = 3:size(structureList,1)
    currentFileName = structureList(i).name;
    if(~strcmp(currentFileName(end-3:end),'data'))
        continue
    end
    folderName = [currentFileName(1:end-5) '-lammps'];
    % For each structure, create seperate folder and copy files
```

128

```
[SUCCESS, MESSAGE, MESSAGEID] = mkdir(folderName);
    if (SUCCESS ~= 1)
        disp(['Can not create folder ' folderName])
        disp (MESSAGE)
        pause
    copyfile([structureDir currentFileName], folderName);
    copyfile([lammpsSampleDir '*'],folderName);
    % Modify .in file
    inFile = readList([folderName '/eq.in'],-1);
    inFileNew = inFile;
    inFileNew = replaceLine(inFileNew, 10, ['read data ' currentFileName]);
    inFileNew = replaceLine(inFileNew, 27, ['variable T0 equal ' num2str(eqTemperature)]);
    inFileNew = replaceLine(inFileNew, 28, ['variable eqStep equal 'num2str(eqStep)]);
   1 all custom '
    % Modify .qsub file
    qsubFile = readList([folderName '/lammpsJob.qsub'],-1);
    qsubFileNew = qsubFile;
    qsubFileNew = replaceLine(qsubFileNew, 2, ['#PBS -1 ' lparam]);
qsubFileNew = replaceLine(qsubFileNew, 15, ['cd ' parentDir folderName]);
    writeList([folderName '/lammpsJob.qsub'],qsubFileNew);
    % create status file
    status = 'CreatedLammpsJob';
    writeList([folderName '/status.txt'], status);
if(~strcmp(computer, 'PCWIN64'))
    exit;
end
```

Extract Structures from LAMMPS Trajectory

```
%% Search all lammps jobs and extract structures from trajectory file
% Load settings
globalSettings
if(strcmp(computer, 'PCWIN64'))
    workingDir = 'F:\SPG\AutomaticTrainingSet\workingDir\';
    trainingSetDir = 'F:\SPG\AutomaticTrainingSet\workingDir\trainingSet\';
end
% Read folders
allDir = dir (workingDir);
if(~exist(trainingSetDir,'dir'))
    mkdir(trainingSetDir);
for i = 3:size(allDir,1)
    currentFolder = allDir(i).name;
    if (~allDir(i).isdir)
        continue
    end
    if(length(currentFolder) < 6)</pre>
        continue
    end
    fileType = currentFolder(end-5:end);
    if(~strcmp(fileType,'lammps'))
        continue
    end
    currentStatus = readList([currentFolder '/status.txt']);
    if(~strcmp(currentStatus,'CreatedLammpsJob'))
        continue
    end
   if(~exist([currentFolder '/eq.xyz'],'file'))
    disp(['No xyz file in ' currentFolder]);
        continue
    end
    % Read structures and info
    originalFileName = regexp(currentFolder,'(.*?)-','tokens');
    infoFile = readList([structureDir originalFileName{1}{1} '.txt']);
    [iterm,value] = readInfo([structureDir originalFileName{1}{1} '.txt']);
   Natoms = 0;
   pickMDMin = 0;
    for j = 1:length(iterm)
        if(strcmp(iterm{j},'Natoms'))
            Natoms = value(j);
            NatomsErr = 5;
        end
        if(strcmp(iterm{j},'NatomsErr'))
            NatomsErr = value(j);
        end
        if(strcmp(iterm{j},'pickMDMin'))
            pickMDMin = value(j);
        end
        if(strcmp(iterm{j},'NSample'))
            NSample = value(j);
        end
   end
   [timeStep,atomNum,atomIdx,atomElement,coordinates,force,atomCharge,cellLength] =
   readLammpsTrajectory9([currentFolder '/eq.xyz'],0);
   Nstructures = size(coordinates,3);
   randomSample = randperm(Nstructures);
   sampleIdx = randomSample(1:NSample);
   if (pickMDMin)
       if(pickMDMin < NSample)</pre>
           disp('NSample is smaller than pickMDMin!')
```

```
MDLogFile = readList([currentFolder '/eq.txt']);
    MDLogFile(1,:) = [];
    MDLogData = str2num(MDLogFile);
    MDEp = MDLogData(:,9);
    [MDEpSort, MDEpSortIdx] = sort(MDEp);
    pickMDMinIdx = MDEpSortIdx(1:pickMDMin);
    for k = 1:length(pickMDMinIdx)
        randomSample (randomSample == pickMDMinIdx(k)) = [];
    end
    sampleIdx = [MDEpSortIdx(1:pickMDMin)' randomSample(1:(NSample - pickMDMin))];
end
% Save structures
for j = 1:NSample
    outputLammpsFilename = [currentFolder(1:end-6) num2str(j) '.data'];
    outputVASPFilename = [currentFolder(1:end-6) num2str(j)
    outputInfoFilename = [currentFolder(1:end-6) num2str(j) '.txt'];
    lammpsCellLength =
    [cellLength(1:2,sampleIdx(j))';cellLength(3:4,sampleIdx(j))';cellLength(5:6,sampleIdx(j))
    '1;
    vaspCellLength = diag(cellLength(2:2:6, sampleIdx(j))) - cellLength(1:2:5, sampleIdx(j)));
    if(Natoms == 0 || Natoms >= atomNum(j)) % use original structure
        currentCoord = coordinates(:,:,sampleIdx(j));
        currentElement = atomElement(:,sampleIdx(j));
        newAtomNum = atomNum(:,sampleIdx(j));
        for k = 1:max(atomElement(:,sampleIdx(j)));
            newAtomNum(k) = sum(currentElement == k);
        [Y, I] = sort(currentElement);
        sortCoord = currentCoord(I,:);
       writeLammpsData(outputLammpsFilename,atomNum(:,sampleIdx(j)), lammpsCellLength, 0,
        coordinates(:,:,sampleIdx(j)), [trainingSetDir outputLammpsFilename]);
        writePOSCAR([trainingSetDir
       outputVASPFilename],outputVASPFilename,1,vaspCellLength,atomName,newAtomNum,sortCoord
       writeList([trainingSetDir outputInfoFilename],infoFile);
   else % cut structure
       totalAtoms = sum(double(atomNum(:,sampleIdx(j))));
        if(totalAtoms < Natoms)</pre>
            disp(currentFolder);
            disp('Not enough atoms!');
        end
        newlammpsCellLength = (Natoms/totalAtoms).^(1/3)*lammpsCellLength;
       newVaspCellLength = (Natoms/totalAtoms).^(1/3)*vaspCellLength;
        % find atoms to be deleted
       deleteIdx = zeros(totalAtoms - Natoms,1);
       idxN = 1:
       currentCoord = coordinates(:,:,sampleIdx(j));
        currentElement = atomElement(:,sampleIdx(j));
        for k = 1:size(coordinates,1)
           currentAtom = currentCoord(k,:);
            if(currentAtom(1) < newlammpsCellLength(1,1) || currentAtom(1) >
           newlammpsCellLength(1,2) ||...
               currentAtom(2) < newlammpsCellLength(2,1) || currentAtom(2) >
               newlammpsCellLength(2,2) ||...
               currentAtom(3) < newlammpsCellLength(3,1) || currentAtom(3) >
               newlammpsCellLength(3,2))
               deleteIdx(idxN) = k;
               idxN = idxN + 1;
            end
        end
        deleteIdx (deleteIdx == 0) = [];
        actualAtomNum = totalAtoms - length(deleteIdx);
        if(abs(actualAtomNum/Natoms) > NatomsErr)
```

```
disp(currentFolder);
                                                        disp('Actual number of atoms might be wrong')
disp(['Actual number of atoms: ' num2str(actualAtomNum)])
disp(['Target number: ' num2str(Natoms)])
                                           end
                                           % delete atoms
                                           currentCoord(deleteIdx,:) = [];
                                           currentElement(deleteIdx) = [];
                                           % write lammps data
                                           newAtomNum = atomNum(:,sampleIdx(j));
                                           for k = 1:max(atomElement(:,sampleIdx(j)));
                                                        newAtomNum(k) = sum(currentElement == k);
                                           end
                                                  if(sum(diff(currentElement)) > length(newAtomNum))
00
                                                               disp(currentFolder);
                                                               disp('Atom elements must be sorted');
                                                 end
                                           % sort the positions according to element
                                           [Y, I] = sort(currentElement);
                                           sortCoord = currentCoord(I,:);
                                          \label{lem:writeLammpsDataDirect (outputLammpsFilename, newAtomNum, length (newAtomNum), currentElement, newlammpsCellLength, 0, currentCoord, [trainingSetDirectCoord, currentCoord, 
                                           outputLammpsFilename]);
                                           writePOSCAR([trainingSetDir
                                           outputVASPFilename],outputVASPFilename,1,newVaspCellLength,atomName,newAtomNum,
                                           sortCoord);
                                           writeList([trainingSetDir outputInfoFilename],infoFile);
                             end
               end
  end
  if(~strcmp(computer, 'PCWIN64'))
               exit;
  end
```

Generate VASP Jobs

```
%% Generate the vasp job from a structure file
000
clear;
% Load settings
globalSettings
% Pre-process
% Read all structures
structureList = dir(VASPStructureDir);
for i = 3:size(structureList,1)
     currentFileName = structureList(i).name;
     if(~strcmp(currentFileName(end-3:end),'vasp'))
         continue
     end
     folderName = [currentFileName(1:end-5) '-vasp'];
     % For each structure, create seperate folder and copy files
[SUCCESS,MESSAGE,MESSAGEID] = mkdir(folderName);
     if (SUCCESS ~= 1)
          disp(['Can not create folder ' folderName])
         disp (MESSAGE)
         pause
     end
    copyfile([VASPStructureDir currentFileName],folderName);
copyfile([VASPStructureDir currentFileName],[folderName '/POSCAR']);
copyfile([VASPSampleDir '*'],folderName);
     % Read info file
     % TODO: put the info file into originalStructures folder -> control
     infoFileName = [currentFileName(1:end-5) '.txt'];
     % originalFileName = regexp(currentFileName,'(.*?)-','tokens');
     [iterm, value] = readInfo([VASPStructureDir infoFileName]);
    NSW = 1:
    \texttt{KPOINTS} = [1 \ 1 \ 1];
    for j = 1:length(iterm)
         if(strcmp(iterm{j},'NSW'))
             NSW = value(j);
         if(strcmp(iterm{j},'KPOINTS1'))
              KPOINTS = value(j:j+2)';
         end
    end
     % Modify INCAR file
     INCARFile = readList([folderName '/INCAR'],-1);
     INCARFileNew = INCARFile;
    INCARFileNew = replaceLine(INCARFileNew, 6, [' ENCUT = ' num2str(E_cutoff)]);
INCARFileNew = replaceLine(INCARFileNew, 8, ['NSW = ' num2str(NSW)]);
    writeList([folderName '/INCAR'],INCARFileNew);
    % Modify KPOINTS
    KPOINTSFile = readList([folderName '/KPOINTS'],-1);
    KPOINTSFileNew = KPOINTSFile;
    KPOINTSFileNew = replaceLine(KPOINTSFileNew, 4, [num2str(KPOINTS)]);
    % Modify .qsub file
    qsubFile = readList([folderName '/vaspJob.qsub'],-1);
    qsubFileNew = qsubFile;
    qsubFileNew = replaceLine(qsubFileNew, 2, ['#PBS -1 ' lparam2]);
qsubFileNew = replaceLine(qsubFileNew, 17, ['cd ' parentDir2 folderName]);
writeList([folderName '/vaspJob.qsub'],qsubFileNew);
    status = 'CreatedVASPJob';
     writeList([folderName '/status.txt'],status);
if(~strcmp(computer,'PCWIN64'))
    exit;
end
```

Extract Energies from VASP

```
%% Collect Energy results from different folder and add to info file
% This code will go to each folder, read corresponding energy value and
% add the energy to info file
clear;
% Load settings
globalSettings
path(path,'/mnt/home/jlliu/Documents/MATLAB/vasplab')
% Test
% workingDir = 'F:\SPG\AutomaticTrainingSet\workingDir\';
% trainingSetDir = 'F:\SPG\AutomaticTrainingSet\workingDir\trainingSet\';
files = dir (workingDir);
%% check vasp jobs status
% testFolder = 'F:\SPG\LiCoO2\cluster\K1-re\clusterLi37Co6O26 6+V\';
% exprPath = '.*\\(.*)\\';
result = '';
for i = 3:length(files)
    currentFileName = files(i).name;
    if((~files(i).isdir)||(~strcmp(currentFileName(end-3:end),'vasp')))
        continue
    end
    currentFolder = [workingDir files(i).name '/'];
    infoFileName = [currentFileName(1:end-5) '.txt'];
    collectTrainingSet(currentFolder, trainingSetDir);
end
% save results
% writeList([parentFolderName{1}{1} '.txt'], result);
```

Collect Structures and Energies into Database

```
function collectTrainingSet(folderName, trainingSetDir)
%% Collect structure and energy from current folder to training set folder
% collectTrainingSet(currentFolder, trainingSetDir)
status = 0;
% Read energy from OSZICAR
OSZICAR_filepath = [folderName 'OSZICAR'];
if(~exist(OSZICAR filepath, 'file'))
    status = 0;
    energy = NaN;
disp(['No OSZICAR file in ' folderName])
    return
else
    energy = import_oszicar(OSZICAR_filepath);
if(isempty(energy))
    status = 0;
    disp(['Error in ' folderName])
end
% Read structures from POSCAR
POSCAR_filepath = [folderName 'POSCAR'];
geometry = import poscar( POSCAR filepath );
natoms = sum(geometry.atomcount);
% Read structures from OUTCAR
structures = zeros(natoms, 3, length(energy));
OUTCAR filepath = [folderName 'OUTCAR'];
if(~exist(OUTCAR_filepath,'file'))
    status = 0;
    energy = NaN;
disp(['No OUTCAR file in ' folderName])
    return
else
    OUTCAR file = readList([folderName 'OUTCAR']);
    nStep = 1;
    for i = 1:size(OUTCAR file,1)
        if(strfind(OUTCAR file(i,:),'POSITION
                                                                                       TOTAL-FORCE
        (eV/Angst)'))
            positionText = OUTCAR_file(i+2:i+1+natoms,:);
            currentStructures = textscan(positionText','%f %f %f %f %f %f');
            structures(:,:,nStep) = [currentStructures{1,1} currentStructures{1,2}
            currentStructures {1,3}];
            nStep = nStep + 1;
        end
    end
% write status file
if (status)
    statusFile = readList([folderName 'status.txt']);
    statusFile = char(statusFile,'Energy and structures collected');
    writeList([folderName 'status.txt'],statusFile);
% add structures to training set folder
exprPath = '.*\/(.*)\/';
filenameReg = regexp(folderName,exprPath,'tokens');
filename = filenameReg{1}{1};
if(size(energy, 2) == 1)
    infoFile = readList([trainingSetDir filename(1:end-5) '.txt']);
    infoFile = char(infoFile,['Energy,' num2str(energy)]);
    writeList([trainingSetDir filename(1:end-5) '.txt'],infoFile);
elseif(size(energy,2) > 1)
```

```
infoFile = readList([trainingSetDir filename(1:end-5) '.txt']);
infoFile = char(infoFile,['Energy,' num2str(energy(1))]);
writeList([trainingSetDir filename(1:end-5) '.txt'],infoFile);
for i = 2:length(energy)
    % generate new file
    copyfile([trainingSetDir filename(1:end-5) '.txt'],[trainingSetDir filename(1:end-5)
    '-' num2str(length(energy) - i + 1) '.txt'])
    copyfile([trainingSetDir filename(1:end-5) '.vasp'],[trainingSetDir filename(1:end-5)
       num2str(length(energy) - i + 1) '.vasp'])
    % change info file
    infoFile = readList([trainingSetDir filename(1:end-5) '-' num2str(length(energy) - i +
    1) '.txt']);
    infoFile(end,:) = [];
    infoFile = char(infoFile,['Energy,' num2str(energy(i))]);
    writeList([trainingSetDir filename(1:end-5) '-' num2str(length(energy) - i + 1)
    '.txt'],infoFile);
    % change structure file
    structureFile = readList([trainingSetDir filename(1:end-5) '-' num2str(length(energy) -
    i + 1) '.vasp']);
    structureFile(end - natoms + 1 :end,:) = [];
    structureFile = char(structureFile,num2str(structures(:,:,i)));
    writeList([trainingSetDir filename(1:end-5) '-' num2str(length(energy) - i + 1)
    '.vasp'], structureFile);
end
```

end end

REFERENCES

REFERENCES

- (1) Tarascon, J. M.; Armand, M. Issues and Challenges Facing Rechargeable Lithium Batteries. *Nature* **2001**, *414*, 359–367.
- (2) Goodenough, J. B.; Kim, Y. Challenges for Rechargeable Batteries. *J. Power Sources* **2011**, *196*, 6688–6694.
- (3) Goodenough, J. B.; Park, K. S. The Li-Ion Rechargeable Battery: A Perspective. *J. Am. Chem. Soc.* **2013**, *135*, 1167–1176.
- (4) Zhou, L. Progress and Problems in Hydrogen Storage Methods. *Renew. Sustain. Energy Rev.* **2005**, *9*, 395–408.
- (5) Obrovac, M. N.; Christensen, L.; Le, D. B.; Dahn, J. R. Alloy Design for Lithium-Ion Battery Anodes. *J. Electrochem. Soc.* **2007**, *154*, A849.
- (6) Obrovac, M. N.; Chevrier, V. L. Alloy Negative Electrodes for Li-Ion Batteries. *Chem. Rev.* **2014**, *114*, 11444–11502.
- (7) Choi, J. W.; Aurbach, D. Promise and Reality of Post-Lithium-Ion Batteries with High Energy Densities. *Nat. Rev. Mater.* **2016**, *1*.
- (8) Beaulieu, L. Y.; Eberman, K. W.; Turner, R. L.; Krause, L. J.; Dahn, J. R. Colossal Reversible Volume Changes in Lithium Alloys. *Electrochem. Solid-State Lett.* **2001**, *4*, A137.
- (9) Zhang, W. J. Lithium Insertion/Extraction Mechanism in Alloy Anodes for Lithium-Ion Batteries. *J. Power Sources* **2011**, *196*, 877–885.
- (10) Kasavajjula, U.; Wang, C.; Appleby, A. J. Nano- and Bulk-Silicon-Based Insertion Anodes for Lithium-Ion Secondary Cells. *J. Power Sources* **2007**, *163*, 1003–1039.
- (11) Larcher, D.; Beattie, S.; Morcrette, M.; Edström, K.; Jumas, J. C.; Tarascon, J. M. Recent Findings and Prospects in the Field of Pure Metals as Negative Electrodes for Li-Ion Batteries. *J. Mater. Chem.* **2007**, *17*, 3759–3772.
- (12) Li, J.-Y.; Xu, Q.; Li, G.; Yin, Y.-X.; Wan, L.-J.; Guo, Y.-G. Research Progress Regarding Si-Based Anode Materials towards Practical Application in High Energy Density Li-Ion Batteries. *Mater. Chem. Front.* **2017**, 1691–1708.
- (13) Jung, S. C.; Kim, H. J.; Kim, J. H.; Han, Y. K. Atomic-Level Understanding toward a High-Capacity and High-Power Silicon Oxide (SiO) Material. J. Phys. Chem. C 2016, 120, 886–892.
- (14) Zhao, J.; Lu, Z.; Wang, H.; Liu, W.; Lee, H.-W.; Yan, K.; Zhuo, D.; Lin, D.; Liu, N.; Cui,

- Y. Artificial Solid Electrolyte Interphase-Protected Li _x Si Nanoparticles: An Efficient and Stable Prelithiation Reagent for Lithium-Ion Batteries. *J. Am. Chem. Soc.* **2015**, *137*, 8372–8375.
- (15) Yin, Y. X.; Wan, L. J.; Guo, Y. G. Silicon-Based Nanomaterials for Lithium-Ion Batteries. *Chinese Sci. Bull.* **2012**, *57*, 4104–4110.
- (16) Yang, H.; Huang, S.; Huang, X.; Fan, F.; Liang, W.; Liu, X. H.; Chen, L. Q.; Huang, J. Y.; Li, J.; Zhu, T.; *et al.* Orientation-Dependent Interfacial Mobility Governs the Anisotropic Swelling in Lithiated Silicon Nanowires. *Nano Lett.* **2012**, *12*, 1953–1958.
- (17) Chan, C. K.; Patel, R. N.; O'Connell, M. J.; Korgel, B. a.; Cui, Y. Solution-Grown Silicon Nanowires for Lithium-Ion Battery Anodes. *ACS Nano* **2010**, *4*, 1443–1450.
- (18) Chan, C. K.; Peng, H.; Liu, G.; McIlwrath, K.; Zhang, X. F.; Huggins, R. A.; Cui, Y. High-Performance Lithium Battery Anodes Using Silicon Nanowires. *Nat. Nanotechnol.* **2008**, *3*, 31–35.
- (19) Liu, N.; Lu, Z.; Zhao, J.; Mcdowell, M. T.; Lee, H. W.; Zhao, W.; Cui, Y. A Pomegranate-Inspired Nanoscale Design for Large-Volume-Change Lithium Battery Anodes. *Nat. Nanotechnol.* **2014**, *9*, 187–192.
- (20) McDowell, M. T.; Ryu, I.; Lee, S. W.; Wang, C.; Nix, W. D.; Cui, Y. Studying the Kinetics of Crystalline Silicon Nanoparticle Lithiation with in Situ Transmission Electron Microscopy. *Adv. Mater.* **2012**, *24*, 6034–6041.
- (21) Song, T.; Xia, J.; Lee, J. H.; Lee, D. H.; Kwon, M. S.; Choi, J. M.; Wu, J.; Doo, S. K.; Chang, H.; Park, W. II; *et al.* Arrays of Sealed Silicon Nanotubes as Anodes for Lithium Ion Batteries. *Nano Lett.* **2010**, *10*, 1710–1716.
- (22) Park, M.-H.; Gyu Kim, M.; Joo, J.; Kim, K.; Kim, J.; Ahn, S.; Cui, Y.; Cho, J. Silicon Nanotube Battery Anodes. **2009**.
- (23) Ma, H.; Cheng, F.; Chen, J.; Zhao, J.; Li, C.; Tao, Z.; Liang, J. Nest-like Silicon Nanospheres for High-Capacity Lithium Storage. *Adv. Mater.* **2007**, *19*, 4067–4070.
- (24) Pinson, M. B.; Bazant, M. Z. Theory of SEI Formation in Rechargeable Batteries: Capacity Fade, Accelerated Aging and Lifetime Prediction. *J. Electrochem. Soc.* **2012**, *160*, A243–A250.
- (25) Ko, M.; Chae, S.; Cho, J. Challenges in Accommodating Volume Change of Si Anodes for Li-Ion Batteries. *ChemElectroChem* **2015**, 2, 1645–1651.
- (26) Verma, P.; Maire, P.; Novák, P. A Review of the Features and Analyses of the Solid Electrolyte Interphase in Li-Ion Batteries. *Electrochim. Acta* **2010**, *55*, 6332–6341.
- (27) Lee, J. H.; Kim, W. J.; Kim, J. Y.; Lim, S. H.; Lee, S. M. Spherical Silicon/Graphite/Carbon Composites as Anode Material for Lithium-Ion Batteries. *J. Power Sources* **2008**, *176*, 353–

- (28) Jeong, G.; Kim, J. G.; Park, M. S.; Seo, M.; Hwang, S. M.; Kim, Y. U.; Kim, Y. J.; Kim, J. H.; Dou, S. X. Core-Shell Structured Silicon Nanoparticles@TiO2-x/Carbon Mesoporous Microfiber Composite as a Safe and High-Performance Lithium-Ion Battery Anode. ACS Nano 2014, 8, 2977–2985.
- (29) Chen, T.; Wu, J.; Zhang, Q.; Su, X. Recent Advancement of SiOxbased Anodes for Lithium-Ion Batteries. *J. Power Sources* **2017**, *363*, 126–144.
- (30) Wei, L.; Hou, Z. High Performance Polymer Binders Inspired by Chemical Finishing of Textiles for Silicon Anodes in Lithium Ion Batteries. *J. Mater. Chem. A* **2017**, *5*, 22156–22162.
- (31) Limthongkul, P.; Jang, Y. Il; Dudney, N. J.; Chiang, Y. M. Electrochemically-Driven Solid-State Amorphization in Lithium-Silicon Alloys and Implications for Lithium Storage. *Acta Mater.* **2003**, *51*, 1103–1113.
- (32) Limthongkul, P.; Jang, Y. Il; Dudney, N. J.; Chiang, Y. M. Electrochemically-Driven Solid-State Amorphization in Lithium-Metal Anodes. *J. Power Sources* **2003**, *119–121*, 604–609.
- (33) Li, J.; Dahn, J. R. An In Situ X-Ray Diffraction Study of the Reaction of Li with Crystalline Si. *J. Electrochem. Soc.* **2007**, *154*, A156.
- (34) Hatchard, T. D.; Dahn, J. R. In Situ XRD and Electrochemical Study of the Reaction of Lithium with Amorphous Silicon. *J. Electrochem. Soc.* **2004**, *151*, A838.
- (35) Key, B.; Bhattacharyya, R.; Morcrette, M.; Sezne, V.; Tarascon, J.; Grey, C. P. Real-Time NMR Investigations of Structural Changes in Silicon Electrodes for Lithium-Ion Batteries Real-Time NMR Investigations of Structural Changes in Silicon Electrodes for Lithium-Ion Batteries. *Society* **2009**, *131*, 9239–9249.
- (36) Key, B.; Morcrette, M.; Tarascon, J.; Grey, C. P. Pair Distribution Function Analysis and Solid State NMR Studies of Silicon Electrodes for Lithium Ion Batteries: Understanding the (De) Lithiation Mechanisms. **2011**, 503–512.
- (37) Chon, M. J.; Sethuraman, V. A.; McCormick, A.; Srinivasan, V.; Guduru, P. R. Real-Time Measurement of Stress and Damage Evolution during Initial Lithiation of Crystalline Silicon. *Phys. Rev. Lett.* **2011**, *107*, 1–4.
- (38) Obrovac, M. N.; Christensen, L. Structural Changes in Silicon Anodes during Lithium Insertion/Extraction. *Electrochem. Solid-State Lett.* **2004**, *7*, A93.
- (39) Li, H.; Huang, X.; Chen, L.; Zhou, G.; Zhang, Z.; Yu, D.; Jun Mo, Y.; Pei, N. Crystal Structural Evolution of Nano-Si Anode Caused by Lithium Insertion and Extraction at Room Temperature. *Solid State Ionics* **2000**, *135*, 181–191.
- (40) Okamoto, H. The Li-Si (Lithium-Silicon) System. Bull. Alloy Phase Diagrams 1990, 11,

- 306-312.
- (41) McDowell, M. T.; Lee, S. W.; Nix, W. D.; Cui, Y. 25th Anniversary Article: Understanding the Lithiation of Silicon and Other Alloying Anodes for Lithium-Ion Batteries. *Adv. Mater.* **2013**, *25*, 4966–4985.
- (42) Wen, C. J.; Huggins, R. A. Chemical Diffusion in Intermediate Phases in the Lithium-Silicon System. *J. Solid State Chem.* **1981**, *37*, 271–278.
- (43) Liu, X. H.; Wang, J. W.; Huang, S.; Fan, F.; Huang, X.; Liu, Y.; Krylyuk, S.; Yoo, J.; Dayeh, S. a.; Davydov, A. V.; *et al.* In Situ Atomic-Scale Imaging of Electrochemical Lithiation in Silicon. *Nat. Nanotechnol.* **2012**, *7*, 749–756.
- (44) Liu, X. H.; Zheng, H.; Zhong, L.; Huang, S.; Karki, K.; Zhang, L. Q.; Liu, Y.; Kushima, A.; Liang, W. T.; Wang, J. W.; *et al.* Anisotropic Swelling and Fracture of Silicon Nanowires during Lithiation. *Nano Lett.* **2011**, *11*, 3312–3318.
- (45) Lee, S. W.; McDowell, M. T.; Choi, J. W.; Cui, Y. Anomalous Shape Changes of Silicon Nanopillars by Electrochemical Lithiation. *Nano Lett.* **2011**, *11*, 3034–3039.
- (46) McDowell, M. T.; Lee, S. W.; Harris, J. T.; Korgel, B. A.; Wang, C.; Nix, W. D.; Cui, Y. In Situ TEM of Two-Phase Lithiation of Amorphous Silicon Nanospheres. *Nano Lett.* **2013**, *13*, 758–764.
- (47) Wang, J. W.; He, Y.; Fan, F.; Liu, X. H.; Xia, S.; Liu, Y.; Harris, C. T.; Li, H.; Huang, J. Y.; Mao, S. X.; *et al.* Two-Phase Electrochemical Lithiation in Amorphous Silicon. *Nano Lett.* **2013**, *13*, 709–715.
- (48) Horstemeyer, M. F. Multiscale Modeling: A Review. In *Practical Aspects of Computational Chemistry*; Springer Netherlands: Dordrecht, 2009; pp. 87–135.
- (49) Shenoy, V. B.; Johari, P.; Qi, Y. Elastic Softening of Amorphous and Crystalline Li-Si Phases with Increasing Li Concentration: A First-Principles Study. *J. Power Sources* **2010**, *195*, 6825–6830.
- (50) Kubota, Y.; Escaño, M. C. S.; Nakanishi, H.; Kasai, H. Electronic Structure of LiSi. *J. Alloys Compd.* **2008**, 458, 151–157.
- (51) Chan, M. K. Y.; Wolverton, C.; Greeley, J. P. First Principles Simulations of the Electrochemical Lithiation and Delithiation of Faceted Crystalline Silicon. *J. Am. Chem. Soc.* **2012**, *134*, 14362–14374.
- (52) Chevrier, V. L.; Dahn, J. R. First Principles Model of Amorphous Silicon Lithiation. *J. Electrochem. Soc.* **2009**, *156*, A454.
- (53) Chevrier, V. L.; Dahn, J. R. First Principles Studies of Disordered Lithiated Silicon. *J. Electrochem. Soc.* **2010**, *157*, A392.

- (54) Chevrier, V. L.; Zwanziger, J. W.; Dahn, J. R. First Principles Study of Li-Si Crystalline Phases: Charge Transfer, Electronic Structure, and Lattice Vibrations. *J. Alloys Compd.* **2010**, *496*, 25–36.
- (55) Kim, H.; Chou, C. Y.; Ekerdt, J. G.; Hwang, G. S. Structure and Properties of Li-Si Alloys: A First-Principles Study. *J. Phys. Chem. C* **2011**, *115*, 2514–2521.
- (56) Johari, P.; Qi, Y.; Shenoy, V. B. The Mixing Mechanism during Lithiation of Si Negative Electrode in Li-Ion Batteries: An Ab Initio Molecular Dynamics Study. *Nano Lett.* **2011**, *11*, 5494–5500.
- (57) Jung, S. C.; Han, Y. K. Ab Initio Molecular Dynamics Simulation of Lithiation-Induced Phase-Transition of Crystalline Silicon. *Electrochim. Acta* **2012**, *62*, 73–76.
- (58) Wang, Z.; Su, Q.; Deng, H.; Fu, Y. Composition Dependence of Lithium Diffusion in Lithium Silicide: A Density Functional Theory Study. *ChemElectroChem* **2015**, 2, 1292–1297.
- (59) Fan, F.; Huang, S.; Yang, H.; Raju, M.; Datta, D.; Shenoy, V. B.; Van Duin, A. C. T.; Zhang, S.; Zhu, T. Mechanical Properties of Amorphous LixSi Alloys: A Reactive Force Field Study. *Model. Simul. Mater. Sci. Eng.* **2013**, *21*.
- (60) Russo, M. F.; Van Duin, A. C. T. Atomistic-Scale Simulations of Chemical Reactions: Bridging from Quantum Chemistry to Engineering. *Nucl. Instruments Methods Phys. Res. Sect. B Beam Interact. with Mater. Atoms* **2011**, 269, 1549–1554.
- (61) Senftle, T. P.; Hong, S.; Islam, M. M.; Kylasa, S. B.; Zheng, Y.; Shin, Y. K.; Junkermeier, C.; Engel-Herbert, R.; Janik, M. J.; Aktulga, H. M.; *et al.* The ReaxFF Reactive Force-Field: Development, Applications and Future Directions. *npj Comput. Mater.* **2016**, 2.
- (62) Kim, S. P.; Datta, D.; Shenoy, V. B. Atomistic Mechanisms of Phase Boundary Evolution during Initial Lithiation of Crystalline Silicon. *J. Phys. Chem. C* **2014**, *118*, 17247–17253.
- (63) Jung, H.; Lee, M.; Yeo, B. C.; Lee, K. R.; Han, S. S. Atomistic Observation of the Lithiation and Delithiation Behaviors of Silicon Nanowires Using Reactive Molecular Dynamics Simulations. *J. Phys. Chem. C* **2015**, *119*, 3447–3455.
- (64) Ostadhossein, A.; Cubuk, E. D.; Tritsaris, G. A.; Kaxiras, E.; Zhang, S.; van Duin, A. C. T. Stress Effects on the Initial Lithiation of Crystalline Silicon Nanowires: Reactive Molecular Dynamics Simulations Using ReaxFF. *Phys. Chem. Chem. Phys.* **2015**, *17*, 3832–3840.
- (65) McQuarrie, D. A. *Quantum Chemistry*; University Science Books, 2008.
- (66) Sholl, D. S.; Steckel, J. A. *Density Functional Theory*; John Wiley & Sons, Inc.: Hoboken, NJ, USA, 2009.
- (67) Kittel, C.; Fan, H. Y. Introduction to Solid State Physics. Am. J. Phys. 1957, 25, 330–330.

- (68) Pack, J. D.; Monkhorst, H. J. "special Points for Brillouin-Zone Integrations"-a Reply. *Phys. Rev. B* **1977**, *16*, 1748–1749.
- (69) González, M. A. Force Fields and Molecular Dynamics Simulations. *Collect. SFN* **2011**, *12*, 169–200.
- (70) *Molecular Modeling of Geochemical Reactions*; Kubicki, J. D., Ed.; John Wiley &;#38; Sons, Ltd: Chichester, UK, 2016.
- (71) Monticelli, L.; Tieleman, D. P. Force Fields for Classical Molecular Dynamics. In; 2013; pp. 197–213.
- (72) Van Duin, A. C. T.; Dasgupta, S.; Lorant, F.; Goddard, W. A. ReaxFF: A Reactive Force Field for Hydrocarbons. *J. Phys. Chem. A* **2001**, *105*, 9396–9409.
- (73) van Duin, A. C. T.; Strachan, A.; Stewman, S.; Zhang, Q.; Xu, X.; Goddard, W. A. ReaxFF Sio Reactive Force Field for Silicon and Silicon Oxide Systems. J. Phys. Chem. A 2003, 107, 3803–3811.
- (74) Narayanan, B.; Van Duin, A. C. T.; Kappes, B. B.; Reimanis, I. E.; Ciobanu, C. V. A Reactive Force Field for Lithium-Aluminum Silicates with Applications to Eucryptite Phases. *Model. Simul. Mater. Sci. Eng.* **2012**, *20*.
- (75) Rappé, A. K.; Goddard, W. A. Charge Equilibration for Molecular Dynamics Simulations. *J. Phys. Chem.* **1991**, *95*, 3358–3363.
- (76) Mortier, W. J.; Ghosh, S. K.; Shankar, S. Electronegativity Equalization Method for the Calculation of Atomic Charges in Molecules. *J. Am. Chem. Soc.* **1986**, *108*, 4315–4320.
- (77) Frenkel, D.; Smit, B.; Tobochnik, J.; McKay, S. R.; Christian, W. Understanding Molecular Simulation. *Comput. Phys.* **1997**, *11*, 351.
- (78) Ostadhossein, A.; Cubuk, E. D.; Tritsaris, G. A.; Kaxiras, E.; Zhang, S.; Van Duin, A. C. T. Stress Effects on the Initial Lithiation of Crystalline Silicon Nanowires: Reactive Molecular Dynamics Simulations Using ReaxFF. *Phys. Chem. Chem. Phys.* **2015**, *17*, 3832–3840.
- (79) Balke, N.; Jesse, S.; Kim, Y.; Adamczyk, L.; Tselev, A.; Ivanov, I. N.; Dudney, N. J.; Kalinin, S. V. Real Space Mapping of Li-Ion Transport in Amorphous Si Anodes with Nanometer Resolution. *Nano Lett.* **2010**, *10*, 3420–3425.
- (80) Pell, E. M. Diffusion of Li in Si at High T and the Isotope Effect. **1960**, *1049*.
- (81) Goldman, J. L.; Long, B. R.; Gewirth, A. A.; Nuzzo, R. G. Strain Anisotropies and Self-Limiting Capacities in Single-Crystalline 3D Silicon Microstructures: Models for High Energy Density Lithium-Ion Battery Anodes. *Adv. Funct. Mater.* **2011**, *21*, 2412–2422.
- (82) Kulish, V. V.; Malyi, O. I.; Ng, M. F.; Wu, P.; Chen, Z. Enhanced Li Adsorption and Diffusion in Silicon Nanosheets Based on First Principles Calculations. *RSC Adv.* **2013**, *3*,

- 4231–4236.
- (83) Wan, W.; Zhang, Q.; Cui, Y.; Wang, E. First Principles Study of Lithium Insertion in Bulk Silicon. *J. Phys. Condens. Matter* **2010**, 22.
- (84) Haldar, P.; Chatterjee, A. Nudged-Elastic Band Study of Lithium Diffusion in Bulk Silicon in the Presence of Strain. *Energy Procedia* **2014**, *54*, 310–319.
- (85) Kim, H.; Kweon, K. E.; Chou, C. Y.; Ekerdt, J. G.; Hwang, G. S. On the Nature and Behavior of Li Atoms in Si: A First Principles Study. *J. Phys. Chem. C* **2010**, *114*, 17954–17959.
- (86) Wang, Z.; Gu, M.; Zhou, Y.; Zu, X.; Connell, J. G.; Xiao, J.; Perea, D.; Lauhon, L. J.; Bang, J.; Zhang, S.; et al. Electron-Rich Driven Electrochemical Solid-State Amorphization in Li-Si Alloys. Nano Lett. 2013, 13, 4511–4516.
- (87) Hedler, A.; Klaumünzer, S. L.; Wesch, W. Amorphous Silicon Exhibits a Glass Transition. *Nat. Mater.* **2004**, *3*, 804–809.
- (88) Matsumura, H.; Tachibana, H. Amorphous Silicon Produced by a New Thermal Chemical Vapor Deposition Method Using Intermediate Species SiF2. *Appl. Phys. Lett.* **1985**, *47*, 833–835.
- (89) Liu, P. L.; Yen, R.; Bloembergen, N.; Hodgson, R. T. Picosecond Laser-Induced Melting and Resolidification Morphology on Si. *Appl. Phys. Lett.* **1979**, *34*, 864–866.
- (90) Glaser, E.; Götz, G.; Sobolev, N.; Wesch, W. Investigations of Radiation Damage Production in Ion Implanated Silicon. *Phys. Status Solidi* **1982**, *69*, 603–614.
- (91) Pelaz, L.; Marqús, L. A.; Barbolla, J. Ion-Beam-Induced Amorphization and Recrystallization in Silicon. *J. Appl. Phys.* **2004**, *96*, 5947–5976.
- (92) Williams, J. S.; Conway, M. J.; Williams, B. C.; Wong-Leung, J. Direct Observation of Voids in the Vacancy Excess Region of Ion Bombarded Silicon. *Appl. Phys. Lett.* **2001**, 78, 2867–2869.
- (93) Li, J.; Dudney, N. J.; Xiao, X.; Cheng, Y. T.; Liang, C.; Verbrugge, M. W. Asymmetric Rate Behavior of Si Anodes for Lithium-Ion Batteries: Ultrafast de-Lithiation versus Sluggish Lithiation at High Current Densities. *Adv. Energy Mater.* **2015**, *5*, 1–6.
- (94) Jagannathan, K.; Raghunathan, K. Charge-Discharge Asymmetry of Phase Change Electrodes from Isotropic Solid State Diffusion Models. *J. Electrochem. Soc.* **2013**, *159*, A26–A37.
- (95) Takami, N.; Hoshina, K.; Inagaki, H. Lithium Diffusion in Li4/3Ti5/3O4 Particles during Insertion and Extraction. *J. Electrochem. Soc.* **2011**, *158*, A725.
- (96) Berla, L. A.; Lee, S. W.; Ryu, I.; Cui, Y.; Nix, W. D. Robustness of Amorphous Silicon

- during the Initial Lithiation/Delithiation Cycle. J. Power Sources 2014, 258, 253–259.
- (97) Wang, Z.; Su, Q.; Deng, H.; He, W.; Lin, J.; Fu, Y. Q. Modelling and Simulation of Electron-Rich Effect on Li Diffusion in Group IVA Elements (Si, Ge and Sn) for Li Ion Batteries. *J. Mater. Chem. A* **2014**, *2*, 13976–13982.
- (98) Yoshimura, K.; Suzuki, J.; Sekine, K.; Takamura, T. Measurement of the Diffusion Rate of Li in Silicon by the Use of Bipolar Cells. *J. Power Sources* **2007**, *174*, 653–657.
- (99) Obrovac, M. N.; Krause, L. J. Reversible Cycling of Crystalline Silicon Powder. *J. Electrochem. Soc.* **2007**, *154*, A103.
- (100) Ogata, K.; Salager, E.; Kerr, C. J.; Fraser, A. E.; Ducati, C.; Morris, A. J.; Hofmann, S.; Grey, C. P. Revealing Lithium-Silicide Phase Transformations in Nano-Structured Silicon-Based Lithium Ion Batteries via in Situ NMR Spectroscopy. *Nat. Commun.* **2014**, *5*, 1–11.
- (101) Ghassemi, H.; Au, M.; Chen, N.; Heiden, P. A.; Yassar, R. S. In Situ Electrochemical Lithiation/Delithiation Observation of Individual Amorphous Si Nanorods. *ACS Nano* **2011**, *5*, 7805–7811.
- (102) Sun, C. F.; Karki, K.; Jia, Z.; Liao, H.; Zhang, Y.; Li, T.; Qi, Y.; Cumings, J.; Rubloff, G. W.; Wang, Y. A Beaded-String Silicon Anode. *ACS Nano* **2013**, *7*, 2717–2724.
- (103) Erlebacher, J.; Aziz, M. J.; Karma, A.; Dimitrov, N.; Sieradzki, K. Evolution of Nanoporosity in Dealloying. *Nature* **2001**, *410*, 450–453.
- (104) Choi, J. W.; McDonough, J.; Jeong, S.; Yoo, J. S.; Chan, C. K.; Cui, Y. Stepwise Nanopore Evolution in One-Dimensional Nanostructures. *Nano Lett.* **2010**, *10*, 1409–1413.
- (105) Decaluwe, S. C.; Dhar, B. M.; Huang, L.; He, Y.; Yang, K.; Owejan, J. P.; Zhao, Y.; Talin, A. A.; Dura, J. A.; Wang, H. Pore Collapse and Regrowth in Silicon Electrodes for Rechargeable Batteries. *Phys. Chem. Chem. Phys.* **2015**, *17*, 11301–11312.
- (106) Wahl, U.; Hofsäss, H.; Jahn, S. G.; Winter, S.; Recknagel, E. Direct Evidence for Substitutional Li after Ion-Implantation into Highly Phosphorus-Doped Si. *Appl. Phys. Lett.* **1993**, *62*, 684–686.
- (107) Li, H. A High Capacity Nano-Si Composite Anode Material for Lithium Rechargeable Batteries. *Electrochem. Solid-State Lett.* **1999**, 2, 547.
- (108) Li, H. Nano-Alloy Anode for Lithium Ion Batteries. Solid State Ionics 2002, 148, 247–258.
- (109) Baranchugov, V.; Markevich, E.; Pollak, E.; Salitra, G.; Aurbach, D. Amorphous Silicon Thin Films as a High Capacity Anodes for Li-Ion Batteries in Ionic Liquid Electrolytes. *Electrochem. commun.* **2007**, *9*, 796–800.
- (110) Zhang, S. Chemomechanical Modeling of Lithiation-Induced Failure in High-Volume-Change Electrode Materials for Lithium Ion Batteries. *npj Comput. Mater.* **2017**, *3*, 1–10.

- (111) Jung, S. C.; Choi, J. W.; Han, Y. K. Anisotropic Volume Expansion of Crystalline Silicon during Electrochemical Lithium Insertion: An Atomic Level Rationale. *Nano Lett.* **2012**, *12*, 5342–5347.
- (112) Kim, K. J.; Qi, Y. Vacancies in Si Can Improve the Concentration-Dependent Lithiation Rate: Molecular Dynamics Studies of Lithiation Dynamics of Si Electrodes. *J. Phys. Chem. C* **2015**, *119*, 24265–24275.
- (113) Katiyar, P.; Jin, C.; Narayan, R. J. Electrical Properties of Amorphous Aluminum Oxide Thin Films. *Acta Mater.* **2005**, *53*, 2617–2622.
- (114) Ostadhossein, A.; Kim, S.-Y.; Cubuk, E. D.; Qi, Y.; van Duin, A. C. T. Atomic Insight into the Lithium Storage and Diffusion Mechanism of SiO ₂ /Al ₂ O ₃ Electrodes of Lithium Ion Batteries: ReaxFF Reactive Force Field Modeling. *J. Phys. Chem. A* **2016**, *120*, 2114–2127.
- (115) Kim, S. Y.; Ostadhossein, A.; Van Duin, A. C. T.; Xiao, X.; Gao, H.; Qi, Y. Self-Generated Concentration and Modulus Gradient Coating Design to Protect Si Nano-Wire Electrodes during Lithiation. *Phys. Chem. Chem. Phys.* **2016**, *18*, 3706–3715.
- (116) Jung, H.; Park, M.; Yoon, Y. G.; Kim, G. B.; Joo, S. K. Amorphous Silicon Anode for Lithium-Ion Rechargeable Batteries. *J. Power Sources* **2003**, *115*, 346–351.
- (117) Ikeda, H.; Qi, Y.; Çagin, T.; Samwer, K.; Johnson, W. L.; Goddard, W. A. Strain Rate Induced Amorphization in Metallic Nanowires. *Phys. Rev. Lett.* **1999**, 82, 2900–2903.
- (118) Wodak, S. J.; Janin, J. Analytical Approximation to the Accessible Surface Area of Proteins. *Proc. Natl. Acad. Sci. U. S. A.* **1980**, *77*, 1736–1740.
- (119) Connolly, M. L. Analytical Molecular Surface Calculation. *J. Appl. Crystallogr.* **1983**, *16*, 548–558.
- (120) Chen, Q.; Sieradzki, K. Spontaneous Evolution of Bicontinuous Nanostructures in Dealloyed Li-Based Systems. *Nat. Mater.* **2013**, *12*, 1102–1106.
- (121) Barabasi, A.-L.; Stanley, H. E. *Fractal Concepts in Surface Growth*; Cambridge University Press: Cambridge, 1995.
- (122) Stournara, M. E.; Xiao, X.; Qi, Y.; Johari, P.; Lu, P.; Sheldon, B. W.; Gao, H.; Shenoy, V. B. Li Segregation Induces Structure and Strength Changes at the Amorphous Si/Cu Interface. *Nano Lett.* **2013**, *13*, 4759–4768.
- (123) Philipp, H. R. Optical and Bonding Model for Non-Crystalline SiOxand SiOxNymaterials. *J. Non. Cryst. Solids* **1972**, 8–10, 627–632.
- (124) Philipp, H. R. Optical Properties of Non-Crystalline Si, SiO, SiOxand SiO2. *J. Phys. Chem. Solids* **1971**, *32*, 1935–1945.
- (125) Dupree, R.; Holland, D.; Williams, D. S. An Assessment of the Structural Models for

- Amorphous Sio Using Mas Nmr. *Philos. Mag. B Phys. Condens. Matter; Stat. Mech. Electron. Opt. Magn. Prop.* **1984**, *50*, 13–18.
- (126) SiOx, A. A. of the R. of. Gordon McKay Laboratory, Harvard University, Cambridge, Mass. 02138, USA. **1975**, *17*, 215–230.
- (127) Miyachi, M.; Yamamoto, H.; Kawai, H.; Ohta, T.; Shirakata, M. Analysis of SiO Anodes for Lithium-Ion Batteries. *J. Electrochem. Soc.* **2005**, *152*, A2089.
- (128) Hwa, Y.; Park, C. M.; Sohn, H. J. Modified SiO as a High Performance Anode for Li-Ion Batteries. *J. Power Sources* **2013**, 222, 129–134.
- (129) Park, C. M.; Choi, W.; Hwa, Y.; Kim, J. H.; Jeong, G.; Sohn, H. J. Characterizations and Electrochemical Behaviors of Disproportionated SiO and Its Composite for Rechargeable Li-Ion Batteries. *J. Mater. Chem.* **2010**, *20*, 4854–4860.
- (130) Schulmeister, K.; Mader, W. TEM Investigation on the Structure of Amorphous Silicon Monoxide. *J. Non. Cryst. Solids* **2003**, *320*, 143–150.
- (131) Yom, J. H.; Hwang, S. W.; Cho, S. M.; Yoon, W. Y. Improvement of Irreversible Behavior of SiO Anodes for Lithium Ion Batteries by a Solid State Reaction at High Temperature. *J. Power Sources* **2016**, *311*, 159–166.
- (132) Nagamori, M.; Boivin, J.-A.; Claveau, A. Gibbs Free Energies of Formation of Amorphous Si2O3, SiO and Si2O. *J. Non. Cryst. Solids* **1995**, *189*, 270–276.
- (133) Hirata, A.; Kohara, S.; Asada, T.; Arao, M.; Yogi, C.; Imai, H.; Tan, Y.; Fujita, T.; Chen, M. Atomic-Scale Disproportionation in Amorphous Silicon Monoxide. *Nat. Commun.* **2016**, 7, 1–7.
- (134) Chou, C. Y.; Hwang, G. S. Lithiation Behavior of Silicon-Rich Oxide (SiO1/3): A First-Principles Study. *Chem. Mater.* **2013**, *25*, 3435–3440.
- (135) Kim, J. H.; Park, C. M.; Kim, H.; Kim, Y. J.; Sohn, H. J. Electrochemical Behavior of SiO Anode for Li Secondary Batteries. *J. Electroanal. Chem.* **2011**, *661*, 245–249.
- (136) Yoo, S.; Kim, J. H.; Kang, B. Characterizing Local Structure of SiOxusing Confocal μ-Raman Spectroscopy and Its Effects on Electrochemical Property. *Electrochim. Acta* **2016**, 212, 68–75.
- (137) Sakko, A.; Sternemann, C.; Sahle, C. J.; Sternemann, H.; Feroughi, O. M.; Conrad, H.; Djurabekova, F.; Hohl, A.; Seidler, G. T.; Tolan, M.; *et al.* Suboxide Interface in Disproportionating a -SiO Studied by x-Ray Raman Scattering. *Phys. Rev. B Condens. Matter Mater. Phys.* **2010**, *81*.
- (138) Kim, T.; Park, S.; Oh, S. M. Solid-State NMR and Electrochemical Dilatometry Study on Li[Sup +] Uptake/Extraction Mechanism in SiO Electrode. *J. Electrochem. Soc.* **2007**, *154*, A1112.

- (139) Bondi, R. J.; Lee, S.; Hwang, G. S. First-Principles Study of the Mechanical and Optical Properties of Amorphous Hydrogenated Silicon and Silicon-Rich Silicon Oxide. *Phys. Rev. B* **2010**, *81*, 195207.
- (140) Mamiya, M.; Kikuchi, M.; Takei, H. Crystallization of Fine Silicon Particles from Silicon Monoxide. *J. Cryst. Growth* **2002**, *237*–*239*, 1909–1914.
- (141) Seko, A.; Togo, A.; Tanaka, I. Descriptors for Machine Learning of Materials Data. **2017**, 1–12.
- (142) Behler, J. Neural Network Potential-Energy Surfaces for Atomistic Simulations; 2010.
- (143) Behler, J. Perspective: Machine Learning Potentials for Atomistic Simulations. *J. Chem. Phys.* **2016**, *145*.
- (144) Artrith, N.; Urban, A. An Implementation of Artificial Neural-Network Potentials for Atomistic Materials Simulations: Performance for TiO2. *Comput. Mater. Sci.* **2016**, *114*, 135–150.
- (145) Szlachta, W. J.; Bartók, A. P.; Csányi, G. Accuracy and Transferability of Gaussian Approximation Potential Models for Tungsten. *Phys. Rev. B Condens. Matter Mater. Phys.* **2014**, *90*, 1–6.
- (146) Artrith, N.; Urban, A.; Ceder, G. Efficient and Accurate Machine-Learning Interpolation of Atomic Energies in Compositions with Many Species. *Phys. Rev. B* **2017**, *96*, 1–7.
- (147) Artrith, N.; Urban, A.; Ceder, G. Constructing First-Principles Phase Diagrams of Amorphous LixSi Using Machine-Learning-Assisted Sampling with an Evolutionary Algorithm. *J. Chem. Phys.* **2018**, *148*, 1–10.